

UvA-DARE (Digital Academic Repository)

Colloidal patchy particle architectures

Simulations of accurate models in and out of equilibrium Jonas, H.J.

Publication date 2024 Document Version Final published version

Link to publication

Citation for published version (APA):

Jonas, H. J. (2024). Colloidal patchy particle architectures: Simulations of accurate models in and out of equilibrium. [Thesis, fully internal, Universiteit van Amsterdam].

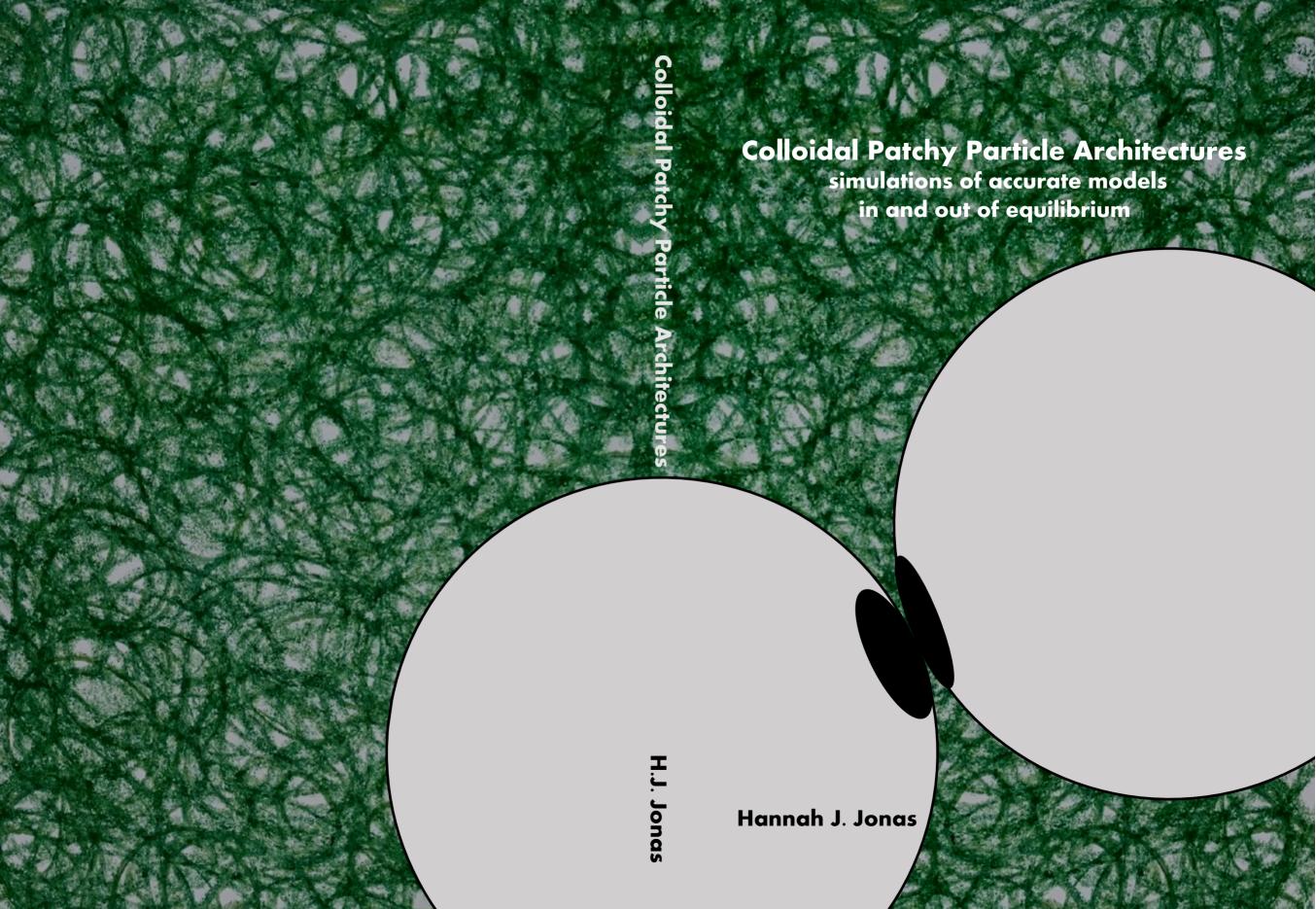
General rights

It is not permitted to download or to forward/distribute the text or part of it without the consent of the author(s) and/or copyright holder(s), other than for strictly personal, individual use, unless the work is under an open content license (like Creative Commons).

Disclaimer/Complaints regulations

If you believe that digital publication of certain material infringes any of your rights or (privacy) interests, please let the Library know, stating your reasons. In case of a legitimate complaint, the Library will make the material inaccessible and/or remove it from the website. Please Ask the Library: https://uba.uva.nl/en/contact, or a letter to: Library of the University of Amsterdam, Secretariat, Singel 425, 1012 WP Amsterdam, The Netherlands. You will be contacted as soon as possible.

UvA-DARE is a service provided by the library of the University of Amsterdam (https://dare.uva.nl)



Colloidal Patchy Particle Architectures

SIMULATIONS OF ACCURATE MODELS IN AND OUT OF EQUILIBRIUM

H.J. Jonas

Cover design by H.J. Jonas

Copyright © H.J. Jonas, 2023. All rights reserved.

A digital copy of this thesis can be obtained via dare.uva.nl

The author can be reached at: hannahjonas@hotmail.com

Colloidal Patchy Particle Architectures

simulations of accurate models in and out of equilibrium

ACADEMISCH PROEFSCHRIFT

ter verkrijging van de graad van doctor
aan de Universiteit van Amsterdam
op gezag van de Rector Magnificus
prof. dr. ir. P. P. C. C. Verbeek
en overstaan van een door het College voor Promoties ingestelde
commissie, in het openbaar te verdedigen in de Agnietenkapel
op dinsdag 30 januari 2024, te 16.00 uur

door

Hannah Julia Jonas

geboren te Eindhoven, Nederland

Promotiecommissie:

Promotores: prof. dr. P.G. Bolhuis Universiteit van Amsterdam

prof. dr. P. Schall Universiteit van Amsterdam

Overige leden: prof. dr. M.F. Hagan Brandeis University

prof. dr. E.J. Meijer

prof. dr. D.J. Kraft dr. S. Jabbari Farouji dr. ir. I.M. Ilie prof. dr. S. Woutersen Universiteit van Amsterdam Universiteit van Amsterdam

Universiteit van Amsterdam

Faculteit der Natuurwetenschappen, Wiskunde en Informatica





Het hier beschreven onderzoek is uitgevoerd binnen de groep van prof. dr. Peter G. Bolhuis aan het Van 't Hoff Institute for Molecular Sciences van de Universiteit van Amsterdam (gevestigd te Science Park 904, 1098 XH, Amsterdam). Het onderzoek is gefinancieerd met steun dat de Foundation for Fundamental Research on Matter (FOM) dat onderdeel is van de Nederlandse Organisatie voor Wetenschappelijk Onderzoek (NWO) met Grant No. 680.91.124.

Contents

1	Introduction							
	1.1	Building atoms, molecules and matter	12					
	1.2	(Molecular) Self-Assembly	14					
	1.3	Colloidal Patchy Particles	16					
	1.4	Colloidal Self-Assembly into Molecular and Bio-Inspired Architectures	20					
	1.5	Outline of the Thesis	22					
2	Theory and Computational Methods							
	2.1	Thermodynamics and Statistical Mechanics	26					
	2.2	Thermodynamic Perturbation Theory	29					
	2.3	Monte Carlo	31					
	2.4	Brownian Molecular Dynamics	34					
	2.5	Measuring	38					
3	Атв	A temperature-dependent critical Casimir patchy particle model bench-						
		KED ONTO EXPERIMENT	45					
	3.1	Introduction	46					
	3.2	Theoretical Background	4 7					
	3.3	Simulation Methods	55					
	3.4	Results and Discussion	56					
	3.5	Conclusion	62					
	3.6	Appendix	63					
4	Ехт	Extended Wertheim theory predicts the anomalous chain length dis-						
	TRIE	BUTIONS OF DIVALENT PATCHY PARTICLES UNDER EXTREME CONFINEMENT	77					
	4.1	Introduction	78					
	4.2	Theory	80					
	4.3	Simulation Methods	86					
	4.4	Results and Discussion	92					
	4.5	Conclusions	96					
5		ACTIVITY AFFECTS THE STABILITY, DEFORMATION AND BREAKAGE DYNAMICS						
	OF COLLOIDAL ARCHITECTURES 99							
	5.1		100					
	5.2		101					
	5.3	Results and Discussion	108					
	5 4	Conclusions	117					

Contents

	5.5	Appendix	120	
6	Аст		125	
	6.1			
	6.2	Methods	127	
	6.3	Results	131	
	6.4	Conclusions	138	
7	Sum	MARY	141	
8	Nederlandstalige samenvatting			
Ac	CKNO	WLEDGMENTS	150	
Lı	ST OF	PUBLICATIONS	152	
Bı	BLIOG	згарну	154	

1 Introduction

The behavior of large and complex aggregates of elementary particles, it turns out, is not to be understood in terms of a simple extrapolation of the properties of a few particles.

P. W. Anderson [1]

1.1 Building atoms, molecules and matter

All matter, whether on Earth, in a different galaxy, or anywhere in between, is composed of atoms. It has always fascinated me how such a vast variety of materials with different appearances, textures, and functions can exist. The reason I chose to study chemistry was because I wanted to understand why rubber is an insulator, why iron may rust over time, and why water can exist as a liquid, a snowflake, a block of ice, or become invisible in the air. The answer to these questions must surely lie within the basic building block of molecules and matter: the atom, right?

An atom consists of a nucleus – positively charged protons and neutral neutrons – surrounded by a cloud of negatively charged electrons. By increasing the number of protons in the nucleus, we create different types of atoms, i.e., the chemical elements. There are 118 different chemical elements listed in the periodic table, which orders them according to their number of protons in the nucleus (see Fig. 1.1a).

The electrons of the atom are located in so-called orbitals, which are regions around the atom where electrons are most likely to be found. They have distinct shapes and allow the atom to form chemical bonds with other atoms (see Fig. 1.1b) [3]. These bonds are formed when two

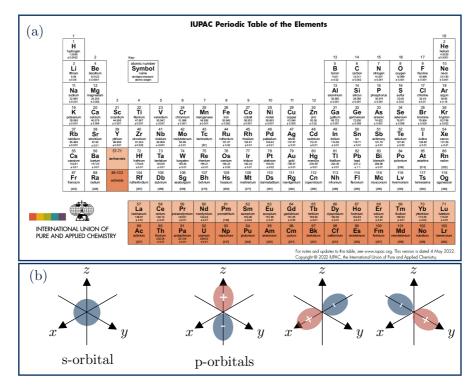


Figure 1.1: (a) Periodic table of elements. All matter is composed of atoms that is one of these 118 chemical elements of which only 92 exists naturally. [2] (b) The electrons of the atoms are located in so-called orbitals, i.e. regions is space the electron is likely to be in. Here schematically illustrated: the spherical s-orbital, and the p-orbital with its three orthogonal directions. The nucleus is located at the intersection of the x, y, z-axes.

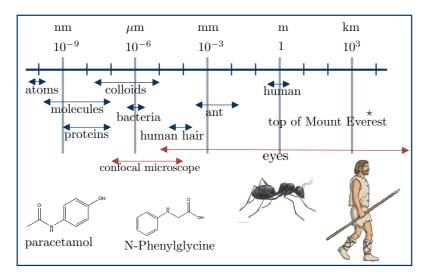


Figure 1.2: (top)Typical length scales of atoms, molecules, proteins, bacteria, colloidal particles, a human, and the top of Mount Everest on a logarithmic scale. The orange arrows indicate the scope of sight of a confocal microscope and the human eyes. (bottom) Chemical drawings of paracetamol and N-Phenylglycine, and an ant and human [7, 8]

atoms overlap their orbitals and share two electrons. A structure of two or more atoms connected by such chemical, i.e., covalent, bonds is called a molecule.

Molecules with different chemical properties are created by covalently binding a number of atoms in a specific sequence. Synthetic chemists have mastered the manipulation of atomic reactivity to synthesize molecules with the same atoms but in different arrangements, giving them distinct functions. For instance, the molecules paracetamol and N-Phenylglycine both consist of the same atoms with the chemical formula $C_8H_9NO_2$, yet they have different structures (see Fig. 1.2). The former is a well-known painkiller, while the latter is industrially used as a precursor for blue paint pigments.

Using the framework of quantum mechanics, we can numerically calculate the energies associated with the chemical bonds between atoms, providing insight into the properties of molecules [4]. However, calculations based on quantum mechanical theory require approximations and simplifications for the electrons, e.g., using the Slater [5] or Gaussian basis-set, and the nucleus, e.g., approximating the nucleus as a point charge (known as the Born-Oppenheimer approximation [6]). Moreover, these calculations become exponentially computationally intensive as the number of electrons increases, making these simulations best suited for modeling e.g. individual molecules.

Because molecules and atoms are incredibly small (see Fig. 1.2), we need many of them together to observe them with our eyes or even refer to them as a material. Little did I know when I began studying chemistry that the answers to understanding the chemical and physical properties of materials do not just lie entirely within the molecule itself. Understanding its basic building block, the atom, is entirely one piece of the puzzle.

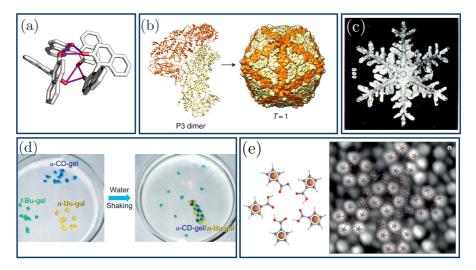


Figure 1.3: Molecular self-assembly at many length scales. (a) supramolecular cages connected by hydrogen bonds (Å- nm-range), (b) a virus capsid (nm-range)[13], (c) frozen water molecules form a snowflake (mm-range), (d) gel-like cubes in a petri dish need a shaking motion to collide (cm-range), (e) computer and STM image of a two dimensional quasicrystal composed of ferrocenecarboxylic acid (nm-range). With Refs [13–17] from a-e, respectively.

1.2 (Molecular) Self-Assembly

Some properties and functions of materials extend beyond the characteristics of their individual molecules and emerge from the collective arrangement of many molecules or atoms together. For instance, entangled and unentangled polymers exhibit vastly different dynamics, which have significant implications for properties such as melting temperatures [9]. Likewise, liquid crystals can adjust their orientation and spatial configuration when an electric field is applied. This adaptive quality allows them to modulate their transparency, thereby controlling the passage of light. Such materials have become integral to modern devices, most notably in televisions and various electronic displays, where they are a key component of liquid crystal displays (LCDs) [10]. In the realm of advanced materials, the conductivity of graphene sheets is notably sensitive to minute imperfections, even those as diminutive as a single atom [11]. Therefore, to truly comprehend these properties, one must adopt a zoomed-out perspective to examine the structures that molecules form over length scales much larger than their individual sizes.

Intriguingly, the individual building blocks itself are not aware of any bigger picture; they simply interact with their immediate neighbors through forces of attraction or repulsion when in close proximity. Yet, without any external guidance or set of instructions, these building blocks can spontaneously organize into large-scale structures. This spontaneous organization process is called *self-assembly*. [12]

Self-assembling building blocks span a wide range of sizes, from molecules and nanoparticles to colloidal particles and even macroscopic objects, self-assemble into architectures ranging from the nm to mm or even macroscopic scale (Fig. 1.3) [18, 19]. What they need is a source of energy that enables them to move around, meet each other and subsequently interact. For molecules and colloidal particles, heat serves as the primary driver. Atomic motion is primarily attributed

to kinetic energy, i.e. temperature; colloidal particles are immersed in a colloidal suspension experience random, erratic motion as surrounding solvent molecules continually bombard their surface. However, macroscopic objects, being considerably heavier, are not influenced by such thermal effects. They typically require alternative energy sources, such as externally-induced agitation, to initiate movement and assembly [17].

In the molecular context, upon collision of two molecules or two parts of the same molecule, they can form non-covalent bonds through attractive interactions such as hydrogen bonds or Van der Waals, Coulomb, and hydrophobic interactions. Compared to the covalent bonds between atoms, these non-covalent bonds are weak. As a result, they often give rise to a soft and deformable rather than rigid character to a material. One advantage of these weaker bonds is their reversibility, characterized by a relatively low activation barrier. This helps the system to escape kinetic traps and "fix" mistakes in the self-assembly over time [20–22].

As scientists, we aim to understand how or why certain structures form or break, how they can avoid kinetic traps or repair defects via molecular self-assembly. It would teach us how to make complex architectures ourselves or smart materials that can self-heal, or respond on demand [23, 24]. In light of the example in Fig. 1.3b, understanding the self-assembly of virus capsids opens up the opportunity to design new antiviral drugs [25]. Likewise, nanoparticles, e.g. micelles, act as a vehicle to transport drugs to target areas in the body, e.g. cancer cells, to maximize efficacy and minimize side effects [26–28].

Computationally it is not feasible to simulate the intricate details of (quantum mechanical) molecular motion to investigate molecular self-assembly as that would quickly become extremely expensive. This is because self-assembly not only operates over extended length scales, but also unfolds over more prolonged time scales. The former implies the need of many or large molecules, while the latter stems from the fact that typical molecular vibrations, such as the C-H vibration, are particularly fast compared to the translational or rotational movement of an entire molecule. Luckily, we do not need a detailed description of covalent bonds.

Removing molecular details (in simulation) is called "coarse graining". The quantum mechanical interactions are replaced by simplistic functionals that often only depend on distances and angles of particles. There are various degrees of coarse graining. For example, in biomolecular force fields such as AMBER, single atoms are substituted with straightforward pairwise additive approximations [29]. Meanwhile, the Martini force field represents multiple atoms and their associated chemical attributes as a single bead [30]. Naturally, an inherent drawback of coarse graining is the loss of detailed chemical information making the method not suitable for exploring chemical reactions.

Yet, the advantages of coarse graining are notable. Simulations become more computationally efficient, allowing for the observation of extended trajectories and the system's long-time dynamics. Moreover, removing chemical details provides a general picture, offering insights not tethered to a specific molecular framework. It can reveal a set of minimal requirements of chemical or physical properties in forming a target structure, or assist in tasks like the initial screening of prospective drug compounds. [31–33]

1.3 COLLOIDAL PATCHY PARTICLES

In this thesis, in order to explore and understand the structural behavior and responses of atoms, molecules, and living matter, we use patchy colloidal particles as a model, or, in other words, coarse-grained system. These micron-sized – not necessarily spherical – particles not only exist in theory and simulation[39–46], but also in experiment [34–38, 47–49]. Their surface is decorated with attractive patches that leads to self-assembly via different driving forces such as: electrostatics[50], DNA coated surfaces[51, 52], critical Casimir forces[53–60], or depletion interactions[61] (Fig. 1.4).

There are four aspects that make patchy particles a suitable model system: their structure, similar statistics as atoms and molecules, their controllable interactions, and their direct observability. Each aspect is discussed next.

1.3.1 STRUCTURE

In his *Lectures on Gas Theory* * , Ludwig Boltzmann already thought of the idea that one could simplify the physical picture of two atoms, such as iodine I_2 , dissociating their bond, and imagine the separation of two particles connected through localized attractions (Fig. 1.5a). The attractive space is small compared to the size of the atom and rigidly connected to the external surface of the atom and two atoms only are considered bound if their attractive regions fully or partially overlap [62].

Boltzmann's simplistic idea of an atom resembles the structure of the colloidal patchy particles that now can be experimentally made which are used by my experimental collaborators (Fig. 1.5b) [56, 60]. The bulk (core, non-patch) of the colloidal particle is made of polystyrene (PS), and the patches of 3-(trimethoxysilyl)propyl methacrylate (TPM) and synthesized with a technique called colloidal fusion [63]. Due to the hydrophilic and hydrophobic affinity of the core and the patches (Fig. 1.5c) respectively, specific and directed, i.e. one bond per patch, bonding is made possible via [56].

The placement of the patches are in such a way that patchy particles can act as structural mesoscopic, coarse-grained analogue of carbon atoms. Dipatch, trigonal planar, and tetrapatch particles with two, three, and four patches can make structurally similar to sp-, sp²-, and sp³-hybridized carbon atoms (Fig. 1.5d), respectively.

^{*}Thanks to Prof. Christoph Dellago for sharing this story with me

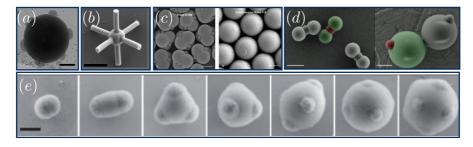


Figure 1.4 : Scanning electron microscope (SEM) images of patchy colloidal particles. The scale bar has length 100 nm, 1 μ m, 1 μ m, 2 μ m, and 500 nm from Refs [34–38] in (a) to (e), respectively.

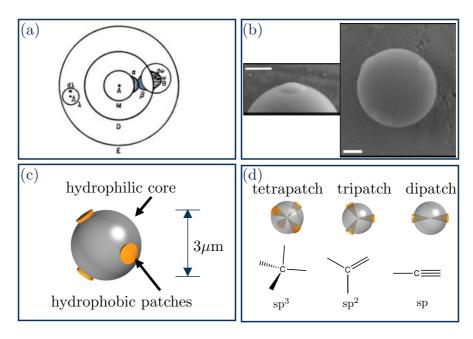


Figure 1.5 : (a) Boltzmann's idea of two atoms chemically binding via localized areas on the edge of the atoms. Particle A is represented by the circle M with an attractive *patch* in the shaded volume α . A second atom B, with its center of mass in volume ω , (partially) overlaps its sensitive region β with α . A chemical bond exists, only if α and β overlap. [62] (b) SEM image of experimental tetrapatch particle (right), and zoomed in at the patch (left). The scalebar is 1 μ m. [63] (c) The bulk and patch materials have different chemical composition which enables them to make directed bonds. (d) The patches of the tetra-, tri-, and dipatch particles belong to the T_d , D_{3h} , and $D_{\infty h}$ symmetry group, and are positioned in a similar fashion as the hybridized sp³, sp², and sp bonding orbitals of carbon, respectively. These hybridized bonding orbitals are mixtures of the s- and p-orbitals in Fig. 1.1b. The (grey-colored) bulk of the particle is made transparent to clearly show the orientation of the patches (in orange).

Note that the trigonal planar particles have not been synthesized using the colloidal fusion technique, and only exists in my computer simulations. However, in experiment, trigonal planar bonding is mimicked by a tetrapatch particle with one patch bound to the capillary wall, leaving three patches available to bind. [58, 59]

1.3.2 STATISTICS SIMILAR TO ATOMS AND MOLECULES

Another feature of the micron-size of colloidal particles is that, due to the impinging solvent molecules that can be 1 000 to 10 000 times smaller in diameter than the colloidal particles (Fig. 1.2), they exhibit a random motion. This motion, known as Brownian or thermal motion, translates and rotates the particle in the solvent and makes the particles to follow Boltzmann statistics in equilibrium, just like atoms and molecules. Therefore, patchy colloidal particles may not only have structural similarities with atoms, but also statistically. This means that colloidal systems show similar phase behavior as molecules, such as formation of crystal, fluid, vapor, gas, or coexisting phases depending on the interaction potential, density and temperature. [64–66]

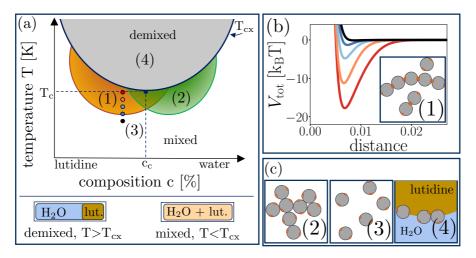


Figure 1.6: Tunable, reversible and specific critical Casimir interactions. (a) A schematic illustration of the phase diagram of the water-lutidine binary mixture as function of temperature and composition. Above the phase separation, or coexistence, temperature $T_{\rm cx}$ (dark blue line), when $T \ge T_{\rm cx}$, the system is demixed into two phases. In this region (grey region at number 4), the two phases are visible in the capillary (bottom left illustration in (a)) and the particles may aggregate at the water-lutidine interface. Below $T < T_{\rm cx}$, the system is mixed into one phase (bottom right illustration in (a)) and the patchy particles either attract at the patches, at the bulk, or do not interact in the orange, green and white regions, respectively. (b) Depending on how *far* you are from the critical point (dark blue dot at (c_c, T_c)), the critical Casimir attraction can be turned on or off in the total potential $V_{\rm tot}$. Illustrations in (b) and (c) depict patchy particles' behavior at points 1 to 4 in the phase diagram in (a).

However, note that a single dynamical trajectory of colloidal particles is not directly comparable to a single trajectory of molecules. Atoms and molecules have inertia and deterministic motion, whereas colloids are overdamped, show stochastic motion , and their translational and rotational motion are defined by their respective diffusion constants. Specifically, at short timescales, the motion of molecule is ballistic. After many collisions, the motion of molecules becomes indeed decorrelated and effectively diffusive. So, under the assumption that the diffusion constants are in the correct regime, mimicking the diffusive motion of the molecules the dynamical behavior of colloidal particles averaged over a whole collection of trajectories is comparable to the dynamical behavior of atoms and molecules.

1.3.3 Direct Control

The attraction between patchy particles of this thesis results from critical Casimir interactions [67]. Critical behavior is characterized by (universal) scaling relations that manifest in various natural phenomena such as connected networks in the brain [68], prices on the stock-market [69], and molecular phase transitions. A favorite critical system among physicists is the Ising model that consists of interacting spin particles on a lattice oriented up (+1) or down (-1) [70]. The spin particles interact only with their direct neighbors and attract when aligned and repel otherwise, such as in the case of +1 and -1 spins. Below a specific temperature, the critical temperature T_c , the spins like to lower their energy by aligning either upward or downward, yielding an average

spin >0. Above T_c , the system contains enough kinetic energy to disorder the spins yielding the average spin equal to 0. Around the critical point, the correlation length ξ diverges, which in practice means if a spin flips it affects the spin orientation of a particle at distance ξ . With the help of the mathematical description of the Ising model, the behavior, such as its fluctuations and diverging correlation lengths, of the spins around the critical point were able to be described by (universal) critical scaling relations. [71]

The critical Casimir interactions arise from the diverging bulk correlation length ξ of the concentration fluctuations when approaching the critical point of e.g. a binary solvent mixture. The fluctuations of the solvent molecules become correlated over large distances and need *space* to exist.* The surfaces of two objects, e.g. spherical particles [72], (chemically treated) walls [73, 74], patchy particles [53, 55, 75], quantum dots or other nanoparticles [76–78], or colloidal cubes [79], act as boundary conditions confining fluctuations between. If their surface-surface distance becomes smaller ξ , they spatially restrict the (critical) fluctuations and gives rise to an effective force called critical Casimir force which was first introduced by Fisher and de Gennes in 1978 [80].

Figure 1.6a shows a schematic phase diagram of the water-lutidine mixture that is used in experiment which has a lower critical point at c_c =0.287 mass fraction lutidine in water and T_c =33.68°C [81]. Its critical behavior at convenient experimental conditions, i.e. atmospheric pressure, and T_c close to and a little above room temperature, makes it a suitable candidate for employing critical Casimir interactions.

The strength and sign, i.e. attractive or repulsive interaction, of the critical Casimir force depends on a few factors. First of all, the *distance* from the critical point, in terms of composition c as well as temperature T, defines the critical scaling behavior and thus the shape and depth of the critical Casimir interaction. At given composition, the temperature acts a knob to tune the interaction in experiment; the closer you are to T_c , indicated by the five colored dots in Fig. 1.6a, the stronger the attraction between the particles (Fig. 1.6b).

Second, at off-critical composition, i.e. $c \neq c_c$, a surface adsorption preference can be created for the boundary conditions. At lutidine concentration $c < c_c$, there is an excess of water and deficiency of lutidine in the solution with respect to critical composition. In this case, lutidine rich density fluctuation are confined between the particles. Lutidine prefers interaction with the hydrophobic patches enabling specific patch-patch binding in the orange region of Fig. 1.6a. Conversely, at lutidine concentration $c > c_c$, water rich density fluctuations will be confined that prefer binding to the bulk material of the particles enabling bulk-bulk binding in the green region of Fig. 1.6a. The wettability of the solvent molecules on the surface of the particle is captured by a wetting factor w and tunes the critical Casimir strength. [82, 83]

Lastly, the geometrical shape of the boundary conditions is important. A flat surface will cause stronger forces compared to curved ones. Consequently, for spherical particles, the interaction is directly proportional to its radius particles, calculated within the Derjaguin approximation [84], such that particles with large radii interact stronger than those with small radii.

The critical Casimir interaction is reversible, tunable, and –under the right solvent conditions–specific and gives us direct control of the self-assembly into molecular, supramolecular and bio-

^{&#}x27;You can even see the critical highly correlated density fluctuation with your eyes as swirling clouds in CO_2 in this video: https://www.youtube.com/watch?v=-gCTKteN5Y4



Figure 1.7: Three snapshots of the video of Simon Stuij of dipatch particles assembling into colloidal chains adapted from Ref. [56]. (a) Only monomers at t=0h, (b) growing dipatch particle chains at t=2h, and (c) fully assembled chains at t=18h. Distinct chains are indicated by the colors. The scale bar is approximately 25 μ m.

inspired architectures. More on self-assembled architectures in Sec. 1.4. For a more in-depth theoretical description of the critical Casimir potential, see Sec. 3.6.1.

1.3.4 Direct Observation

An feature of micron-size of patchy particles is their visibility under e.g. a brightfield or confocal microscope. It enables direct tracking of the movement of patchy particles as seen in this 'video made by Simon Stuij (see Fig. 1.7 for snapshots). The video start with monomeric dipatch particles; far from $T_{\rm c}$. Then, the temperature is quenched close to $T_{\rm c}$ which turns on the critical Casimir attraction between the patches of divalent particles. Subsequently, the growth of chains by the self-assembly of dipatch particles is observed in time.

Direct visualization of the movements of the particles provides insight in the dynamics and kinetics of phase transitions such as nucleation[85], sublimation [86], and melting [87, 88] of crystals, the growth of nematic phases [53], and propagation of defects [58, 89, 90]. Following these processes on the atomic scale is difficult and requires advanced techniques. For example, electron microscopy such as scanning tunneling microscopy (STM) is able able to directly observe atoms (see for example this[†] cool video, and here[‡] for the making of) [91].

1.4 Colloidal Self-Assembly into Molecular and Bio-Inspired Architectures

Despite their apparent simplicity, colloidal patchy particles have effectively served as coarse-grained representations for a diverse array of structures. As depicted in Fig. 1.5, these particles can function akin to *big atoms*, forming colloidal configurations that structurally resemble organic molecules, such as cyclopentane (see Fig. 1.8a). [57, 92] Notably, even for water—a molecule fundamental to our existence and characterized by thermodynamic and dynamic anomalies still not fully grasped—tetrapatch particles have illuminated its intricate phase behavior by drawing parallels with empty liquids. [93] This notion of "empty liquids", defined as systems exhibiting coexistent liquid states in low-density regimes, was originally introduced by using thermodynamic perturbation theory (see Sec. 2.2) and patchy particle simulations in Ref. [94].

Many functions and structures in biological matter, think of the hydrogen bonding network between DNA basepair nucleotides, the stacked fatty chains and hydrophilic head groups form-

^{*}https://www.youtube.com/watch?v=DmA70xEYrzY

https://www.youtube.com/watch?v=oSCX78-8-q0

^{*}https://www.youtube.com/watch?v=xA4QWwaweWA

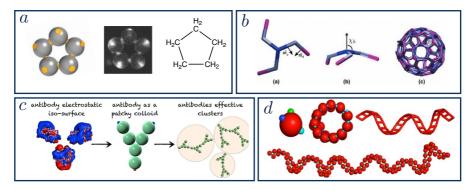


Figure 1.8: (a) Patchy particles as big atoms [57]. (b) Cage formation with a clathrin patchy particle model [102]. (c) Patchy particles as a model for antibody aggregation [99]. (d) Biomolecular mimetic supracolloidal helices [97].

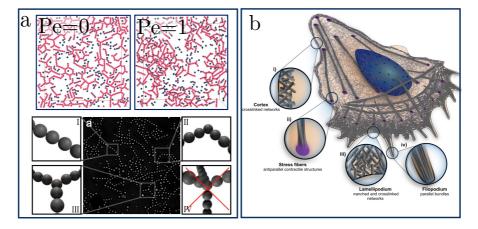


Figure 1.9 : (a) Patchy colloidal particles self-assembled into colloidal networks. At the top, snapshots of two simulated networks with dT=0.12 K at passive (Pe=0), and minor activity (Pe=1) are shown. The particles are colored according to their cluster size N_c , ranging from 1 (dark blue) to >4 (bright pink). See Chapter 6 for more details. At the bottom, an experimental patchy particle system recorded by Piet Swinkels. The colloidal network contains linear chains (I), chains with kinks (II) and nodes (III) . From Ref. [60]. (b) A schematic representation of a cell showcasing different architectures of actin filaments depending on their structure and location. From Ref. [103].

ing the lipid bilayer of the cell membrane, or ligand-protein interactions, are encoded by their non-covalent bonds. Therefore, patchy particles has served as a model system for the self-assembly of bio-inspired architectures such as virus capsids [95], DNA-like helices [96–98], antibodies [99], and other proteins [42, 100, 101] (see Fig. 1.8b-d).

Active physical gels, a fascinating subset of active matter, find their natural counterparts in the cytoskeleton of for example muscle and plant cells[104]. These gels stand out due to their viscoelastic character combined with continuous injection of energy by molecular motors, leading to notable non-equilibrium responses [105]. Actin filaments, which constitute the cytoskeleton's network, cycles through assembly and disassembly. Based on its position and corresponding func-

tion within the cell, actin can adopt various configurations, including branched and crosslinked networks in the cell cortex and lamellipodium, as depicted in Fig. 1.9b [103]. A mesoscopic structural analogue of the crosslinked or branched actin networks can be self-assembled using patchy particles interacting with critical Casimir attractions (Fig. 1.9a). When integrated with active colloidal particles, specifically Janus particles as detailed in Sec. 2.4.1, the passive colloidal gels can respond to active forces exerted on them leading to, for example, shape changes as depicted in Fig. 1.9a.

1.5 OUTLINE OF THE THESIS

This thesis aims to shed light on the microscopic structural behaviors of molecular and bioinspired materials using patchy colloidal particles through a close collaboration between experiment, theory and numerical simulations. The latter two are the focus of this thesis.

As colloidal patchy particles possess similar statistics as molecules and atoms, the theories from statistical mechanics and thermodynamics are also applicable to their systems. Chapter 2 will give an introduction of the theoretical basics, with a focus on the canonical ensemble, describing phase behavior including phase separation and the Van der Waals equation. When interested in observables of (patchy particle) systems, one may resort to theory or computer simulations. For simulating patchy particles two algorithms are used in this thesis: Monte Carlo and Brownian molecular dynamics. We end with a brief overview of measurement algorithms that are not discussed in detail in the other chapters.

In Chapter 3, we developed an accurate patchy particle model that interact via the critical Casimir force in off-critical binary liquids such as water-lutidine mixtures. It is based on theoretical critical Casimir potentials, the geometry of the patchy particle of interest, and benchmarked onto experimentally measured chain length distributions and bending rigidities of colloidal semiflexible polymers composed of divalent patchy particles. Our model enables us to accurately predict the experimental measurements and give a detailed mechanistic insights.

In Chapter 4, we extend Wertheim's theoretical framework for associating divalent particles under extreme confinement. Under the influence of the gravitational field, colloidal particles sediment with sub-diameter gravitational heights to the bottom of the capillary in both simulations and real-world experiments. This quasi-2D confinement affects chain length distributions of self-assembling divalent patchy particles showing an abundance of monomers. By factoring in the effect of confinement into the theory, without any adjustable parameter, the predictions of the chain length distribution are in excellent agreement with explicit simulations of self-assembling particles. Given the accuracy of our predictions, we provide insights into the role of confinement on thermodynamic equilibrium and provide a quantitative explanation for how the persistence length of semi-flexible chains affects their reactivity in extreme confinement.

In Chapter 5, we delve into the microscopic mechanisms behind bond breakage within colloidal patchy particle architectures, specifically under the influence of activity. We conduct a numerical investigation by introducing self-propelled colloids modeled as active Brownian particles into a self-assembling colloidal dispersion of dipatch and tripatch particles that form three archetypal substructures, namely, dimers, chains, and rings. We find a rich response behavior to the introduction of self-propelled particles, in which the activity can enhance as well as reduce the stability of the architecture, deform the intact structures and alter the mechanisms of

fragmentation We rationalize these finding in terms of the rate and mechanisms of breakage as function of the direction and magnitude of the active force by separating the bond breakage process into two stages: escaping the potential well and separation of the particles.

In Chapter 6, we explore the responses of physical gels under the influence of activity. Active physical gels are an interesting type of active matter, which are observed in biological systems such as the cytoskeleton in muscle and plant tissues; these gels are vital for processes such as cell motility and tissue repair. For this, we use patchy colloidal gels composed of divalent and trigonal planar patchy particles interacting via the critical Casimir force as a model system. Similar as for the active colloidal molecules from Chapter 5, we find a rich response behavior when introduction of self-propelled particles in the colloidal networks leading to growth or fragmentation of clusters.

Theory and Computational Methods

In this chapter we start with introducing statistical mechanics and thermodynamics. Then, phase behavior and how the Van der Waals equation or Thermodynamic Perturbation Theory predict it. One may also resort to computer simulation to understand the behavior and responds of materials. This thesis uses two algorithms to sample states in phase space, namely Monte Carlo and Brownian Molecular Dynamics which are discussed.

2.1 THERMODYNAMICS AND STATISTICAL MECHANICS

As scientists, our aim is to understand and predict the properties of materials, allowing us to make informed design decisions and engineer materials with targeted functionalities [32, 97, 106–108]. The knob to tune properties of materials is the interaction potential V, which is an expression of the microscopic energy and provides a complete description of the system. In our patchy particle system, the interaction potential depends on the position ${\bf r}$ and orientation ${\bf \Omega}$ of the N particles that are, in short, written as ${\bf r}^N = \{{\bf r}_1, \dots {\bf r}_N\}$ and ${\bf \Omega}^N = \{{\bf \Omega}_1, \dots {\bf \Omega}_N\}$

$$V(\mathbf{r}^{N}, \mathbf{\Omega}^{N}) = E_{\text{pair}}(\mathbf{r}^{N}, \mathbf{\Omega}^{N}) + E_{\text{ext}}(\mathbf{r}^{N}, \mathbf{\Omega}^{N})$$
(2.1)

where $E_{\rm pair}$ is the sum over all pair potential between the particles and describes the particle's shape, i.e. repulsion, and directed attraction, and $E_{\rm ext}$ is the potential energy coming from an external source such as a wall or gravitational field.

The difference between measuring observables in experiment and in simulation is the magnitude of numbers of atoms that are measured. As there are roughly 10^{24} water molecules in a glass of water, a experimental measurement captures an average over many molecules. Such experimental averages correspond to the thermodynamic limit, where the number of particles or molecules N approaches infinity. In simulations, representing such an immense number of particles is unfeasible, even if a single particle were encapsulated by just one bit. Fortunately, simulations do not require us to account for this extreme particle count.

Using statistical mechanics and the laws of thermodynamics, we can bridge the gap between the microscopic behavior of a limited number of particles and their macroscopic quantities measured in experiments. Central to understanding materials on a macroscopic scale is the free energy, since all thermodynamic behavior can be derived from it. While the free energy is often viewed as an abstract concept – it cannot be directly measured – statistical mechanics offers a framework to relate it to mechanical quantities, such as position and velocities, which can be measured in simulation. By minimizing the free energy, the system relaxes to a (thermodynamic) equilibrium. Subsequently, thermodynamics provides us with connections between measurable quantities, such as pressure P and temperature T, which are expressed as derivatives of the free energy, energy, and entropy.

To give the system the freedom to relax to a free energy minimum, one may fix three quantities in the simulation such as volume V, number of particles N, and temperature T referenced as the canonical ensemble. There exist alternative ensembles as well, such as the micro canonical, isobaric, grand canonical ensemble which keep for example the energy E, chemical potential μ or pressure P constant instead of N,V or T. Throughout this thesis, the theory and simulations are performed in the canonical ensemble which means that the free energy is the Helmholtz free energy F = U - TS with U the energy and S the entropy.

In general, and thus in all ensembles, an average may be calculated by:

$$\langle A \rangle = \sum_{i} P(i)A(i)$$
 (2.2)

where A is the observable of interest, e.g. pressure, chemical potential, conductivity, bond length, bending angle, or even prize money in a lottery, and P(i) is the probability of state i. For

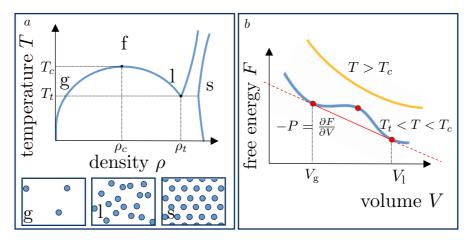


Figure 2.1: (a) A schematic phase diagram of an isotropically interacting mono-atomic substance, such as atomic Argon (Ar). The gas (g), fluid (f), liquid (l) and solid (s) state are indicated by the letters. The liquid is bound by (ρ_c, T_c) and (ρ_t, T_t) . At the bottom, a structural schematic illustration of particles in the gaseous, liquid and solid phase. (b) A schematic free energy curve for $T > T_c$ (yellow line) and $T_t < T < T_c$ (blue line). The red dots indicate equal pressure, and at $V_l < V < V_g$ (red solid line) the gas and liquid coexists, respectively. Note that the volume range only shows the gaseous and liquid, and not the solid phase.

microscopic objects, such as atoms, or patchy particles, the probability of state i is determined by its energy E_i and its degeneracy $\Omega(i)$

$$P(E) = \frac{\Omega(E_i) \exp(-\beta E_i)}{Q}$$
 (2.3)

$$= \frac{\Omega(E_i) \exp(-\beta E_i)}{\sum_j \Omega(j) \exp(-\beta E_j)}$$
 (2.4)

where $\beta=1/(k_{\rm B}T)$ is the inverse temperature, $k_{\rm B}$ is the Boltzmann constant, and T the temparture. The degeneracy $\Omega(i)$ is the number of states with energy E_i and is closely related to S, and Q, the partition function, is equal to $\sum_j \Omega(j) \exp(-\beta E_j)$ in the canonical ensemble. Other ensembles have different expressions for Q, but Eq. 2.3 still holds.

The partition function Q encompasses the full phase space which is often an impossibly complex and large function if there are many energy states, possibly with unknown degeneracy. However, Q defines the free energy as

$$F = -k_{\rm B}T\ln Q \tag{2.5}$$

and is therefore important when wanting to understand the system.

In the next sections, we will first discuss a theoretical description of mono-atomic substances. Using thermodynamic perturbation theory, we can find explicit expressions of the free energy and equations of state. If the systems are not so simplistic anymore, alternatively, one may resort to computer simulations. This thesis uses two, namely: Monte Carlo (MC), and Brownian Molecular Dynamics (BMD).

2.1.1 Phase Behavior

The three most simplistic phases of matter are the gaseous, the liquid and the solid state. Although there are many more phases, lets assume for now, those are the only states that exist. The gas phase is a low density phase such that particles most of the time are moving in a free path and rarely collide with each other. Therefore, the gas state shows no structural order. The solid phase is a high density phase where the particles are close enough to interact at all times leading to both short and long range order. The liquid state exists somewhere in between those two when the density is high enough and the temperature is low enough for the particles to attractively interact a significant amount of time, leading to short ranged order, but the density is too low to enforce long ranged order as solids show. Depending on the state variables density $\rho = N/V$ and temperature T, the system transitions through these (coexisting) phases (see Fig. 2.1a).

Why is a particular phase or coexistence favored under varying conditions? The answer lies in the system's inclination to minimize its free energy, thereby seeking its most stable state.

When the temperature is high, specifically $T>T_c$ (as illustrated by the yellow line in Fig. 2.1b) where T_c is the critical temperature, only one phase is stable: the fluid phase. The solid state can be reached in a continuous fashion, upon increasing the density, i.e. compression.

In the temperature range $T_t < T < T_c$ (depicted by the blue line in Fig. 2.1b) where T_t is the triple-point temperature, the free energy curve manifests inflection points. Then, multiple points on the free energy curve can share the same tangent, as indicated by the red dots. Between the red dots at the volume of the gas V_g and liquid V_l , a (linear) combination of a gas and liquid phase (red solid line) yields a lower free energy than tracing the blue curve of F. Notably, the third red dot, situated between V_l and V_g , remains inaccessible. It resides within the unstable region of the phase diagram where F adopts a concave shape. The critical T_c and triple-point T_t temperature act as an upper and lower bound for the liquid, respectively. Between T_c and T_t , through a first-order phase transition, a dilute fluid (gas) and dense fluid (liquid) coexist. Below T_t , the gas and solid phase coexist (Fig. 2.1a).

From the common tangent construction shown in Fig. 2.1b, we learn that at coexistence, the pressure P, that is $-\frac{\partial F}{\partial V}$, T and μ are equal in both phases (Eq. 2.6).

$$T_1 = T_2,$$
 $\mu_1 = \mu_2.$ (2.6)

with T, P and μ defined as (Eq. 2.7):

$$T = \left(\frac{\partial S}{\partial U}\right)_{V,N}, \qquad P = -\left(\frac{\partial F}{\partial V}\right)_{T,N}, \qquad \mu = \left(\frac{\partial F}{\partial N}\right)_{V,T}. \quad (2.7)$$

The phase behavior of simple fluids, such as the existence of the liquid phase and the breakdown of Boyle's law, had been for a long time not understood. In Van der Waals' thesis in 1873, he described molecules as elastic spheres with short range repulsion and long range attraction. He stated that the attractive intermolecular forces can lower the pressure, and that molecules, in contrast to what the ideal gas law assumes, occupy a region in space and effectively reduce

^{*}Boyle's law states that the pressure and the volume are inversely related to each other which is a good approximation for dilute systems

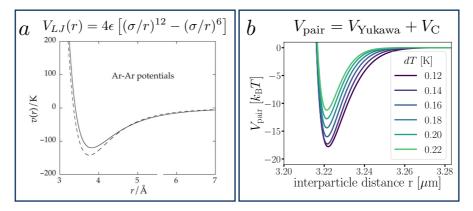


Figure 2.2: (a) The famous Lennard-Jones potential (solid line) that is able to mimic the phase behavior of argon (Ar) with $\epsilon/k_B=120$ K, and σ =3.4 Å. The dotted line is a pseudo potential based on gas phase measurements. From Ref. [111]. (b) The optimized pair potential for dipatch particles interacting via critical Casimir interactions from Chapter 3.

the volume V [109]. In 1880, Van der Waals wrote in his *Theorem of Corresponding States*, the following equation of state, i.e. an equation that describes the phase behavior of a system:

$$P = \frac{Nk_{\rm B}T}{V - b} - \frac{a}{V^2},\tag{2.8}$$

where a and b are material/potential dependent parameters: a is related to the effect of the attractive intermolecular forces, and b on the excluded volume of the particle. In 1910, he received the Nobelprize in physics for his work on the gas-liquid theory including his equation of state, as his elegant formula works for large range of real molecules capturing complex phase behavior such as the gas-liquid phase transition. [110]

These attractive intermolecular forces – called the Van der Waals force– originate from permanent or induced dipole-dipole interactions and density fluctuation of the electrons (dispersion forces). A simplistic potential that mimics this attraction, and became famous for reproducing the Van der Waals equation of state, is the Lennard-Jones (LJ) potential:

$$V_{LJ} = 4\epsilon [(\sigma/r)^{12} - (\sigma/r)^{6}], \qquad (2.9)$$

where σ is the particle diameter and ϵ is the minimum of the potential (see Fig. 2.2a). LJ mimics the long range dipole-dipole attraction ($\propto r^{-6}$) and writes the short-range repulsion in a convenient similar form as the attraction ($\propto r^{-12}$).

2.2 Thermodynamic Perturbation Theory

What the Van der Waals equation already suggests by its form, the properties of liquids can be deduced as a perturbation on the ideal gas; there is a correction term to the volume and pressure due to repulsion and attraction, respectively. Actually, particles that solely repel each other, also show a solid phase like depicted at Fig. 2.1a at high density. Thus, a significant part of the

structure, e.g. its radial correlation or structure factor, of interacting particles is determined by their repulsion which forms a basis for Thermodynamic Perturbation Theory. [111]

Thermodynamic perturbation theory (TPT), describes the free energy of system 1 as a perturbation on system 0 using a coupling parameter λ ,

$$F_{\lambda} = F_0 + \lambda (F_1 - F_0),$$
 (2.10)

which *couples* the two systems with corresponding free energies F_0 ($\lambda=0$) and F_1 ($\lambda=1$). Via a thermodynamic integration over λ in a simulation, one may calculate the free energy difference, F_1-F_0 , and deduce thermodynamic properties.

Alternatively, one may use a known free energy expression as the reference system. The simplest repulsive potential is the hard sphere (HS) potential that has an infinite repulsion at contact, i.e. $r < \sigma$ and zero interaction elsewhere (Eq. 4.28). With this type of interaction only excluded volume effects define phase behavior. Nonetheless, this highly simplified particle type already contains a lot of interesting physics and is the prime example of the importance of entropy. Hard spheres have therefore been (and still are) extensively studied to arrive at analytical expressions of its radial distribution function and free energy at various densities. Then, the perturbation $(F_1 - F_0)$ itself can be approximated through a Taylor expansion if the perturbation is weak and smooth, i.e., it does not show strong variations over λ , such as the LJ potential (Fig. 2.2a).

2.2.1 Wertheim Theory

Wertheim TPT enables one to predict thermodynamic properties of associating fluids through directed bonds bases on the interaction potential and density only. [112–115] Essential to Wertheim's theory, and the Statistical Associating Fluid Theory which is a reformulation of Wertheim's theory [116], is that the attractions are short ranged, unlike the LJ potential that has an attractive range of \pm 2.5 σ , and there can only form one bond per bonding site. For the setup of the patchy particles interacting through critical Casimir interactions and Yukawa repulsion, that have directional and deep attractive potentials, these assumptions hold (Fig. 2.2b).

As the attraction is sharp and short ranged, the perturbation cannot be performed directly through λ . Alternatively, Wertheim Theory uses the Mayer f-function:

$$f = \exp(-\beta U) - 1 \tag{2.11}$$

where U is the energy of the interacting system. Additionally, it uses the HS system as its reference (F_0) , and the attractive part of the potential is the perturbation $(F_1 - F_0)$.

Note that when using soft repulsive potentials in combination with perturbation theories that use the HS as a reference, a mapping onto the HS system is required. See Sec. 4.3.5 for this mapping of the Yukawa repulsion of the colloidal particles.

In Chapter 4, we extended the Wertheim Theory to inhomogeneous extremely confined systems and it gives a introduction to Wertheim Theory. As Wertheim's original papers are quite difficult to read, I suggest Ref. [117] as it explains the theory starting from statistical mechanics and graph theory.

Molecular Simulation Algorithms

In molecular simulations, particles are moved around to sample phase space to directly measure ensemble averages (Eq. 2.2), or sample the Helmholtz free energy (Eq. 2.5) as

$$F(\mathbf{q}) = -k_{\rm B}T \ln P(\mathbf{q}) + C \tag{2.12}$$

where $P(\mathbf{q})$ is the probability distribution as function of some reaction coordinate \mathbf{q} of interest, and C is an arbitrary constant.

In the coming sections, we will discuss Monte Carlo (MC), and Brownian Molecular Dynamics (BMD) that are algorithms to *move* the particles around in the simulation box. Depending on the research question, available resources and codes, one picks the algorithm that suits best. Each algorithm has its advantages and disadvantages that are explained next.

2.3 Monte Carlo

The name Monte Carlo originates from the equally named gambling city of the rich in Monaco. By gambling your way through new configurations of the system, you may lose or win some (energy). In contrast to what the players want that gamble at the casino, losing (energy in MC) is part of the game and actually part of the gain. MC is not only used in chemical physics, but also in other fields such as social sciences or finance.

The Monte Carlo algorithm –my personal favorite– is based on energies only (Eq. 2.1). Under certain circumstances, e.g. when derivatives of the energy, are complicated or unknown, or if you want to use constraints or restraints, MC can be easier to implement compared to molecular dynamics. The disadvantage is that MC, in principle, does not represent the dynamics of your system; it only gives you ensemble averages. However, if specific moves are used designed to mimic collective or dynamical motion, it could [118, 119]. At the same time, this is also the beauty of Monte Carlo as you are allowed to make nonphysical moves. While this may sound alarming when trying to simulate physical systems, it is not a problem as MC is an excellent method to calculate ensemble averages (Eq. 2.3).

The aim of Monte Carlo sampling is to create a collection of snapshots (configurations) that statistically represents the Boltzmann distribution of a relevant part of phase space. It does so by proposing trial *moves* to generate new configurations which are either accepted or rejected according to set of rules that render the correct distribution.

Systems in thermal equilibrium do not exhibit total net fluxes in state space. This means that the probability to transition from an old (o) configuration to a new (n) one, $o \to n$, is equal to its reverse, $n \to o$. This property is known as detailed balance:

$$P_o^{\text{eq}} W_{on} = P_n^{\text{eq}} W_{no} \tag{2.13}$$

$$P_o^{\text{eq}} P_{\text{gen}}(o \to n) P_{\text{acc}}(o \to n) = P_n^{\text{eq}} P_{\text{gen}}(n \to o) P_{\text{acc}}(n \to o)$$
 (2.14)

where $P_i^{\rm eq} = \exp(-\beta E_i)/Q$ with i=n or o is equilibrium probability of configuration with corresponding the energy E_i of the new and old configuration, respectively. The W is the transition matrix in a Markov chain, meaning that it only depends on the current configuration. Then

so, the transition matrix W is defined by the probability of generating the other configuration $P_{\rm gen}$ times the acceptance probability $P_{\rm acc}$.

In principle, only the ratio of the acceptance probabilities is important:

$$\frac{P_{\rm acc}(o \to n)}{P_{\rm acc}(n \to o)} = \frac{P_n^{\rm eq} P_{\rm gen}(n \to o)}{P_o^{\rm eq} P_{\rm gen}(o \to n)}$$
(2.15)

$$= \exp[-\beta (E_{\rm n} - E_{\rm o})] \frac{P_{\rm gen}(n \to o)}{P_{\rm gen}(o \to n)}$$
 (2.16)

which conveniently cancels the partition function Q in $P^{\rm eq}$ leaving only the energy difference between the two configurations.

In the original scheme proposed by Metropolis, $P_{\rm gen}$ is symmetric, i.e. their ratio in Eq. 2.16 is one. Then, given an old $\mathbf{x}_{\rm o}$ and a new $\mathbf{x}_{\rm n}$ configuration with corresponding energies $E_{\rm o}$ and $E_{\rm n}$, respectively, the probability of accepting the new configuration to the collection of snapshots is:

$$P_{\rm acc}(o \to n) = \begin{cases} \exp(-\beta \Delta E) & \text{if } \Delta E > 0\\ 1 & \text{if } \Delta E \le 0 \end{cases}$$
 (2.17)

where $\Delta E = E_{\rm n} - E_{\rm o}$. If the *move* leads to lowering the energy, i.e. $\Delta E \leq 0$, the new configuration is accepted. If the energy is increased, i.e. $\Delta E > 0$, the new configuration is accepted with probability $\exp(-\beta \Delta E)$. In practice, if random number $R < \exp(-\beta \Delta E)$, the new configuration is accepted. Then so, the new configuration is rejected $R \geq \exp(-\beta \Delta E)$. Mind that a rejection of $\mathbf{x}_{\rm new}$ means one should recount $\mathbf{x}_{\rm old}$ in the collection of snapshots.

So with MC sampling, the observable A is measured as:

$$\langle A \rangle = \frac{1}{L} \sum_{i=1}^{L} A_i \tag{2.18}$$

where L is the number of the Markov chain generated configurations according to the Boltzmann distribution. To calculate correct averages and standard deviations, it does not matter how or in which order the new configurations are made as the acceptance is only dependent on \mathbf{x}_i , not \mathbf{x}_{i-1} .

Now you might wonder, how the contribution of the entropy to the free energy is accounted for, if the acceptance rule is only energy based. But it is hidden in creating new configurations in $P_{\rm gen}$. States with (twice) more entropy, will be generated (twice) more often and thus will entropically contribute (twice) to the free energy.

Albeit MC's flexibility, versatility and broad range of application, there are a few essential ingredients when using it. First, detailed balance should hold. Second, your MC moves should allow you to be able to explore full phase space. Third, you sample phase space sufficiently. If these criteria are not met, you will not sample from the correct underlying distribution and your statistics will be wrong.

2.3.1 MC moves

There are no limitations on how to generate new configurations and the aim is to sample phase space *fast*. There is a sweet balance between generating configurations that lie far apart in phase space, but also accepting the new configurations sufficiently. Examples of moves used in this thesis are: single particle moves, cluster moves, and tail-flip moves.

SINGLE PARTICLE MOVES.

In single particles moves, you select a random particle and choose either translation or rotation (50/50%). For translations, the particle is translated along a random vector with a length $\in \langle 0, r_{\rm s,max} \rangle$. In the systems with a confining gravitational field along the z-axis, the z-value of the random vector is reduced by a factor of 10. This is to prevent that $E_{\rm n}$ becomes high by placing the particles inside the wall or against the gravitational field.

For rotations, the particle is rotated around its center of mass with an angle $\phi \in \langle 0, \phi_{s,max} \rangle$ in a random direction. Sec. 2.4.3 will explain how rotations on rigid bodies are performed. As the number of particles is constant, it follows the Metropolis acceptance rule (Eq. 2.17).

CLUSTER MOVES.

Cluster moves are performed in a similar fashion where both cluster rotations and translations are performed. A cluster is defined as group of particles connected via bonds. A bond is defined when two particles are attractively interacting though their patches, meaning that the attractive part of the pair potential (Eq. 3.6) is negative. The translation or rotation of clusters larger than a single particle have a much higher chance of creating new configurations that overlap with other particles in the system compared to a single particle. Hence, moves involving monomers, i.e. single particles, have significantly different acceptance probabilities that clusters larger than one. To improve the sampling with cluster moves, the maximal rotation and translation of monomers and larger clusters are set in different variables.

Translations are performed along a random vector of length $\in \langle 0, r_{\rm m, \, max} \rangle$ for the monomers, or $\in \langle 0, r_{\rm c, \, max} \rangle$ for any cluster of size larger than one. Random rotations are performed around the center of mass of a randomly selected particle with angle $\phi_{\rm m} \in \langle 0, 180^{\circ} \rangle$ for the monomers, and $\phi \in \langle 0, \phi_{\rm c, max} \rangle$ for any cluster of size larger than one.

In systems with gravity, the translation and rotation are not completely random as they would lead to configurations at which the particles are placed inside the wall or against the gravitational field. In these systems, the translation is restricted to the x,y-plane, by making a random vector with coordinates $\vec{r}=(x,y,0)$. The rotation is performed around $\hat{e}=(0,0,1)$, i.e. a rotation vector in the direction of the z-axis (see Sec. 2.4.3 for detailed description of performing rotations). From the quaternion, a rotation matrix is constructed that is able to perform the cluster rotation.

When performing cluster moves, an additional rejection criterion is defined. If a cluster move leads to the formation of a new bond, the configuration is rejected. This prevents the number of clusters to change during a cluster move, which is an easy way to keep $P_{\rm gen}=1/N_{\rm clusters}$ constant. This additional rejection criterion makes this scheme obey detailed balance and follow the Metropolis acceptance rule (Eq. 2.17).

Note that breakage of bonds is not possible when performing correct rotations and translations. However, if bonds do break during cluster moves, it is a sign that either the rotation of translation was not performed correctly. Specifically, one should be careful upon rotating a (large) cluster close to the periodic boundaries. See Sec. 2.5.3 for details.

TAIL-FLIP MOVES.

In Chapter 3, we measure bending rigidities of chains by combining single particle moves and tail-flip moves. The tail-flip moves are introduced to decorrelate the configurations of the semi-flexible chain faster. In this move, an interparticle bond vector \vec{r}_{bond} of the chain is randomly selected. Then, all particles starting from \vec{r}_{bond} to the tail, i.e. end of the chain, are rotated by 180° around this vector.

During these bending rigidity measurements, it was not desired that the chain would break. Therefore, an additional acceptance/rejection criterium was added to the single particle moves: if a bond breaks, the new configuration is rejected.

These few examples of MC moves, and additional rejection criteria, illustrate the freedom one has in creating or rejecting configurations which makes MC versatile.

2.4 Brownian Molecular Dynamics

The solvent molecules in a colloidal suspension are typically 3-4 order of magnitude smaller in radius than the colloidal particles. They collide with the surface of colloidal particles that leads to stochastic rotation and translation and viscous friction acting on the colloidal particles. When interested in collective and dynamical properties of colloidal particles, overdamped Langevin Dynamics, i.e. Brownian Molecular Dynamics (BMD) is the algorithm of choice. Unlike "regular" molecular dynamics that uses e.g. Velocity Verlet, the equation of motion of Brownian particles contains no inertial effects and mimic the stochastic thermal motion of the colloidal particles caused by the solvent molecules. [120]

The translational equation of motion of an (active) Brownian particle is

$$\vec{r}(t + \Delta t) - \vec{r}(t) = \mu_{\mathrm{T}}(\vec{F}_{\mathrm{A}} + \vec{F})\Delta t + \sqrt{2k_{\mathrm{B}}T\mu_{\mathrm{T}}\Delta t}\vec{\xi}$$
(2.19)

where \vec{r} is the positional vector of the particle, and t the time. The $\vec{F}=-dV/d\vec{r}$ is the force acting on the particle comes from the potential V, and the active force $\vec{F}_{\rm A}$ are only nonzero for the active particles. See Ref. [121] how to construct \vec{F} for anisotropic particles. The translational mobility tensor $\mu_{\rm T}=\beta D_{\rm T}\mathbb{1}$ with $D_{\rm T}$ translational diffusion, $\mathbb{1}$ the identity matrix, $\beta=1/k_{\rm B}T=1$ the inverse temperature with the Boltzmann constant $k_{\rm B}$, and the temperature T. The stochastic noise $\vec{\xi}$ is a vector where each element is i.i.d., with a zero mean and unit variance over time.

The rotational equation of motion is given by

$$\vec{\Omega}(t + \Delta t) - \vec{\Omega}(t) = \mu_{\rm R} \vec{\tau} \Delta t + \sqrt{2\mu_{\rm R} k_{\rm B} T \Delta t} \vec{\xi}$$
 (2.20)

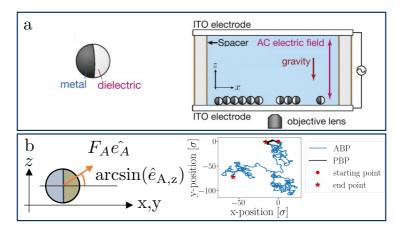


Figure 2.3: (a) In experiment, a Janus particle, that is composed of a hemisphere of metal and a hemisphere of dielectric material, will show an active propulsion if fueled by e.g. an AC field. Adapted from Ref. [122]. (b) A schematic illustration of an ABP with active propulsion vector $\vec{F}_A = F_A \hat{e}_A$ that makes an angle with respect to the wall (in the x,y-plane) indicated in orange. Two example trajectories of an active (ABP, $F_A = 50k_BT/\sigma$) in blue and passive Brownian particles (PBP) in black are shown.

where $\vec{\tau}$ is the torque acting on the particle coming from V, and $\mu_R = \beta D_R \mathbb{1}$ is the rotational mobility tensor with D_R rotational diffusion.

2.4.1 ACTIVE SYSTEMS

A widely used model to simulate self-propelling colloidal particles is the active Brownian particle (ABP). It consists of a self-propulsion force acting on the center of mass of the colloidal particle

$$\vec{F}_{A} = F_{A}\hat{e}_{A} \tag{2.21}$$

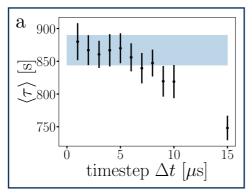
where F_A is the magnitude of the active force, and \hat{e}_A is a particle fixed unit vector that expresses the direction of the force as illustrated in Fig. 2.3b.

In an experimental setup, the Janus particle aligns its motion parallel to the wall, due to the applied AC field as illustrated in Fig. 2.3a [122]. Furthermore, the continuous presence of gravity prevents the active particles to self-propel against the gravitational field away from the wall [123]. As the exact response of the Janus particles to the AC field is quite complex [124], we mimic this behavior by including an effective alignment potential with magnitude[125–127]

$$V_{\text{align}}(\hat{e}_{A,z}) = \begin{cases} 0 & \text{ABP without gravity} \\ \frac{1}{2} \epsilon_{\text{align}} \arcsin^2(\hat{e}_{A,z}) & \text{ABP with gravity.} \end{cases}$$
(2.22)

where $\hat{e}_{\mathrm{A},z}$ denotes the z-component of the active force direction as defined in Fig. 2.3b. Note that this alignment acts as a restoring force that tries to minimize $\hat{e}_{\mathrm{A},z}$. The prefactor $\epsilon_{\mathrm{align}} = 500~k_{\mathrm{B}}T$ was chosen such that a lift-off of the particle against gravity did not occur.

Particles that contain a self-propulsion force $F_{\rm A}$ show an enhanced diffusion compared to their passive counterparts. Two example trajectories with the same time duration of single particles



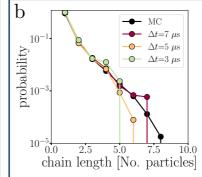


Figure 2.4: (a) The average lifetime of a dimer measured in 5000 breakage events shown with a 95% CI of the error of the mean. The blue horizontal bar is a guide to the eye to follow the 95% CI at $\Delta t = 2\mu s$. (b) The chain length distribution of dipatch particles in a box with N=20 particles and density $\rho = 0.253 N/\sigma^2$ in a system with gravity. Both tests are performed with the optimized potential at dT=0.16 K from Chapter 3.

with $D_{\rm T}$ =0.0035 $\sigma^2/{\rm s}$ and $D_{\rm R}$ =0.05 rad $^2/{\rm s}$ of a passive and an active Brownian particle with $F_{\rm A}=50\,k_{\rm B}T/\sigma$ are shown in Fig. 2.3b. These trajectories clearly show the enhanced diffusive behavior of active particles.

In active matter, the (dimensionless) Péclet number Pe expresses the relative importance of the propulsion speed from the active force compared to the diffusive Brownian motion. At low Pe, diffusive motion dominates, while at high Pe, active directed motion prevails. In the literature, multiple definitions of Pe are used, depending on e.g. the heterogeneity of the system, particle shape or anisotropy, or the range of the soft repulsion of the particle [128–132].

Here, we use the following definition:

$$Pe = \frac{v_0}{\sqrt{D_T D_R}} = \frac{\beta F_A \sqrt{D_T}}{\sqrt{D_R}}$$
 (2.23)

with $v_0=\beta F_{\rm A}D_{\rm T}$ the self-propulsion velocity, $D_{\rm T}$ the translational diffusion coefficient and $D_{\rm R}$ the rotational diffusion coefficient. [133, 134] The active force magnitudes of $F_{\rm A}$ = 0, 10, 50, and 100 $k_{\rm B}T/\sigma$ correspond to Pe=0, 2.6, 13.1, and 26.1 and are achievable in a typical experimental system.

2.4.2 Timestep Δt

All brute force BMD simulations are performed with a translational and rotational diffusion constant as measured in experiment of dipatch particles with diameter $\sigma=3.2\mu\mathrm{m}$ and equal D_{T} =0.0035 σ^2/s and D_{R} =0.05 rad $^2/\mathrm{s}$, respectively [56]. The timestep was tested in two system using the optimized potential at dT=0.16 K from Chapter 3.

In the first system, the lifetime of a patchy particle dimer consisting of two particles in a system without gravity is measured. Starting from the bound state, 5000 brute force BMD simulations are performed until the particles separate $1/2\sigma$ and the bond was defined as broken. The average lifetime of the bond is measured and is shown with a 95% confidence interval (CI) of the error

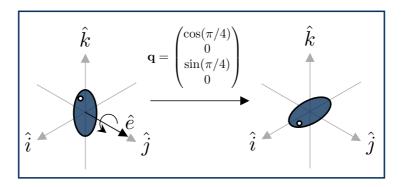


Figure 2.5 : The object on the left, is rotated around \hat{e} with angle θ by the quaternion $\mathbf{q} = (\cos \pi/4, 0, \sin \pi/4, 0)$ (Eq. 2.27) to yield to object on the right.

of the mean in Fig. 2.4a. A timestep upto Δt =6 μs falls well into the 95% CI of the smallest timestep.

The second system consists of N=20 dipatch particles interacting in a gravitational field. The chain length distribution is shown at multiple values of Δt in Fig. 2.4b. The largest tested timestep of Δt =7 μ s shows excellent agreement with the MC simulations.

To be on the save side, a timestep of Δt = 5.0 μ s was chosen to perform all BMD simulations with at all interaction strengths defined by dT.

2.4.3 Rigid Body Rotations & Quaternions

Numerically performing subsequent rotations of rigid bodies may lead to spurious behavior such as Gimble lock or drifting rotational dynamics [120]. Therefore, rotations of rigid bodies are performed using quaternions that are a four dimensional representation of 3D rotations. [135]

Similar to the rotation of a two dimensional vector that can conveniently be expressed using imaginary numbers, rotations of three dimensional vectors can also be expressed using imaginary numbers. For this, a quaternion the following form:

$$\mathbf{q} = a + b\hat{i} + c\hat{j} + d\hat{k} \tag{2.24}$$

where a, b, c, and d are real numbers, and \hat{i}, \hat{j} , and \hat{k} are its basis vectors in the imaginary dimension such that:

$$i^2 = j^2 = k^2 = ijk = -1 (2.25)$$

A rigid body rotation, as schematically illustrated in Fig. 2.5, can be expressed as a rotation of angle θ around a vector \hat{e} that is defined on the quaternion's basis vectors \hat{i} , \hat{j} , and \hat{k} . The resulting unit quaternion is:

$$\mathbf{q} = \exp\left(\frac{\theta}{2}(e_x\hat{i} + e_y\hat{j} + e_z\hat{k})\right) \tag{2.26}$$

$$= \begin{pmatrix} \cos(\theta/2) \\ \hat{e}_x \sin(\theta/2) \\ \hat{e}_y \sin(\theta/2) \\ \hat{e}_z \sin(\theta/2) \end{pmatrix}$$
 (2.27)

which is thus easily constructed by θ and \hat{e} .

Subsequent rotations $\mathbf{q_1}$ and $\mathbf{q_2}$ are performed as a vector product $\mathbf{q} = \mathbf{q_1} \cdot \mathbf{q_2}$ resulting:

$$\mathbf{q} = \begin{pmatrix} a_1 a_2 - b_1 b_2 - c_1 c_2 - d_1 d_2 \\ a_1 b_2 + b_1 a_2 + c_1 d_2 - d_1 c_2 \\ a_1 c_2 - b_1 d_2 + c_1 a_2 + d_1 b_2 \\ a_1 d_2 + b_1 c_2 - c_1 b_2 + d_1 a_2 \end{pmatrix}$$
(2.28)

where $\mathbf{q_i} = (a_i, b_i, c_i, d_i)$.

The 3D rotation matrix $\mathbf{R}(\mathbf{q})$ is calculated via:

$$\mathbf{R}(\mathbf{q}) = \begin{pmatrix} a^2 + b^2 - c^2 - d^2 & 2(bc - ad) & 2(bd + ac) \\ 2(bc + ad) & a^2 - b^2 + c^2 - d^2 & 2(cd - ab) \\ 2(bd - ac) & 2(cd + ab) & a^2 - b^2 - c^2 + d^2 \end{pmatrix}$$
(2.29)

where a, b, c, and d are as defined in Eq. 2.24.

Then, in the simulation, the direction of a patch on a patchy particle can be described using a *basis* patch vector and a quaternion that you define in the input files given to the code. This basis description of the patchy particle, the location of the patch, is described with a patch vector \mathbf{p} , e.g. $\mathbf{p}=(1,0,0)$. Then if in a configuration the patch is for example oriented on the z-axis, the particle's quaternion is $\mathbf{q}=(\cos\pi/4,0,-\sin\pi/4,0)$, i.e. a θ =90° rotation around $\hat{e}=(0,-1,0)$ of $\mathbf{p}=(1,0,0)$. In practice, each particle has its own *current* quaternion that allows you to calculate the *current* orientation of each patch via the rotation matrix in Eq. 2.29. By simply multiplying the quaternion of the particle with a new quaternion (Eq. 2.28), the particle's orientation is adjusted.

2.5 MEASURING

Most measured observables are detailed in the method sections of each chapter. However, here is a deeper explanation of determining rate constants for rare events from simulations, MC integration, and depth-first search .

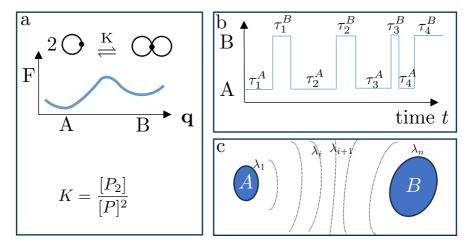


Figure 2.6: (a) A schematic illustration of two monovalent patches reacting into a dimer along a reaction coordinate \mathbf{q} . The two states at a local free energy minimum are separated by a free energy barrier. (b) The height of the barrier determines the rate at which the systems transitions between the states. In a time series, one may observe the times at which the system resides in A or B. (c) In TIS, the rate is calculated using interfaces λ (dotted lines) defined between the states A and B.

2.5.1 Transition Rates of Rare Events

In both chemistry and physics, numerous processes, such as chemical reactions, protein folding, and self-assembling activities, occur over significantly larger timescales than the system's smallest timescales, such as the vibrational timescale of chemical bonds. Additionally, the free energy barrier of these processes can be so elevated that the system becomes *stuck* in a local free energy minimum. As a result, observing these transitions in simulations becomes increasingly rare and makes observing rare events inherently a stochastic process. [136]

Imagine two monovalent patchy particles in a (small) simulation box and phase space is sampled using a molecular dynamics algorithm, e.g. Brownian Dynamics, to recover a free energy profile (Fig. 2.6a). Over time, the systems transitions between the monomeric state (A), where the patches are unbound, and the dimer state (B), where the patches are bound, as schematically illustrated in Fig. 2.6b. The transitions itself between the two states are fast, but the times, indicated by τ_A and τ_B between the transitions are relatively long.

There are several ways to determine the rate constant of such a stochastic process:

- using the mean first passage time au_{MFPT} ,
- using the flux and transition interface sampling (TIS) [137], or
- via the survival probability $P_{\rm S}$,

MEAN FIRST PASSAGE TIME

Assuming there are many transitions observed between state A and B, and the systems has visited phase space sufficiently in the simulation, that is in the limit of $t\to\infty$, the rate of transitioning from state A to B converges to:

$$k_{AB} = \lim_{t \to \infty} N_{A \to B}(t) / \sum_{i} \tau_i^A(t)$$
 (2.30)

which is $N_{A\to B}$ is the number of transitions from A to B observed at time t divided by the total time spent in A equal to $\sum_i \tau_i^A$. The inverse of this equation is

$$k_{AB}^{-1} = \lim_{t \to \infty} \sum_{i} \tau_i^A(t) / N_{A \to B}(t)$$
 (2.31)

$$= \langle \tau_A^{\text{MFPT}} \rangle \tag{2.32}$$

which yields the mean first passage time $\langle \tau^{\rm MFPT} \rangle.$

This method has been used in Chapter 5 where many brute force simulations are performed, halted after reaching the broken state, to determine the rate of breakage through the mean first passage time.

TRANSITION INTERFACE SAMPLING

In transition interface sampling (TIS), the phase space between state A and B is separated by interfaces λ as illustrated in Fig. 2.6c [136, 137]. The first interface λ_1 defines the boundary of state A, and following the interfaces, the system ends up at B that is defined by the last interface λ_n .

The rate can be calculates as

$$k_{AB} = \phi_{1,0} \prod_{i=2}^{n} P(\lambda_i | \lambda_{i-1})$$
 (2.33)

where $\phi_{1,0}$ is the flux through the first interface, and $P(\lambda_i|\lambda_{i-1})$ is conditional probability of reaching interface λ_i given that you came from λ_{i-1} . The flux can be calculated as the average time between positive transition, i.e. from state A to outside state A, though the first interface. The conditional probabilities can be separately measured in many uncorrelated simulations as done in TIS, or it is measured in many single brute force simulation runs starting in A and halted in B as done in Chapter 5.

SURVIVAL PROBABILITY

Lastly, the rate can be calculated through the survival probability. The time distribution of consecutive events in a Poisson process, governed by a timescale τ that does not vary significantly over time, is exponentially distributed.

An exponential distribution f is defined as:

$$f(t) = \frac{1}{\tau} \exp(-t/\tau) \tag{2.34}$$

where t is time and $\tau = 1/k$ is the inverse rate.

Then, the survival probability of an exponential distribution is:

$$P_S(t) = 1 - F(t) (2.35)$$

$$=1-\int_{0}^{t}\frac{1}{\tau}\exp(-t/\tau)dt$$
 (2.36)

$$=1-(-\exp(-t/\tau)|_{0}^{\infty}) \tag{2.37}$$

$$= 1 - (1 - \exp(-t/\tau)) \tag{2.38}$$

$$= \exp(-t/\tau) \tag{2.39}$$

with F the cumulative distribution function, or the cumulative probability of being transitioned at time t. By measuring the survival probability as function of a time interval t, the rate k can be measured by a fit of the exponential decay of P_S .

In Chapter 6, this method is used. In these systems, there might not be many bonds that are formed or broken in the brute force simulations, making the method of using the mean first passage time inaccurate as the MFPT method works particularly well if there are many independent samples of the rare event. Additionally, when fitting τ via the the survival probability, it is not necessary that all bonds to be broken at time t.

2.5.2 MC Integration

In chemical and physical systems, Monte Carlo (MC) methods are frequently employed for sampling equilibrium statistics, as elucidated in 2.3. However, MC methods also serve as a potent tool for computing complex integrals by computing the average of a function f that may depend on a high-dimensional space \mathbf{x} in volume V. Similar to Equation 2.2:

$$\langle f \rangle_V = \frac{\int_V f(\mathbf{x}) d\mathbf{x}}{\int_V d\mathbf{x}}$$
 (2.40)

where the brackets $\langle \rangle$ indicate the average. Since MC methods allow for easy averaging in volume V, we obtain:

$$\int_{V} f(\mathbf{x}) d\mathbf{x} = \langle f \rangle_{V} \int d\mathbf{x}$$
 (2.41)

$$= \langle f \rangle_V V \tag{2.42}$$

Therefore, the complex integral on the left-hand side can be estimated by the product of the function average in the volume and the volume itself.

In Chapter 4, we combined both MC sampling and MC integration to determine the reaction constants of self-assembling highly confined dipatch particles.

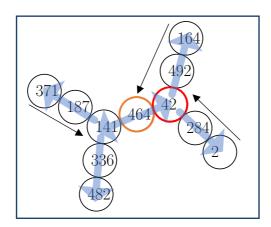


Figure 2.7: Schematic illustration of a colloidal architecture composed of divalent and trivalent particles with their particle number written in their center. DFS (Listing 2.1) starts at particle number 464 indicated by the orange color. By following the transparent blue arrows shown on top of the colloidal architecture, DFS walks over the bonds. If particle 2 is reached, DFS escapes its nested loops, by walking back over the structure to the last visited branch point at particle 42, indicated by the red color. From there, it continues to particles 492 until the full structure has been visited.

2.5.3 Depth First Search

The algorithm Depth First Search (DFS) is an algoritm that allows one to follow the connections of a graph, or bond of a colloidal architecture in this case. In the code, DFS is used, for example, to count the size distribution of rings in a colloidal network architecture [57–59], or when one wants to rotate a cluster in rotational MC cluster moves. In the latter, it is important that the coordinates of the particles do not cross the periodic boundaries, else the cluster will break upon rotating. DFS will help to create new coordinates of the cluster.

The DFS function shown below in Listing 2.1, makes smart use of a nested loop, by recalling DFS inside DFS, to walk systematically over the structure. Before the DFS starts, all particle numbers in the cluster have been identified and saved in a dynamic integer array defined as IntArray particlesleft_list. Then, DFS is called on the particle ipart and walks over its bonds. If the bound particle jpart has not been visited yet, it will continue with DFS on jpart indicated by the blue transparent arrows in Fig. 2.7. If jpart has been visited already, as tracked by the dynamic integer array IntArray particlesleft_list, it can continue the loop over the other bonds. If the end of a chain is reached, e.g. at particle 2, the algorithm escapes the nested loop walking back over the structure until it arrives at the last visited branch point at particle 42, as indicated by the thin black arrow drawn outside the structure in Fig. 2.7.

```
void DFS(Slice *psl,int ipart, IntArray *particlesleft_list, Slice *copyslice ){
// Depth First Search adapted from https://www.codewithharry.com/videos/data-structures-and-algorithms-in-hindi-89/
// Adapted by HJ Jonas, specifically to gives particle in a cluster new coordinates that not cross the periodic boundaries. Important to do when performing cluster rotations in MC.
// it walks over the particles and performs DPF, and makes smart use of a nested loop, by recalling DFS inside DFS, to walk over the structure
// Slice *psl contains the particle coordinates and bond information
```

```
// int ipart is the particle on which DFS is performed
        // IntArray *particlesleft_list is the dynamical list of integers that tracks which particles
        have not been visited yet.
        // Slice *copyslice is a copy of Slice, but with updated coordinates of the cluster. (used for
        rotating cluster is MC)
10
         vector dr;
11
        int jpart;
        // remove ipart from list, else you will find the bond back to ipart. Now you will walk forward
14
         removeElementXIntArray(particlesleft_list, ipart);
         // loop over the bound particles of ipart, to see if you have visited them
         for (int n = 0; n < psl->pts[ipart].nbonds; n++){
18
          jpart=psl->pts[ipart].bonds[n]; // the next bound particles to ipart;
2.0
           // did you already visit jpart?
            \textbf{if(checkElementXIntArray(particlesleft\_list, jpart ))}  \{ \ // \ \text{checkElementXIntArray returns 1 if} 
        jpart is in the list.
            // new position jpart
23
            dr=particles_vector(psl, jpart,ipart);
24
             vector_add(copyslice->pts[ipart].r,dr,copyslice->pts[jpart].r);
26
27
             // now perform DFS on jpart
             DFS( psl,jpart, particlesleft_list, copyslice );
28
           }
30
         }
31
         return;
32
    }
33
```

Listing 2.1: Depth First Seach code written in c.

A TEMPERATURE-DEPENDENT CRITICAL CASIMIR PATCHY PARTICLE MODEL BENCHMARKED ONTO EXPERIMENT

Synthetic colloidal patchy particles immersed in a binary liquid mixture can self-assemble via critical Casimir interactions into various superstructures, such as chains and networks. Up to now, there are no quantitatively accurate potential models that can simulate and predict this experimentally observed behavior precisely. Here we develop a protocol to establish such a model based on a combination of theoretical Casimir potentials and angular switching functions. Using Monte Carlo simulations, we optimize several material-specific parameters in the model to match the experimental chain length distribution and persistence length. Our approach gives a systematic way to obtain accurate potentials for critical Casimir induced patchy particle interaction and can be used in large-scale simulations.

3.1 Introduction

Advances in colloid chemistry have enabled the synthesis of micron-sized particles that, when immersed in a near-critical binary liquid mixture (e.g. water and lutidine), experience anisotropic directional interactions induced by a critical Casimir force. As such patchy particles can make directed bonds, i.e. only one bond per patch, they can be viewed as mesoscopic analogs of (carbon) atoms [63]. Their micron-sized scale makes them directly observable via a confocal microscope, while they simultaneously still experience thermal motion that lets them obey the same statistical behavior of molecules and atoms, i.e. the Boltzmann distribution. Hence, colloidal patchy particles are well suited as an experimental model system to explore complex structures analogous to molecular architectures. Indeed, by exquisite temperature control of the Casimir interaction, patchy particles can form colloidal architectures, such as chains and rings, revealing molecular-like structures [53, 57].

Much experimental work has been performed on the self-assembly of patchy particles [38, 47, 138, 139] and many computer simulations have investigated generic static and dynamic properties [43, 140–146]. However, most common colloidal interaction models cannot reproduce or predict experimental observation because this behavior is sensitive to the precise form of the effective interactions at the experimental conditions, as dictated by the material and solvent properties.

In this work, we aim to develop an accurate model for patchy particle systems that can quantitatively predict the outcome of experiments. Such models would have several advantages. First, it would be possible to mimic the experimental setup and understand what is happening on the particle level, e.g. the conformational ring statistics in Ref. [57]. As such, simulations bring structural and dynamical insight into the experimental observations. Second, accurate potentials used in a multi-scale simulation provide large-scale and long-time behavior, enabling the exploration of new hypotheses. Moreover, such simulations will serve as a predictive tool and provide a guide to design future experiments. Finally, our work shows a systematic road toward the development of accurate effective patchy particle potentials.

While in previous work [44], we developed a potential for (experimental) dumbbell particles where two sites are both interacting isotropically, here we focus on spherical particles with directional patches. In the experimental realization of the system, a small patch is exposed at the surface of a colloidal particle made of a different material. The specific wetting properties of the patch and the colloidal particle material with respect to the two components of the near-critical liquid mixture induce the Casimir interactions between the patches [147–149].

The model we develop for simulating patchy colloidal particles is based on theoretical (isotropic) pair potentials valid for spherical colloidal particles immersed in an off-critical binary liquid. The Yukawa potential describes the repulsive part, and the attractive part originates from the critical Casimir interactions [72, 83]. As the theoretical potentials are constructed for a particle with a radius matching the radius of curvature of the patch on the patchy particle of interest, we assume prior knowledge of its geometry. Additionally, these isotropic potentials depend on properties of the solvent and the colloidal particle and contain two imprecisely known parameters: the surface charge density and the wetting scaling parameter.

Next, we model the patches of the colloidal particle by multiplying the isotropic interaction by a switching function, which decays from one to zero, interpolating between a fully bonded and a non-bonded configuration, depending on the relative orientations of the interacting patches.

The precise form of this switching function is computed by performing an explicit numerical integration over the two patch surfaces at various orientations.

As there are several unknown parameters in the theoretical potentials, it is not easy to come up with an entirely bottom-up approach. Therefore, we adopt a hybrid top-down, bottom-up procedure and parameterize the potential by benchmarking it on experimental measurements.

Implementing the full potential for a colloidal dipatch particle system, we performed extensive Monte Carlo simulations for colloidal systems under gravity. As expected, the particles assemble into chains for sufficiently strong attraction and we measure the persistence length and chain length distributions at various temperatures (Fig. 3.1). The potential is then matched to mimic the experimental results by tuning the surface charge density, scaling wetting parameter and patch size.

The remainder of the paper is organized as follows. In section II, the patchy particle model is presented, which is based on the physical dimensions of the patchy particle, theoretical critical Casimir interactions, and electrostatic repulsion, section III shows details of the simulated system to calculate the chain length distributions and persistence lengths, and in section IV, we show the effects of the fitting parameters on the two observables and the optimization of the potential. We end with concluding remarks.

3.2 Theoretical Background

Following the bottom-up approach, we start with introducing the pair potential of isotropic particles immersed in a binary liquid, followed by the pair potential of patchy particles. Then, by adding the external gravitational field, the full potential is constructed.

Next, we apply our general model onto the dipatch particle system that is based on physical dimensions of the experimentally measured particles.

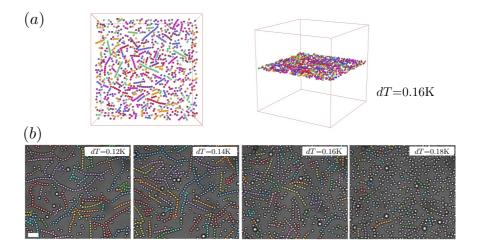


Figure 3.1: (a) A top and side view from the simulation box at dT = 0.16K. (b) Snapshots from experiment at various temperatures [53]. Distinct chain are indicated by the colors.

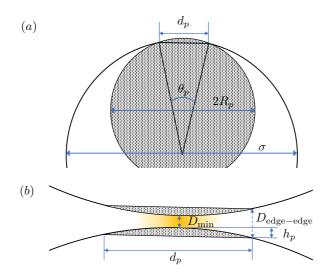


Figure 3.2: (a) The computational patchy particle is composed out of two components: the bulk colloidal particle (white circle), and the patch colloidal particle (dotted circle). (b) A schematic illustration zoomed in at the bond of two patchy particles. If θ_p is large enough, the $D_{\rm edge-edge}$ falls outside the range of $V_{\rm isotropic}$ and only a small fraction of the patch surfaces interacts, as illustrated with the yellow color. The patch height h_p , the projected patch diameter d_p , the patch surface-surface distance D_{\min} and $D_{\rm edge-edge}$ are indicated (dotted lines).

3.2.1 The isotropic pair potential

The isotropic pair potential is based on the work of Stuij *et al.* [72], which presented a model for the attractive critical Casimir potential between two spherical colloidal particles immersed in an off-critical binary liquid. The model is constructed by mapping experimentally measured radial distribution functions and second virial coefficients, onto pair potentials based on critical Ising model Monte Carlo simulations and mean-field theoretical methods [150].

These isotropic potentials $V_{\rm isotropic}$ are composed of the repulsive Yukawa potential $V_{\rm Yukawa}$ and the attractive critical Casimir potential obtained from the theoretical scaling function $V_{\rm C}^{\rm theory}$. Their isotropic nature makes them a function of the interparticle distance r only.

$$V_{\text{isotropic}}(r) = V_{\text{Yukawa}}(r) + V_{\text{C}}^{\text{theory}}(r)$$
 (3.1)

The potential $V_{\rm Yukawa}$ describes the screened Coulomb repulsion between the colloidal particles in a polar solvent. It is a coarse-grained model that captures the screening effect of the electric double layer of the ions in the solvent [151, 152]. The Yukawa potential of two identical charged particles with diameter σ_c and a center-to-center distance r apart is:

$$V_{\text{Yukawa}}(r) = \begin{cases} \infty, & r \leq \sigma_c \\ U_0 \exp(-\kappa(r - \sigma_c))\sigma_c/r, & r > \sigma_c \end{cases}$$
(3.2)

with

$$U_0 = \frac{Z^2 \lambda_{\rm B}}{(1 + \kappa \sigma_c/2)^2 \sigma_c},\tag{3.3}$$

where $Z=\pi\sigma_c^2\Upsilon$ is the charge of the particles, Υ the surface charge density, $\lambda_{\rm B}=\beta e^2/4\pi\epsilon$ the Bjerrum length of the solvent where ϵ is the permittivity of the solvent, e the elementary charge, and $\beta=1/k_{\rm B}T$ the inverse temperature with $k_{\rm B}$ the Boltzmann constant. The screening length, i.e. Debye length, is defined as $\kappa^{-1}=\sqrt{\epsilon k_{\rm B}T/e^2\sum_i\rho_i}$ where ρ_i is the number density of monovalent ions in the solvent [153].

The attraction is caused by critical Casimir interactions resulting from the diverging bulk correlation length ξ of the concentration fluctuations of a binary solvent near its critical point. The surfaces of two spherical particles, or differently shaped objects such as walls, patchy particles or cubes [82, 154–156], act as boundary conditions (BCs) confining the fluctuations between them. When the distance between the objects becomes smaller than ξ , the spatial restriction on the critical fluctuations gives rise to an effective force, called the critical Casimir force, first introduced by Fisher and de Gennes in 1978 [80]. This effective force is attractive or repulsive force depending on the identical or opposing surface preference of the BCs. In the theoretical description, this surface preference is captured by so-called surface fields h_s that depend on a material-specific (dimensionless) wetting parameter w, i.e. the hydrophilic or -phobic affinity of the surface with the solvent [82, 157, 158].

The critical Casimir interaction between two spheres of radius R_p follows a universal scaling function $\hat{\Theta}$ according to finite-size scaling theory (see Appendix Sec. 3.6.1)

$$V_{\rm C}^{\rm theory}(r) = \frac{w^3 R_p}{D} \hat{\Theta}^{(d=3,\text{Derj})}(\mathcal{Y}/w, \Lambda), \tag{3.4}$$

where distance $D=r-2R_p$, and r the interparticle distance of the two particles with radius R_p . This form holds for two spheres with $R_p\gg D$, in the Derjaguin approximation in three dimensions (d=3).

The first variable in the scaling function $\mathcal{Y} \equiv \mathrm{sgn}(t)D/\xi_t$ is dependent on the scaled temperature $t = (T_c - T)/T_c$ with T_c as the critical temperature and T the temperature, and the solvent correlation length $\xi_t \equiv \xi_{t,\pm}^{(0)} |t|^{-\nu}$ along the path $t \to 0^\pm$ at the critical composition. The second variable in the scaling function $\Lambda \equiv \mathrm{sgn}(h_b)D/\xi_h$ depends on the bulk ordering field h_b . The bulk ordering field is proportional to the difference between the chemical potentials of the solvent species A and B such that $h_b \sim \mu_A - \mu_B - (\mu_A - \mu_B)_c$ with respect to the critical point. The related solvent correlation length is $\xi_h = \xi_h^{(0)} |h_b|^{-\nu/\beta\delta}$ along the path $h_b \to 0$ with t=0. While the scaling exponents ν,β,δ , and the amplitude ratio $\xi_{t,+}^{(0)}/\xi_{t,-}^{(0)}$ are universal [71], the magnitude of the amplitudes of $\xi_{t,\pm}^{(0)}$ and $\xi_h^{(0)}$ is not.

The universal scaling behavior means that the critical Casimir interactions are largely independent of microscopic details of the system but are instead a function of the thermodynamic state of the solvent and the properties of the boundary conditions. The former includes the composition of the binary liquid c, salt concentration $c_{\rm salt}$, and phase separation temperature T_{cx} , and the latter is a function of the radius R_p of the particle, and scaling wetting parameter w.

3.2.2 The patchy particle pair potential

For the construction of the patchy particle pair potential, consider a patchy particle that consists of a spherical bulk particle of diameter $\sigma=2R$ with n_p spherical patch particles with a radius R_p , located such that the patch particle cuts through the surface of the bulk particle, yielding a exposed circular patch of diameter d_p (see Fig. 3.2a).

Due to the short nm-ranged character of the critical Casimir interaction, which is at least an order of magnitude smaller than the particle diameter, only a small area of the exposed patch surfaces interacts. While in principle there is also a bulk-bulk Casimir attraction, this is relatively weak compared to the patch-patch attraction and will be dominated by the repulsive electrostatic potential at the experimentally chosen conditions. We can therefore neglect these interactions. Note that the situation would be reversed for compositions on the other side of the critical composition.

Suppose two patchy particles are facing each other at their minimum energy position. In that case, the bulk particle and the edges of the circular patch surface do not contribute to the effective interaction calculated in the Derjaguin approximation, as this distance $\geq D_{\rm edge-edge}$ (see Fig. 3.2b) falls outside the range of the critical Casimir interaction. Therefore, the effective interaction between two facing patches of two particles is accurately approximated by the isotropic pair potential (Eq. 3.1) of two spherical particles with radius R_p .

The pair interaction $V_{\rm pair}$ between the patchy particles arises from the electrostatic repulsion $V_{\rm Yukawa}$ and the patch-patch attractive interaction

$$V_{\text{pair}}(r_{ij}, \Omega_i, \Omega_j) = V_{\text{Yukawa}}(r_{ij}) + \min_{1 \le k, l \le n_p} V_{\mathbf{p}_{ik}, \mathbf{p}_{jl}}(r_{ij}, \Omega_i, \Omega_j)$$
(3.5)

where the min function gives the minimum energy of the set of all possible patch-patch potentials. The position of each patch in the particle reference frame is given by n_p unit vectors $\mathbf p$ which point from the particle's center to the center of the patch. This mimics the fact that only one bond per particle pair can be formed. This patch-patch potential $V_{\mathbf p_{ik},\mathbf p_{jl}}$ is defined as

$$V_{\mathbf{p}_{ik},\mathbf{p}_{jl}}(r_{ij},\Omega_i,\Omega_j) = V_{\mathbf{C}}^{\text{theory}}(r_{ij})S_{\mathbf{p}_{ik},\mathbf{p}_{jl}}(\Omega_i,\Omega_j)$$
(3.6)

where $V_{\rm C}^{\rm theory}(r_{ij})$ is the (isotropic) critical Casimir attraction for two particles with diameter $2R_p$ given in Eq. 3.4. The switching function $S_{{\bf p}_{ik},{\bf p}_{jl}}(\Omega_i,\Omega_j)$ captures the effective interaction strength as function of the particles' orientation Ω (given by a quaternion representation). The strongest bond is formed if the patches are aligned, as illustrated in Fig. 3.2b, yielding S=1. The bond weakens when patches are rotated away, rendering $S\in[0,1)$.

3.2.3 The switching function

This switching function is in principle six-dimensional (three degrees of freedom for each orientation Ω). However, by making use of the symmetry of the system, it reduces to three dimensions. To do so, we define three angles θ_i , θ_j , and θ'_{ij} and a distance r to represent all conformations

that two particles can have when making a bond. In Fig. 3.3 on the left, the θ_i and θ_j angles are illustrated. They are defined as:

$$\cos(\theta_i) = \frac{\mathbf{p}_{ik} \cdot \mathbf{r}_{ij}}{|\mathbf{p}_{ik}||\mathbf{r}_{ij}|}, - \cos(\theta_j) = \frac{\mathbf{p}_{jl} \cdot \mathbf{r}_{ij}}{|\mathbf{p}_{jl}||\mathbf{r}_{ij}|}$$
(3.7)

where $\mathbf{p}_{ik}(\mathbf{p}_{jl})$ is the kth(lth) patch vector of particle i(j), and $\mathbf{r}_{ij} = \mathbf{r}_j - \mathbf{r}_i$ is the interparticle center-to-center distance vector. The angle θ'_{ij} is defined as the patch vectors' projected angle on the plane perpendicular to the interparticle vector as illustrated in Fig. 3.3 on the right. Note that by aligning the reference frame with \mathbf{r}_{ij} , we can make this representation rotationally and translationally invariant. In this way, the six-dimensional function $S_{\mathbf{p}_{ik},\mathbf{p}_{jl}}(\Omega_i,\Omega_j)$ is reduced to a three-dimensional function $S(\theta_i,\theta_j,\theta'_{ij})$.

The function $S(\theta_i, \theta_j, \theta'_{ij})$ can be computed by a numerical integration of the effective attractive critical Casimir interaction at various conformations defined by θ_i , θ_j , and θ'_{ij} . To simplify the integration, the patch curvature is set equal to the curvature of the bulk particle. In the Appendix Sec. 3.6.4, we show that the integrated function $S(\theta_i, \theta_j, \theta'_{ij})$ can be well approximated by

$$S(\theta_i, \theta_j, \theta'_{ij}) \approx S'(\theta_i)S'(\theta_j)$$
 (3.8)

where $S'(\theta_i)$ depends only on one angle and is a fit of the part of the integrated $S(\theta_i, \theta_j, \theta'_{ij})$ where one of the particles is fixed at θ_j =0°, while the other is rotated by $\theta_i \ge$ 0°:

$$S'(\theta) = \exp\left(\sum_{l=2}^{8} c_l \theta^l\right) \tag{3.9}$$

In a self-assembled patchy particle dispersion, the persistence length and distribution of the chain lengths are not strongly affected by the choice of the definition of S by either θ_i , θ_j , and θ'_{ij} or making the simplification of only incorporating θ_i and θ_j as in Eq. 3.8. See the Appendix Sec. 3.6.4for more details.

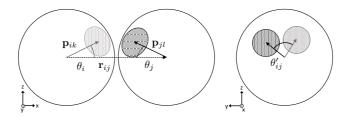


Figure 3.3: Two single patch particles with their interparticle vector \mathbf{r}_{ij} (dotted arrow) and patch vectors \mathbf{p}_{ik} and \mathbf{p}_{jl} (solid arrows). The light and dark grey colored patch are behind and in front of the plane of the paper, respectively. The angles θ_i , θ_j , and θ'_{ij} are indicated with a bow.

3.2.4 The external potential $V_{ m gravity}$

To mimic the experimental observation that patchy particles tend to sink to the bottom of the sample due to the gravitational force F_g pulling the colloids down, we add an external gravitational potential to the model. The gravitational potential V_g

$$V_q(z) = \Delta mgz = -F_q z, \tag{3.10}$$

depends on gravitational acceleration (on Earth in this case) g, the height z, and the mass difference Δm between the patchy particle and the solvent (see Appendix Sec. 3.6.3 for details).

The bottom of the sample is mimicked by a steep Lennard-Jones 12-6 potential $(V_{\rm LJ})$ which is connected to V_g at the transition point $z_{\rm cut}$ with an equal first derivative:

$$V_{\rm LJ}(z_{\rm cut}) = V_q(z_{\rm cut}) \tag{3.11}$$

$$V'_{\rm LJ}(z_{\rm cut}) = V'_q(z_{\rm cut}) \tag{3.12}$$

The complete external potential is thus

$$V_{\text{gravity}}(z) = \begin{cases} V_{\text{LJ}}(z) & z \le z_{\text{cut}} \\ V_g(z) & z > z_{\text{cut}} \end{cases}$$
(3.13)

$$= \begin{cases} 4\epsilon_{\rm LJ} \left(\left(\frac{\sigma}{z} \right)^{12} - \left(\frac{\sigma}{z} \right)^{6} + \frac{1}{4} \right), & z \le z_{\rm cut} \\ -F_g z - b, & z > z_{\rm cut} \end{cases}$$
(3.14)

where $\epsilon_{\rm LJ}$ is a self-chosen value. This potential is smooth up to the first derivative and is suited for molecular dynamics as well as Monte Carlo simulations.

3.2.5 The system's potential energy

The full potential of N spherical colloidal patchy particles interacting via the effective pair potential V_{pair} and experiencing a gravitational field is given by a summation over the pair potentials between all pairs of patchy particles:

$$V = \sum_{i \le j}^{N} V_{\text{pair}}(r_{ij}, \Omega_i, \Omega_j) + \sum_{i}^{N} V_{\text{gravity}}(z_i)$$
(3.15)

and the external field V_{gravity} caused by the gravity and the cell boundary. The latter is only dependent on z, the vertical component of the particle's position.

3.2.6 Constructing the dipatch particle potential

So far the described a model is generally applicable onto patchy particles interacting via critical Casimir interactions and electrostatic repulsions under a gravitational field. However, the model still contains two material-specific parameters: w (wetting parameter) and Υ (surface charge density). Since these are not precisely known, they are treated as free parameters to optimize our

σ [μ m]	$d_p\left[\mu\mathrm{m} ight]$	$ heta_p\left[ightharpoonup^{\circ} ight]$	h_p [nm]	$R_p \left[\mu \mathbf{m} \right]$
3.2(1)	0.58(5)	21(2)	45(5)	1.0(2)

Table 3.1: The particle diameter σ , projected patch diameter d_p , patch arc-angle θ_p , patch height h_p , patch radius of curvature R_p are measured with AFM. The number in brackets indicates the standard deviation of the last digit based on four measurements.

potential model using experimental data. We stress here that these parameters are not meaningless fit parameters but have a physical meaning and their range of possible values is thus limited.

The dipatch particles of interest from Ref [53, 56] are immersed in a water-lutidine (75/25%vol) solution with $c_{\rm MgSO_4}$ =1.0mM. The ions not only screen the surface charge and affect the electrostatic repulsion, but also allows one to tune specific patch-patch interactions [159–161]. The physical dimensions of these dipatch particles are measured with AFM (atomic force microscopy) [53]. The particle's diameter σ , projected patch diameter d_p , patch arc-angle θ_p , patch height h_p , and R_p are listed in Table 3.1 and indicated in Fig. 3.2.

The parameters of the repulsive Yukawa potential (Eq. 3.2 and 3.3) of this solution are κ^{-1} =2.78nm, ϵ =2.25×10⁻¹⁰F/m [147], $\lambda_{\rm B}$ =2.14nm, and σ_c =2 R_p . The surface charge density Υ remains a fitting parameter.

In an off-critical binary liquid, instead of measuring t, the off-set $dT = T_{cx} - T$ from the phase separation temperature T_{cx} is measured. For the construction of the potentials, the location of T_c with respect to T_{cx} is calculated with the relation $\frac{T_{cx}-T_c}{T_c} = \left(\frac{c_c-c}{\mathcal{B}}\right)^{1/\beta}$ where $c_c = 0.287$ denotes the critical (lutidine mass) fraction [81], \mathcal{B} is a non-universal scaling constant of the water lutidine solution without salt measured in Ref. [162], and β is a universal scaling constant (see Table 3.2).

The $V_{\rm C}^{\rm theory}$ is obtained as numerical data from Ref. [72] using the universal and non-universal scaling parameters listed in Table 3.2. For our simulations, it is convenient to have an analytical expression and analytical interpolation of the numerical data. The data is well represented by the functional form:

$$V_{\rm C}(r; dT, w) = -\frac{A}{B} \exp\left(-\left(\frac{r-\sigma}{B}\right)^2\right)$$
 (3.16)

which we fit as a functions of the wetting scaling factor $w \in [0.40, 0.56]$ and $dT \in [0.12, 0.22]$ K which is the temperature range of the experimental measurements. The resulting parameters A(dT, w) and B(dT, w) turn out to be well represented by the product of two simple cubic polynomials of the arguments (see Appendix Sec. 3.6.2).

In order to set the effective patch-patch interaction equal to the isotropic pair potential of two patch particles, the critical Casimir attraction $V_{\rm C}^{\rm theory}$ at distance $D_{\rm edge-edge}$ should become negligible (see Fig. 3.2b). Three potentials are shown in Fig. 3.4 using the above described system, at various values for w with Υ =-0.15e/nm² and dT=0.12K. Even at maximum value w=1.00, when the interaction depth reaches \sim -200 $k_{\rm B}T$, the interaction strength at 0.035 σ ($D_{\rm edge-edge}$ =2 h_p + $D_{\rm min}$) is negligibly small. The potential with w=0.60, which has a more realistic interaction strength, becomes negligibly small at 0.025 σ . Thus, if the bonds are aligned, i.e. θ_i = θ_j =0°, then $V_{\rm pair}=V_{\rm isotropic}$.

If the patches rotate, a repulsive bulk-patch interaction arises due to opposing boundary conditions of the surfaces [149]. As this bulk-patch interaction distance (for $\theta \to \! 0^\circ$ at $D_{\rm edge-edge}$) is longer than the attractive interaction distance 0.025σ , we assume this repulsive contribution to be small compared to the attraction and ignore it in the description of the potential. Nevertheless, to compensate for this assumption, a smaller effective patch width $\theta_p^{\rm eff}$ than the experimental θ_p is allowed. This approach circumvents the explicit calculation and benchmark of the repulsive contribution which would introduce more unknown parameters to the model.

We employ a three-step calculation scheme, as illustrated schematically in Fig. 3.5, for benchmarking the experimental measurements to the model. We start with defining the four input parameters: Υ , w, dT, and $\theta_p^{\rm eff}$. In the second step, from the former three input parameters, the isotropic potentials $V_{\rm Yukawa}$ and $V_{\rm C}$ are constructed, and, in combination with the latter, the part $S'(\theta)$ of the angular switching function S in Eq. 3.8 is determined by numerical integrating. Next, by employing MC simulations, the persistence length L_p and chain length distribution P_x are measured using $V_{\rm pair}$ and $V_{\rm gravity}$. Finally, based on the L_p and P_x over the whole temperature range, the input parameters Υ , w, and $\theta_p^{\rm eff}$ are adjusted, and the steps are repeated.

To perform this adjustment efficiently, we first illustrate the effect of the input parameters on $V_{\rm pair}$ with five example potentials with dT=0.12-0.22K (Fig. 3.6). Later in Section 3.4.1, their qualitative effect on absolute values and temperature trends on L_p and P_x is demonstrated.

Decreasing Υ , i.e. making it more negative, makes the repulsion $V_{\rm Yukawa}$ stronger and, therefore, the pair potential weaker (Fig. 3.6a). Although S' is based on the change of the effective attractive interaction, the repulsion plays a role in the location of the minimum, and thus also Υ has an effect on S' (Fig. 3.6c).

As the scaling function $\hat{\Theta}$ is multiplied by w^3 and the correlation length ξ_t by w, increasing w will make $V_{\rm C}$ effectively deeper and its interaction range longer. The resulting switching function S' becomes more narrow around $\theta \sim 5^\circ$ and less steep around 10° (not explicitly shown in Fig. 3.6).

If both w and Υ are adjusted simultaneously, potentials with similar interaction strength can be created, but with a different temperature dependence (Fig. 3.6b). For example, by comparing potentials (4) and (5), the minima of (4) at dT=0.12 and 0.22K are closer together than (5). This means that there is a weaker temperature effect in (4) compared to (5). Adjusting w and Υ simultaneously can therefore serve as a knob to adjust the effective temperature dependence of $V_{\rm pair}$.

Finally, if $\theta_p^{\rm eff}$ is decreased, e.g. from 21.0° to 18.0°, the curvature of the switching function S' shifts with a constant to smaller angles, while the curvature itself stays the same. Note that the assumption $V_{\rm isotropic}(D_{\rm edge-edge}) \approx 0 k_{\rm B} T$ should still hold upon making $\theta_p^{\rm eff}$ smaller, else a discontinuity in the force around $\theta=0^\circ$ appears.

$\overline{\xi_{t,+}^{(0)}}[nm]$	\mathcal{B}	ν	β	δ
0.198	0.765	0.63	0.3265	4.789

Table 3.2: Critical Casimir non-universal and universal scaling constants. From Ref. [72] [71]

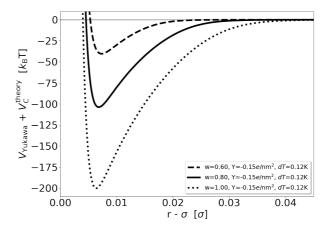


Figure 3.4: Three pair potentials of two isotropic hydrophobic particles with radius R_p immersed in a water-lutidine (75/25%vol) solution with 1.0mM MgSO₄ with Υ =-0.15e/nm², and w=1.00, 0.80, and 0.60 at dT=0.12K. All potentials become negligible at 0.035 σ , thus $V_{\rm pair}(\theta_i = \theta_j = 0^\circ) = V_{\rm isotropic}$.

3.3 Simulation Methods

3.3.1 Monte Carlo simulation of the chain length distribution

For the chain length distribution simulations, a cubic box of length 51.17σ with 1000 particles with periodic boundary conditions, corresponding to an area fraction of $\eta = \rho \pi/4 = 0.30$, where ρ is the number density, is simulated with Monte Carlo (MC). Starting from a random configuration, the system was equilibrated by performing between 1×10^4 up to 6×10^4 MC cycles for the weak and strong interaction strengths, respectively. Each MC cycle consists of 5×10^5 single particle (95%) and cluster moves (5%).

In a single particle move, a randomly selected particle is either rotated (50%) or translated (50%) and can create and break bonds. Note that even though the potentials are deep, breakage occurs. In case of the strongest potential, we observe typically thousands of bond breakage events. The rotation is performed using a random quaternion with an angle uniformly chosen $\in [0, dq_{\rm max}]$. The translation is performed using a random vector \vec{r} with length uniformly chosen $\in [0, \sqrt{3}dr_{\rm max}]$. To enhance the decorrelation and make the sampling in the quasi 2D x,y-plane more efficient, the z-component of the translation vector \vec{r} is reduced by a factor 10 to avoid the particle being placed outside the quasi 2D plane, i.e. inside the wall or far above the gravitational height.

For the cluster move, the translation or rotation move is performed on a chain that is composed of particles that are connected via bonds, i.e. the attractive term in the pair potential is negative, or on single particles. Detailed balance is obeyed by keeping the number of clusters constant. Therefore, any new configuration that creates a new bond is rejected.

The maximum displacement dr_{max} and maximum rotation dq_{max} of the single particle and cluster moves are adjusted to maintain an acceptance ratio between 30-70%.

Measurements are performed on three independent samples during 7×10^4 MC cycles. The chain length distribution is calculated as $P_x = \frac{n_x}{\sum_i n_i}$ with P_x the probability of a chain of length x, n_x the number of chains with length x, and $\sum_i n_i$ the total number of chains.

3.3.2 Measuring the persistence length

The persistence length L_p is calculated via a mode analysis of the chain in the worm-like chain model, in the same manner as done for the experimental measurement [54]. For a chain fluctuating in a two-dimensional plane, the variance of the mode amplitudes is related to the persistence length via:

$$\langle (a_n - \langle a_n \rangle)^2 \rangle = \frac{2}{L_n} \left(\frac{L}{n\pi}\right)^2$$
 (3.17)

where a_n is the mode amplitude of mode number n, L is the contour length of the chain [163, 164].

To determine the mode fluctuations, we use MC runs to sample the conformation of a chain consisting of 15 dipatch particles in three independent samples, while not allowing bonds to break. To enhance decorrelation, in addition to single particle rotation and translation moves, tail flipping moves are performed. In this move, an interparticle bond vector $\vec{r}_{\rm bond}$ of the chain is randomly selected. Then, all particles starting from $\vec{r}_{\rm bond}$ to the tail end of the chain are rotated by 180° around $\vec{r}_{\rm bond}$.

3.4 Results and Discussion

First in section 3.4.1, we qualitatively compare the effects of the benchmark parameters w, Υ , and θ_p^{eff} on the chain length distribution P_x and persistence length L_p and identify three dependencies. In Section 3.4.2, we perform the quantitative benchmark onto experimental measurements.

3.4.1 The P_x and L_p as a function of $\Upsilon, w, \theta_p^{\mathrm{eff}}$ and dT

The three distinct dependencies become apparent in the chain length distributions in Fig. 3.7 and persistence length in Fig. 3.8 for the potential (1)-(5) from Fig. 3.6.

The first effect is that an increased radial potential strength leads to longer and stiffer chains over the complete temperature range. By comparing potentials (1), (2) and (3), we observe increasing chain lengths, i.e. more longer chains, and stiffer chains for (3)<(2)<(1).

The second effect, that of shorter chains and stiffer chains over the complete temperature range, is achieved by reducing the effective patch width θ_p^{eff} . This effect is best observed in potential

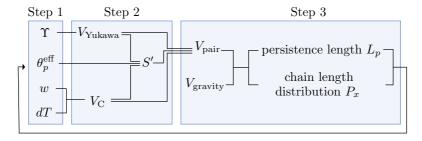


Figure 3.5: The three-step calculation scheme for optimizing the patchy particle potential. The solid lines represent the dependencies, e.g. $V_{\rm Yukawa}$ is only dependent on Υ .

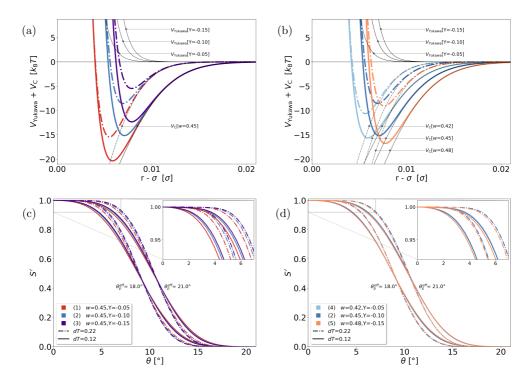


Figure 3.6: Pair potentials of the dipatch particles with diameter σ dressed with hydrophobic patches with radius of curvature R_p , immersed in a water-lutidine (75/25%vol) mixture with 1mM MgSO₄. (a,b) The radial parts, $V_{\rm Yukawa}$ and $V_{\rm C}$. (c,d) The corresponding switching functions S' with $\theta_p^{\rm eff}=18.0$ and 21.0°. The w and $\Upsilon({\rm Y})$ combinations are indicated by the numbers (1) to (5) and the color coding, and the lines indicate $dT=0.12{\rm K}$ (solid) and $dT=0.22{\rm K}$ (dash-dotted).

(2) which shows a strong reduction of chain lengths and a significant increase of the persistence length, but this holds for all potentials.

The third effect relates to the temperature dependence of P_x and L_p . By varying both w and Υ simultaneously, one can create potential with approximately equal strength, but with a different temperature dependence, as done for potentials (2), (4), and (5). By comparing the chain lengths of potentials (4) and (5), at dT=0.17K potential (4) shows the longest chains, while at dT=0.12K it is potential (5) instead. Additionally, in the persistence length the same temperature trend is observed, where at dT=0.22K the chain of potential (5) is more flexible than that of (4), while at dT=0.12K this is reversed. Thus, the temperature strength of the potentials can be tuned while still retaining similar chain lengths and flexibility.

3.4.2 Benchmarking P_x and L_p on experimental measurements

Now that we have examined the qualitative effects on P_x and L_p as a function of w, Υ and θ_p^{eff} , we can benchmark the potential on the experimental measurements quantitatively. Two evaluation functions R1 and R2 are constructed that express the deviation of the simulation of the L_p and P_x from the experiments, respectively.

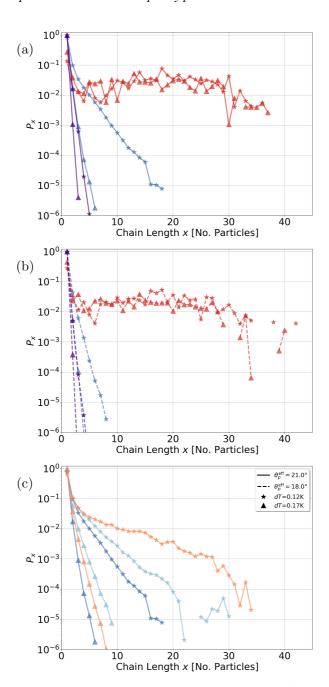


Figure 3.7 : Chain length distributions for potentials (1), (2), and (3) with $\theta_p^{\rm eff}=21.0$ (a) and 18.0° (b) and for potentials (2), (4), and (5) with $\theta_p^{\rm eff}=21.0^{\circ}$ (c). Lines represent $\theta_p^{\rm eff}$ and symbols dT as indicated in the legend, while the color coding is from Fig. 3.6.

For the persistence length measurements, R1 is defined as the percentage of deviation from the experimental values:

$$R1(L_p^{\text{exp.}}, L_p^{\text{sim.}}; dT) = \frac{L_p^{\text{sim.}} - L_p^{\text{exp.}}}{L_p^{\text{exp.}}} \cdot 100\%,$$
 (3.18)

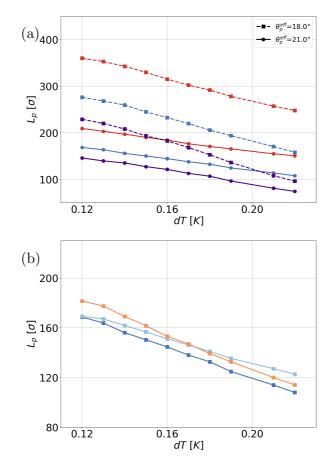


Figure 3.8: Persistence length as a function of temperature of potentials (1)-(5). The effect of Υ and θ_p^{eff} (a) and combining Υ and w simultaneously (b) are shown. Line and symbol coding represents θ_p^{eff} as indicated in the legend, while the color coding is from Fig. 3.6.

and is calculated for each experimentally measured temperature dT=0.12, 0.14, 0.16K. Although not explicitly written, both $L_p^{\rm exp.}$ and $L_p^{\rm sim.}$ are, of course, temperature dependent.

Table 3.3 shows the evaluation of the persistence length of the chains for w=0.456, 0.462, 0.470, Υ =-0.08, -0.09, -0.10e/nm², and $\theta_p^{\rm eff}$ =19.0, 19.5, 20.0° for the three temperatures. For each combination of w and Υ there exists an $\theta_p^{\rm eff}$ in which the persistence length corresponds to experiment within $\pm 8\%$ indicated by the bold numbers.

In both experiments and simulations, we observe an increased monomer and dimer concentration, which does not coincide with the expected exponential decay of the chain length distribution for longer chains (Fig. 3.9). Therefore, the simulated chain length distributions of chains with $x \geq 2$ are evaluated against fitted exponential curves of the (noisy) experimental data

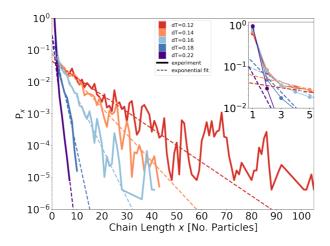


Figure 3.9: The exponential fits onto the experimentally measured chain length distributions for x>2 and $x \le 55$, 30, 25, 10, and 8 for dT = 0.12, 0.14, 0.16, 0.18, and 0.22, respectively. The inset shows a zoom in which the connected dots by solid thin lines represent the experimentally measured probabilities for clarity.

	w		0.456			0.462			0.470	
	$ heta_p^{ ext{eff}}$	19.0	19.5	20.0	19.0	19.5	20.0	19.0	19.5	20.0
Υ	dT^{r}									
	0.12	-5.5	-13.3	-19.6	-1.2	-9.3	-16.5	5.8	-3.0	-11.3
-0.10	0.14	0.2	-7.6	-14.8	4.9	-3.3	-10.8	12.5	2.6	-5.6
	0.16	0.4	-6.9	-14.3	5.6	-3.1	-11.0	11.9	3.5	-5.3
	0.12	-1.8	-10.0	-17.5	2.8	-5.4	-13.4	8.4	0.1	-7.9
-0.09	0.14	3.8	-3.8	-11.7	10.3	0.2	-7.6	17.2	6.3	-1.5
	0.16	4.9	-3.4	-11.1	10.2	1.2	-7.0	17.3	7.9	-1.1
	0.12	2.3	-6.0	-14.0	8.0	-1.6	-9.9	14.6	4.5	-4.3
-0.08	0.14	9.6	0.2	-7.9	14.8	4.9	-3.1	21.9	11.4	2.0
	0.16	10.2	1.4	-6.6	15.3	5. 7	-3.1	23.0	13.2	3.2

Table 3.3: R1 (Eq. 3.18) values which expresses the percentual deviation of the simulation from experiment. The bold numbers indicate the optimal θ_p^{eff} at given w and Υ .

that exclude monomers and dimers. The deviation between the average of the three independent simulations and experiments is evaluated as:

$$R2(P_x^{R2}, P_x^{\text{sim.}}; dT) = \frac{1}{x_{\text{max}}} \sum_{x}^{x_{\text{max}}} \left(\frac{P_x^{\text{sim}} - P_x^{R2}}{P_x^{R2}}\right)^2$$
(3.19)

where $P_x^{\rm R2}$ is the experimental or fitted value. For each dT simulation, the sum runs over the chain lengths x upto $x_{\rm max}$, the maximum chain length for which holds $P_x \geq 5 \times 10^{-5}$ and length $x \leq 45$ particles.

w		0.456			0.462			0.470	
$ heta_p^{ ext{eff}}$	19.0	19.0	19.5	19.0	19.5	19.5	19.5	20.0	20.0
Υ	-0.10	-0.09	-0.08	-0.10	-0.09	-0.08	-0.10	-0.09	-0.08
dT									
0.12	0.60	0.51	0.09	0.52	0.08	2.69	0.24	7.13	9.69
0.14	0.61	0.57	1.60	0.54	1.21	39.52	9.25	143.09	804.29
0.16	0.63	0.57	0.12	0.57	0.23	$\sim 10^{6}$	0.14	$\sim 10^7$	$\sim 10^{9}$
0.18	0.54	0.54	0.43	0.55	0.45	50.59	0.33	$\sim 10^{3}$	$\sim 10^{20}$
0.22	0.48	0.45	0.55	0.45	0.57	0.40	0.56	0.32	0.07

Table 3.4: R2 (Eq. 3.19) value which expresses the deviation of simulation from experiment in order of magnitude. The bold values are from the selected potential.

Calculating chain length distributions requires more CPU time, because there are more particles in the simulation box. Therefore, the chain length distribution simulations were only performed for the potentials with a good persistence length as listed in bold in Table 3.3.

Based on the smallest deviation from experiment over the whole temperature range as defined by R1 and R2 (indicated in bold in Table 3.4), the potential with w=0.462, Υ =-0.090 e/nm², and $\theta_p^{\rm eff}$ =19.5° is selected (Fig. 3.10). This optimized potential performs best in mimicking the experimentally measured temperature dependent chain length distribution and persistence length as shown in Fig 3.11.

Although the simulations still show small deviations from experiment, the potential cannot be significantly improved. For a truly perfect overlap, the potential should exhibit a weaker temperature dependence in P_x as the chains are too short at dT=0.22K and mimic experiment well at dT=0.12K, while it requires a stronger temperature dependence in L_p , as R1 shifts from positive (dT=0.22K) to negative (dT=0.12K). This is a contradicting property of the potential. Thus, changing the input parameters cannot lead to an improved potential, using the current potential forms.

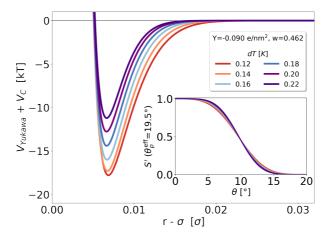


Figure 3.10 : The radial part of the pair potentials V_{Yukawa} and V_{C} and the switching function S' (in the inset) are shown for temperatures dT=0.12-0.22K with w=0.462, Υ =-0.09e/nm², and θ_p^{eff} =19.5°.

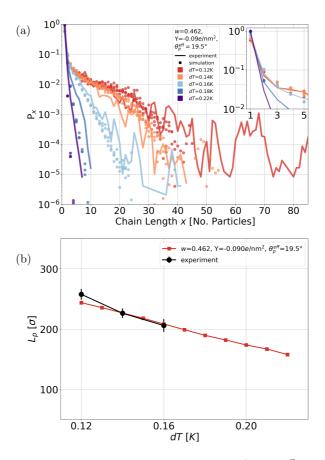


Figure 3.11: With potential parameters w=0.462, Υ =-0.090e/nm², and $\theta_p^{\rm eff}$ = 19.5° the chain length distribution P_x (a) and persistence length L_p (b) are simulated and mimic experiment over the temperature range of $dT \in [0.12, 0.22]$ K. The vertical error bars in (b) represent the standard deviation of measurements consisting of 3600 images (30 minutes at a frame rate of 2fps).

We stress however, that notwithstanding these small difference the potential model is remarkably accurate, and can predict the assembly as well as the mechanical behavior over the relevant temperature range. Moreover, the final values for the free parameters in the optimized model, are physically reasonable. The patch angle $\theta_p^{\rm eff}$ is very close to the measured patch width by AFM. The surface charge density is within the expected physical range for these types of colloids, see e.g. Ref [72]. Finally the optimal w value is lower than expected, but still reasonable. Thus, we conclude the potential model is physically sound, and can be used for complex colloids systems.

3.5 Conclusion

In this work we have developed an accurate potential model to simulate patchy particles interacting via critical Casimir forces. The potential model is based an a hybrid bottom-up/top-down coarse-graining approach, in which we take isotropic interaction from accurate scaling theory, and adjust these to the patchy particle geometry, by numerical integration and fitting as a func-

tion of the patch orientation. While accurate, the theoretical scaling theory contains several poorly known material parameters: the wetting factor, the charge density, and the effective patch width. We optimized the potential by fine-tuning these parameters, so that a system of these particles under gravitational field, mimics the experimentally observed chain length distribution and persistence length as best as possible. Indeed, we demonstrated that the optimal potential model accurately predicts the experimental results.

While the optimization procedure might be seen as a fitting procedure, all parameters have a physical meaning and can be interpreted, and can only be used for fine-tuning. As there is basically no freely adjustable parameter, it is quite remarkable that we can simulate such a complex system accurately.

Thus, our work clearly shows how a single potential model can be developed to accurately simulate a complex system of patchy particles interacting with critical Casimir interactions, under a variety of conditions. Our approach provides a general framework to develop coarse-grained effective potentials that can be used to reproduce and interpret experiments, and guide future experiment. For instance, a direct extension of the model is to describe multivalent patchy particles, e.g., tetra-patch particles, so that networks can be formed. Moreover, using the optimized potential model in a (Brownian) molecular dynamics setting can provide dynamical information.

We stress that our coarse-grained potential is naturally bound to a specific experimental system. Changing the system, will also change the potential. Therefore, the potential needs to be optimized for each new colloidal systems. While this seems a drawback, we stress that much or our framework can be automatized. In fact, most of the effort will lie in the particle synthesis and collection of experimental data to benchmark the models.

Finally, we mention that our approach still relies on functional forms for the potentials, and on standard fitting procedures. In the future, the use of machine learning can be considered to directly go from the theoretical isotropic potentials to the final model, without going through the intermediate fitting steps.

3.6 APPENDIX

3.6.1 THE ISOTROPIC CRITICAL CASIMIR ATTRACTION

For the construction of the patchy particle potential we start with the theoretical prediction for the isotropic critical Casimir interaction between two spheres with radius R_p as described in Ref. [72, 83]. Here, for completeness, we outline the basics of this isotropic interaction. First, the scaling parameters are explained. Then, the mapping from d=4 to 3 dimensions of the critical Casimir interaction between parallel plates is introduced, followed by the integration over two spheres in the Derjaguin approximation. For a more exhaustive overview on critical Casimir interactions, see Ref. [150], and on the construction of the isotropic potentials see Ref. [72].

The critical Casimir force follows universal scaling functions determined solely by the universality classes of the solvent and of the colloid surfaces that are in contact with the binary liquid near its demixing transition.

An important determining factor in the critical Casimir force is the solvent correlation length ξ . This parameter ξ is a function of its *distance* from the critical point at (T_c, c_c) , i.e. temperature

and concentration. Specifically, it scales with the scaled temperature $t=(T_{\rm c}-T)/T_{\rm c}$ via $\xi_t=\xi_{t,\pm}^{(0)}|t|^{-\nu}$ with $t\to 0$ at the critical concentration and thus corresponds to the Ising model in the absence of an external magnetic field \vec{B} . The bulk ordering field h_b is proportional to the *distance* of the chemical potential μ of the off-critical mixture with respect to the critical chemical potential $\mu_{\rm c}$ at $c_{\rm c}$. The correlation length ξ scales as $\xi_h=\xi_h^{(0)}|h_b|^{-\nu/\beta\delta}$ with $h_b\to 0$ at t=0. The $\nu=0.63$, $\beta=0.3265$, and $\delta=4.789$ are universal scaling exponents [71].

The critical Casimir force is a function of the scaled distances \mathcal{Y} and $\Lambda = \operatorname{sgn}(h_b) \frac{D}{\xi_h}$ between the confining objects. During an experimental measurement, only t is easily varied while h_b stays constant. Therefore, the scaling parameters are rewritten in:

$$\mathcal{Y} = \operatorname{sgn}(t) \frac{D}{\xi_t}$$
 $\Sigma = \frac{\Lambda}{\mathcal{Y}}$ (3.20)

The critical Casimir interaction in 3 dimensions for two parallel plates is denoted $\vartheta_{||}^{(d=3)}(\mathcal{Y}, \Sigma)$. This function is not directly known, but is determined via mapping 3D MC Ising model simulations at $\Sigma=0$, i.e. $h_b\to 0$, and $\vartheta^{(d=4)}(\mathcal{Y},\Sigma)$ from mean-field theory within the Landau-Ginzburg theory [165].

$$\vartheta_{||}^{(d=3)}(\mathcal{Y}, \Sigma) = \frac{\vartheta_{||}^{(d=4)}(\mathcal{Y}, \Sigma)}{\vartheta_{||}^{(d=4)}(\mathcal{Y}, \Sigma = 0)} \vartheta_{||}^{(d=3)}(\mathcal{Y}, \Sigma = 0)$$
(3.21)

The material-dependent surface-solvent interactions, are dependent on the surface fields h_s [158]. Including the effect of h_s via $w(h_s)$ explicitly in d=4 gives $\vartheta_{||}^{(d=4)}(\mathcal{Y},\Sigma;h_s)=w^d\vartheta_{||}^{(d=4)}(\mathcal{Y}/w,\Sigma)$. It is assumed that this also hold for d=3, although this has not been explicitly tested.

Using the force $F_{C,||}(L) = SL^{-3}\vartheta_{||}^{(d=3)}(L/\xi_t,\Sigma)$ between two plates of surface area S separated a distance L, integration over the two patch particle spheres with radius R_p and R_p' in the Derjaguin approximation is performed to yield the force between two spheres at a distance D, the shortest surface-surface distance between the particles,

$$F_{\mathcal{C}}(D) = \int_0^{\phi_M} d\phi \frac{dS(\phi)}{L(\phi)^3} \vartheta_{||}^{(d=3)}(L(\phi)/\xi_t, \Sigma)$$
(3.22)

where the integral is over the angle ϕ , and $dS(\phi)$ is the surface of an infinitesimal ring of radius $R\sin\phi$, and $L(\phi)$ is the distance between two such rings on the two spheres.

The isotropic $V_{\rm C}^{
m theory}$ then follows by integrating over the force. Realizing that only small ϕ contribute, change of variables, rearrangement, and execution of (one of) the integrals gives [84, 147, 155, 166]

$$V_{\mathcal{C}}^{\text{theory}}(D, R_p, R'_p, \mathcal{Y}, \Sigma) = \int_{D}^{\infty} dz F_{\mathcal{C}}(z)$$

$$= \frac{1}{D} \frac{2\pi R_p R'_p}{(R_p + R'_p)} \int_{1}^{\infty} dx (x^{-2} - x^{-3}) \vartheta_{||}^{(d=3)}(x \mathcal{Y}, \Sigma)$$

$$\equiv \frac{1}{D} \frac{2R_p R'_p}{(R_p + R'_p)} \hat{\Theta}^{(d=3, \text{Derj})}(\mathcal{Y}, \Sigma)$$
(3.23)

where in the last line we defined the function $\hat{\Theta}^{(d=3,\mathrm{Derj})}(\mathcal{Y},\Sigma) \equiv \pi \int_{1_{-}}^{\infty} dx (x^{-2} - x^{-3}) \vartheta_{||}^{(d=3)}(x\mathcal{Y},\Sigma)$. Note that in the Derjaguin approximation, the (critical Casimir) interaction strength is easily scaled according to the radii of the particles.

 $\text{As } \vartheta_{||}^{(d)}(\mathcal{Y},\Lambda)=\vartheta_{||}^{(d)}(\mathcal{Y},\Sigma) \text{ [83], we can replace } \hat{\Theta}^{(d=3,\mathrm{Derj})}(\mathcal{Y},\Sigma) \text{ with } \hat{\Theta}^{(d=3,\mathrm{Derj})}(\mathcal{Y},\Lambda).$ For two spheres with equal radius, including the effect of the surface fields $w(h_s)$, we then finally arrive at

$$V_{\rm C}^{\rm theory}(r) = \frac{R_p w^3}{D} \hat{\Theta}^{(d=3, {\rm Derj})}(\mathcal{Y}/w, \Lambda)$$
 (3.24)

where $r=D+2R_{p}$ is the center-to-center distance, and we suppressed the functional dependence of $R_p, \mathcal{Y}, \Lambda$ and h_s . This is Eq. 3.4 arising in the Main Text.

3.6.2 POTENTIAL OPTIMIZATION

In this section, we detail how we construct the fit the potential. First, $V_{\rm C}$ is fitted as function of A and B to the numerical data, and A and B are again fitted to w and dT. Second, the construction of $V_{\text{gravity}}(z_i)$ is discussed. Third, the integration of the switching function S is explained.

Fit parameters for $V_{\rm C}$

The critical Casimir attraction $V_{\rm C}^{\rm theory}$ is fitted to Eq. 3.16 for $D \in [0.004, 0.025]\sigma$ with the curve_fit function of the scipy package in Python which is a non-linear least-square fitting procedure. The fitting is performed for $w \in [0.40, 0.56]$, surface charge density $\Upsilon \in$ [-0.05, -0.38] e/nm² and $dT \in [0.12, 0.22]$ K. The values for A and B are again fitted to the functions:

$$A(w, dT) = \left(\sum_{x=0}^{3} a_x w^x\right) \left(\sum_{y=0}^{4} b_y dT^y\right)$$
 (3.25)

$$B(w, dT) = \left(\sum_{x=0}^{3} a_x w^x\right) \left(\sum_{y=0}^{4} b_y dT^y\right)$$
 (3.26)

	$A \left[\sigma k_{\mathrm{B}} T \right]$	$B\left[\sigma\right]$
$\overline{a_0}$	-0.0150618	0.2193184
a_1	2.1799711	-6.4152869
a_2	-9.9192600	0.6840590
a_3	51.4795047	0.6859149
b_0	-0.2261732	-0.0072189
b_1	7.2460609	0.0712114
b_2	-60.6003083	-0.5016291
b_3	221.6023391	1.8701371
b_4	-304.8329480	-2.7834135

Table 3.5: The coefficients a and b valid for $w \in [0.40, 0.56]$, surface charge density $\Upsilon \in [-0.05, -0.38] \ e/\text{nm}^2$, and $dT \in [012, 0.22] \text{K}$ for the calculation of A and B as defined in Eq. 3.25 and 3.26, respectively.

Table 3.5 shows the resulting coefficients a and b.

3.6.3 Gravity

As experimentalists on Earth see their patchy particles at the bottom of the sample due to the gravitational force pulling the colloids down, we add gravity to the model. The gravitational energy is defined as:

$$V_a(z) = mgz = -F_a z \tag{3.27}$$

where m is the mass, g the gravitational acceleration (on earth in this case), z the height, and F_g the gravitational force. In order to know the effective gravitational force acting on the colloids, we need the mass difference between the colloid and the solvent:

$$\Delta m = \frac{4}{3}\pi r_{\text{colloid}}^3(\phi_{\text{TPM}}\rho_{\text{TPM}} + \phi_{\text{PS}}\rho_{\text{PS}} - \rho_{\text{sol}})$$
(3.28)

where $r_{\rm colloid}$ is the radius of the colloid, ϕ_x the fractional volume, and ρ_x the density of material x and the water-lutidine solution.

For the synthesis of dipatch particles [63], three spheres of polystyrene (PS) surrounding one sphere of 3-(trimethoxysilyl)propyl methacrylate (TPM). The fractional volumes are estimated by assuming that the sphere are touching such that ratio of the radii is $r_{\rm TPM}$: $r_{\rm PS}$ =-1+2/ $\sqrt{3}$. We calculate a volume fraction $\phi_{\rm TPM}=0.0012$

While the patch material is clearly distributed anisotropically, we do not expect a gravitational torque acting on the patchy particles. Only a very small fraction TPM is used in the synthesis, which means that the patchy particle does not deviate much from an isotropic sphere.

For a dipatch particle with radius $r=0.5\sigma$, the following values are used:

 $\begin{array}{ll} \phi_{\rm TPM} = 0.0012 \\ \phi_{\rm PS} &= 1\text{-}\phi_{\rm TPM} \\ \rho_{\rm TPM} = 1.235~{\rm g/mL}~{\rm [167]} \\ \rho_{\rm PS} &= 1.05~{\rm g/mL}~{\rm [168]} \\ \rho_{\rm sol} &= 0.98966~{\rm g/mL}~{\rm [169]} \\ q &= 9.80665~{\rm m/s}^2 \end{array}$

Which results in an F_g =-7.7 $k_{\rm B}T/\sigma$ for the dipatch particles corresponding to a gravitational height of 0.13 σ . Solving the equations in Eq. 3.14 with $\epsilon_{\rm LJ}$ =500 $k_{\rm B}T$ gives values for b=8.64 $k_{\rm B}T$ and $z_{\rm cut}$ =1.12 σ .

3.6.4 Calculation of the switching function

We calculate the switching function from a direct evaluation of the patch-patch Casimir attraction V_{pp} , by performing a (numerical) integration over the two surfaces of the patches in various configurations in which the particles are placed at the minimum energy position r_{\min} , with specific patch angles $\theta_i, \theta_j, \theta'_{ij}$

$$V_{pp}(r_{\min}, \theta_i, \theta_j, \theta'_{ij}) = \int_{D=0}^{D=\infty} V_{\text{area}}(D) dA$$
 (3.29)

where D=r-2R is the surface-surface distance, $V_{\rm area}$ is the local Casimir potential energy per area, and dA is a small subarea on the patch surface [84]. We can approximate this effective interaction by performing a summation over N_A small subareas dA on both patch surfaces

$$V_{pp}(r_{\min}, \theta_i, \theta_j, \theta'_{ij}) \approx \sum_{i=1}^{N_A} V_{\text{area}}(D)$$

$$\approx \alpha \frac{1}{2} \sum_{x=i,j}^{N_A^x} V_{\text{C}}(D_{\min}^x)$$
(3.30)

where we compute $V_{\rm area}(D)$ from the critical Casimir interaction $V_{\rm C}(r)$ for each of these N_A subareas on particle x=i,j using the closest distance $D_{\rm min}^x$ to the patch surface on the other particle, as schematically illustrated in Fig. 3.12. As $V_{\rm area}$ has units of energy per area, whereas $V_{\rm C}$ is in units of energy, we insert an arbitrary prefactor α to make this conversion. We do not calculate this correction factor α explicitly. Instead, for the calculation of the integrated switching function $S^{\rm int}$ in Eq. 3.31, we normalize the integration to the conformation where the patches are perfectly aligned, i.e. $\theta_i = \theta_j = \theta'_{ij} = 0^\circ$.

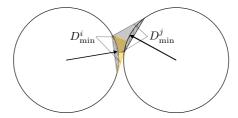


Figure 3.12: The patch-patch interaction is calculated by integrating over both patch surfaces. The yellow and dark-colored areas for the particle on the left and right schematically indicate the volumes in which the N_A distances D_{\min}^x lie, respectively.

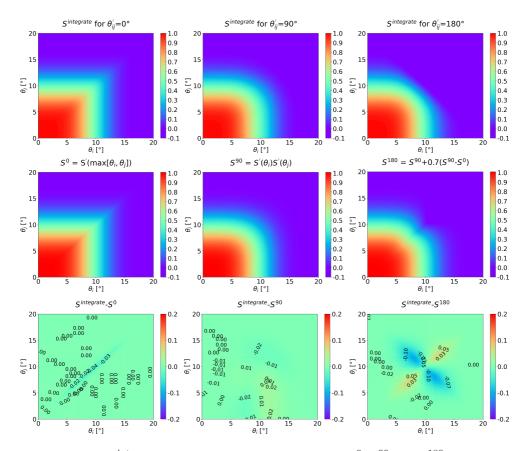


Figure 3.13 : The $S^{\rm int}$ (top row), the estimated switch functions S^0 , S^{90} , and S^{180} (middle row) (Eq. 3.33, 3.34, and 3.35, resp.), and the difference between $S^{\rm int}$ and S^0 , S^{90} , and S^{180} (bottom row) for θ'_{ij} =0, 90, and 180° using an isotropic potential with w=0.462, Υ =-0.090 e/nm², $\theta^{\rm eff}_p$ =19.5°, and dT=0.16K.

$$S^{\text{int}}(\theta_{i}, \theta_{j}, \theta'_{ij}) = \frac{V_{pp}(r_{\min}, \theta_{i}, \theta_{j}, \theta'_{ij})}{V_{pp}(r_{\min}, \theta_{i} = \theta_{j} = \theta'_{ij} = 0^{\circ})}$$

$$= \frac{\sum_{x=i,j}^{N_{A}^{x}} V_{C}(D_{\min}^{x}; \theta_{i}, \theta_{j}, \theta'_{ij})}{\sum_{x=i,j}^{N_{A}^{x}} V_{C}(D_{\min}^{x}; \theta_{i} = \theta_{j} = \theta'_{ij} = 0^{\circ})}$$
(3.31)

The $N_{\rm A}$ small equal areas of the summation are generated using an icosphere. An icosphere is a spherical shape composed of equally sized triangles, and, by definition, the triangles' corners are uniformly distributed along the surface of the sphere. Thus, summing over these triangles' corners mimics the summation over $N_{\rm A}$. Also, to simplify the integration, we assume the curvature of the patch is equal to the curvature of the colloidal bulk particle.

The top row of Fig. 3.13 shows $S^{\rm int}$ of Eq. 3.31 for the potential with w=0.462, Υ =-0.090e/nm², and θ_p =19.5° at dT=0.16K. For this integration, we used $N_A \sim$ 4730 for each particle. The

Tp	0.12	0.14	0.16	0.18	0.20	0.22
C_2	-9.9041399e-04	.9.9041399e-04 -8.6203362e-04 -6.9326098e-04 -4.5588257e-04 -1.6719905e-04 1.1841309e-04	-6.9326098e-04	-4.5588257e-04	-1.6719905e-04	1.1841309e-04
C_3	4.8281954e-04	4.8281954e-04 5.5081595e-04 4.6183135e-04 2.3084587e-04 -8.3489930e-05	4.6183135e-04	2.3084587e-04	-8.3489930e-05	-3.9826809e-04
C_4	-2.6855756e-04	-2.3657358e-04	-1.4824624e-04	-1.6649632e-05 1.3192856e-04 2.6630861e-04	1.3192856e-04	2.6630861e-04
C_5	2.7014513e-05	1.6508372e-05	-2.4504174e-06	-2.7092006e-05	-5.2730314e-05	-7.4311871e-05
c_{6}	-1.7667696e-06	-7.4603246e-07	9.2495528e-07	2.9849240e-06	5.0223231e-06	6.6203569e-06
C_7	7.0531602e-08	2.6147859e-08	-4.3910243e-08	-1.2787947e-07	-2.0773103e-07	-2.6586465e-07
c_8	-1.3515934e-09	-6.2723052e-10	5.0997548e-10	1.8552989e-09	3.0949410e-09	3.9270196e-09

Table 3.6: The coefficients c of S' in Eq. 3.32 for which θ has units of degrees and w=0.462, Υ =-0.090e/nm², θ_p^{eff} =19.5° and $dT \in [012, 0.22]$ K.

three plots show how the interaction energy changes upon rotating the colloidal particles with angles θ_i and θ_j while θ'_{ij} =0, 90, or 180°.

Next, we would like to construct an approximation of S^{int} based on knowing only the switch function at $S^{\text{int}}(\theta_i, \theta_i = 0^\circ)$. This part of the switching function S is fitted with the function

$$S'(\theta) = \exp\left(\sum_{l=2}^{8} c_l \theta^l\right) \tag{3.32}$$

by using the curve_fit function of SciPy. The sum runs from 2, to ensure that the first derivative of S' is zero at θ =0°. It runs upto 8, as the fitting procedure was not able to include more terms to improve the fit. In Table 3.6, the coefficients for the switching function of the benchmarked potential with w=0.462, Υ =-0-090 e/nm², θ_p^{eff} =19.5° and $dT \in [012, 0.22]$ K are shown.

From S' we construct the functions S^0 , S^{90} , and S^{180} defined, respectively, as

$$S^{0}(\theta_{i}, \theta_{j}) = S'(\max(\theta_{i}, \theta_{j})) \tag{3.33}$$

$$S^{90}(\theta_i, \theta_j) = S'(\theta_i)S'(\theta_j) \tag{3.34}$$

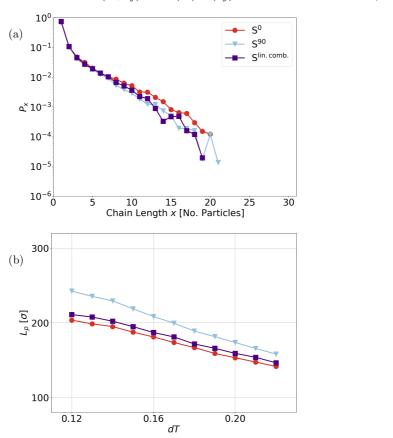


Figure 3.14 : The chain length distribution P_x (a) and persistence length L_p (b) of using function S as S^0 , S^{90} , or $S^{\text{lin. comb.}}$ with w=0.462, Υ =-0.090 e/nm 2 , θ_p^{eff} =19.5°, and dT=0.16K.

$$S^{180}(\theta_i, \theta_j) = S^{90}(\theta_i, \theta_j) + 0.7(S^{90}(\theta_i, \theta_j) - S^{0}(\theta_i, \theta_j)). \tag{3.35}$$

Fig. 3.13 shows these functions in the middle row and their difference with $S^{\rm int}$ in the bottom row. The functions were made by carefully inspecting the shape of the numerical results for $S^{\rm int}$ at 0, 90, and 180°. $S^{\rm int}$ at 0° and 90° are well approximated by S^0 and S^{90} , as one can see in the bottom row of Fig. 3.13. Inspecting $S^{\rm int}$ at 180° and $\max(\theta_i,\theta_j)<5$ °, one observes that it is almost identical to S^{90} . Only at $5<\theta_i,\theta_j<15$ °, the value of $S^{\rm int}$ for 180° is lower than for 90°. In exactly this region, also S^0 and S^{90} show a difference. Therefore, S^{180} is constructed by adding to S^{90} the difference between S^0 and S^{90} .

To compose a functional solution for S as a function of θ_i , θ_j and θ'_{ij} as a linear combination of S^0 , S^{90} , and S^{180}

$$S^{\text{lin. comb.}} = \begin{cases} S^{0}(\lambda - 1) + S^{90}\lambda, & \lambda = \theta'_{ij}/90^{\circ} \le 1\\ S^{90}(2 - \lambda) + S^{180}(\lambda - 1), & \lambda > 1 \end{cases}$$
(3.36)

where $\lambda=\theta'_{ij}/90^\circ$. The discrepancy between $|S^{\rm int}-S^{\rm lin.\,comb.}|\leq 10\%$ and lies mainly in a region where $S^{\rm int}$ is approximately 0.5, which means it is not a highly occupied region. The coefficient 0.7 in S^{180} was chosen to minimize the discrepancy between $S^{\rm lin.\,comb.}$ and $S^{\rm int}$ for $90<\theta'_{ij}<180^\circ$.

We simulate the chain length distribution and persistence length to test the sensitivity of the choice of switch function S. Figure 3.14 shows the persistence length of a 15-particle long chain and the chain length distribution of 1000 dipatch particles with gravity at the three test cases in which the switching function S is: S^0 , S^{90} , or $S^{\text{lin. comb.}}$. The persistence length of S^0 and $S^{\text{lin. comb.}}$ are similar, which seems to indicate that the chains under gravity have θ'_{ij} around 0°. However, the switching function S^{90} shows a stronger temperature dependence on the persistence length.

While the choice of switching function is substantially influencing the persistence length, it turns to have only a minor effect on the chain length distribution, as seen in Fig. 3.14. Advantages of S^{90} are its simple form and its dependence on the orientation of both particles. As the S^0 leads to discontinuous torques due to the max function, another advantage of S^{90} is its continuous torques in a molecular dynamics simulation. Therefore, the switching function S used in equation 3.8 has the form of S^{90} .

3.6.5 PARAMETER LIST

For completeness, we compose a list with all the parameters and functions including their symbol, a description, their value, units and reference used in the model in Table 3.7-3.9. The given values are for the benchmarked dipatch particle potential.

Table 3.7: The parameters of the potentials, gravitational parameters and solvent properties.

72	nm	0 198	the solvent correlation length of the binary liquid related to t	÷(0)
	K	T_c +0.08	phase separation temperature	T_{cx}
[81, 170]	റ്	33.68	critical temperature of the binary lutidine/water mixture	T_c
	$_{ m mM}$	0.375	salt concentration, MgSO ₄	$c_{ m salt}$
[162]	c_c^{-1}	0.765	non-universal scaling constant of the water lutidine solution without salt	\mathcal{B}
[81]		0.287	critical luditine mass fraction of the water and lutidine binary mixture	$c_{ m c}$
	vol% lutidine	25	composition of the binary liquid	c
	nm	2.14	Bjerrum length	$\lambda_{ m B}$
	nm	2.78	solvent properties Debye length of the lutidine/water (25/75vol%) mixture with ImM MgSO ₄	κ^{-1}
	σ	0.13	gravitational height	$z_{\mathrm height}$
	pg	1.04	the mass difference between the solvent and the particle	Δm
	$k_{ m B}T$	500	a self-chosen value; it represents the steep potential of the capillary wall	$\epsilon_{ m LJ}$
			gravitational parameters	
	K		$T_{cx}-T$	dT
	$k_{ m B}T$		the external field caused by the gravity and cell boundary	$V_{ m gravity}$
			the switching function of the effective patch-patch interaction of \mathbf{p}_{ik} and \mathbf{p}_{jl}	$S_{\mathbf{p}_{ik},\mathbf{p}_{jl}}$
			the fitted switching function	Š
	$k_{ m B}T$		patch-patch potential	$V_{\mathbf{p}_{ik},\mathbf{p}_{jl}}$
	$k_{ m B}T$		patchy particle pair potential	$V_{ m pair}$
	$k_{ m B}T$		analytical interpolation of $V_{ m C}^{ m theory}$	$V_{\rm C}$
[72]	$k_{ m B}T$		theoretical critical Casimir interaction (acquired as numerical data)	$V_{\rm C}^{ m theory}$
	$k_{ m B}T$		isotropic repulsive electrostatic Yukawa potential	$V_{ m Yukawa}$
[72]	$k_{ m B}T$		isotropic potential of a spherical colloidal particle (Eq. 3.1)	$V_{ m isotropic}$
			potentials	
	$1/k_{ m B}{ m T}$		inverse temperature	β
	K		temperature	T
Ket.	unit	value	description	symbol

symbol	description	value	mill	TYCI.
	scaling functions and parameters			
Œ	a universal scaling function			
t	scaled temperature $(T_c - T)/T_c$			
h_b	bulk ordering field			
η	chemical potential			
¥	solvent correlation length			
2	scaling function related to the scaled temperature t			
V	scaling function related to the bulk ordering field h_b			
7	universal scaling exponent	0.63		7
β	universal scaling exponent used in the relation $\frac{T_{cx}-T_c}{T}=\left(\frac{c_c-c}{R}\right)^{1/\beta}$	0.3265		7
δ	universal scaling exponent	4.798		<u>Z</u>
h_s	surface field, describes the surface preference of the binary liquid			
m	scaling wetting parameter, a function of surface field h_s	0.462		[82, 158]
	properties and physical dimensions of the dipatch particle			
Z	charge of the particle		в	
T	surface charge density	-0.090	e/nm^2	
d_p	projected patch diameter (AFM)	0.58(5)	$\mu_{ m m}$	[53, 56]
θ_p	patch diameter (AFM)	21(2)	0	[53, 56]
R_p	patch particle radius of curvature (AFM)	1.0(2)	$\mu_{ m m}$	[53, 56]
ρ	diameter of bulk particle (AFM)	3.2(1)	$\mu_{ m m}$	[53, 56]
h_p	height of the patch (AFM)	0.58(5)	$\mu_{ m m}$	[53, 56]
σ_c	diameter of particle used in Yukawa potential, equals $2R_p$	2.0	$\mu_{ m m}$	
n_p	number of patches of the patchy particle	2		
ρ eff	$A_{1} = B_{2} = A_{1} = A_{2} = A_{3} = A_{4} = A_{4$		c	

Table 3.8: The parameters of the scaling functions, and properties and physical dimensions of the dipatch particle.

 $D_{
m edge-edge}$ D_{\min} $egin{aligned} \mathbf{p}_{ik} \ heta_i, heta_j \ heta'_{ij} \ \Omega_i \end{aligned}$ observables angle between patch vector and interparticle vector $k^{\mathrm{t}h}$ patch vector of particle idistance from the edge of the patch, to the edge of the other patch, when $heta_i, heta_j = 0^\circ, 2h_p + D_{\min}$ contour length of the chain (Eq. 3.17) the amplitude of the n^{th} bending mode in the worm-like-chain model (Eq. 3.17) probability of finding a chain of length \boldsymbol{x} patch vectors' projected angle on the plane perpendicular to the interparticle vector surface-surface distance at which $V_{\text{isotropic}}(D_{\min}) = \min(V_{\text{isotropic}})$ surface-surface distance between two spherical particles, $r-\sigma$ center-to-center distance between two particles, $|\mathbf{r}_{ij}|$ the interparticle vector from particle i to jpersistence length (4D) quaternion representation of the orientation of particle ipositional and orientational variables of the dipatch particle description 0.0068 0.035value 9 9 9 9 ρ [163, 164][163, 164]Ref.

Table 3.9: The parameters of the positional and orientational variables of the dipatch particle, and observables.

4

EXTENDED WERTHEIM THEORY PREDICTS THE ANOMALOUS CHAIN LENGTH DISTRIBUTIONS OF DIVALENT PATCHY PARTICLES UNDER EXTREME CONFINEMENT

Colloidal patchy particles with divalent attractive interaction can self-assemble into linear polymer chains. Their equilibrium properties in 2D and 3D are well described by Wertheim's thermodynamic perturbation theory which predicts a well-defined exponentially decaying equilibrium chain length distribution. In experimental realizations, due to gravity, particles sediment to the bottom of the suspension forming a monolayer of particles with a gravitational height smaller than the particle diameter. In accordance with experiments, an anomalously high monomer concentration is observed in simulations which is not well understood. To account for this observation, we interpret the polymerization as taking place in a highly confined quasi-2D plane and extend the Wertheim thermodynamic perturbation theory by defining addition reactions constants as functions of the chain length. We derive the theory, test it on simple square well potentials, and apply it to the experimental case of synthetic colloidal patchy particles immersed in a binary liquid mixture that are described by an accurate effective critical Casimir patchy particle potential. The important interaction parameters entering the theory are explicitly computed using the integral method in combination with Monte Carlo sampling. Without any adjustable parameter, the predictions of the chain length distribution are in excellent agreement with explicit simulations of self-assembling particles. We discuss generality of the approach, and its application range.

4.1 Introduction

Synthetic colloidal particles suspended in a near-critical binary liquid mixture (e.g. water and lutidine), attract each other via a solvent mediated critical Casimir force. Through novel synthesis routes these particles can be designed such that they form directed bonds between patches on the surface of neighboring particles [63]. As such patchy particles simultaneously experience thermal motion, their statistical behavior follows the Boltzmann distribution. Hence, they can be viewed as mesoscopic analogs of (carbon) atoms, which can be directly observed via, e.g., confocal microscopy [57]. In this way, patchy particles can act as an experimental model system to explore complex self-assembled structures analogous to molecular architectures, such as chains, rings, and networks [38, 53, 54, 57, 138].

To understand the self-assembly in patchy particle systems, one can of course resort to computer simulations [43, 47, 145, 146, 171], but an attractive alternative is to invoke statistical mechanics which aids to a better theoretical understanding and prediction. One of the classical theories for self-assembly of colloidal particles is the Wertheim thermodynamic perturbation theory (TPT) [112–115], later reformulated as Statistical Associating Fluid Theory (SAFT) by Chapman et al. [116]. Wertheim's theory was originally intended as a molecular model [172], but also works for mesoscopic particles. For divalent patchy particles in two and three dimensions, Wertheim theory is able to predict the polymerization equilibrium in terms of for example the chain length distribution, with the particle density and a pair bonding strength as the only input parameters [140, 142, 143, 173–175]. For systems with average valencies larger than two, equilibrium properties are predicted using Flory-Stockmayer's polymer theory [40, 176]. The location of the percolation point, existence of empty liquids and equilibrium gels were predicted theoretically, confirmed in simulation and validated experimentally [141, 177–181].

However, when there is a mismatch in mass density of the particles and the suspending solvent, particles will sediment to the bottom of the sample due to gravity. For sufficiently low particle concentration (or volume fraction) and short gravitational height, the system is then confined to a quasi-2D plane; making single layer structures possible. Direct application of Wertheim's theory for divalent particles in 2D or 3D will give an exponential distribution and a large discrepancy between the experiments and theoretical prediction exists, in particular in the monomer (and dimer) density [53, 182]. In this work we address this discrepancy.

The origin of the discrepancy is that, under extreme confinement where spherical particles live in a two-dimensional (x,y)—plane, the monomers are still able to rotate around their center-of-mass (Fig. 4.1a). While some monomer orientations, e.g. when their patch points toward the wall, are part of the orientational phase space, their patches are not available for bonding. This renders the system fundamentally different compared to the standard 2D and 3D systems. As a consequence, in order to predict thermodynamic properties, this excess rotational degree of freedom needs to be taken into account [183]. For strong confinement due to gravity, there is an additional anisotropy in the density along the direction perpendicular to the wall. Monomers and small chains still have freedom to translate and rotate against gravity, while for long chains only a small part of the chain (at the end) has this freedom as illustrated in Fig. 4.1b.

Note that directional assembly under extreme confinement not only occurs in model colloidal patchy particle systems. In chemistry, there are many examples where confinement has been used at its advantage. For example, nanoporous materials with pore shapes and sizes comparable to the typical size of small molecules such as metal-organic-frameworks (MOFs), covalent organic

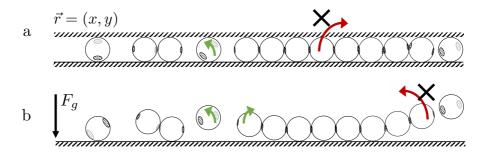


Figure 4.1: Schematic illustration of possible patchy particle orientations in quasi-2D or under the gravitational field confining the particles close to the wall (striped area). (a) In quasi-2D, i.e. with the translation restricted to the (x,y)-plane, chains cannot rotate around their center-of-mass against the confining wall (red arrow with cross) while monomers can (green arrow without cross). (b) At finite gravitational field, short chains have more freedom to translate against the gravitational force F_g compared to long chains due to the stiffness of the bonds.

frameworks (COFs), zeolitic imidazolate frameworks (ZIFs) [184, 185], and nanopores composed of for example carbon nanotubes [186]. Another example is that of self-assembled supramolecular structures where the intermolecular non-covalent bonds determine the structure and chemical function, and confinement affects the reactivity [187]. Even in the confined environment of the living cell, where short-ranged, strongly directional hydrogen bonds provide a mode for molecular assembly. Recently, the fabrication of nanoslits with Ångström-scale separation became possible opening an exciting field of nanofluidics that show unusual dynamics, kinetics, and thermodynamics due to the extreme confinement [188–191]. However, a thorough theoretical understanding of the effect of confinement on for example separation and phase transitions is still lacking [192, 193].

Such highly confined systems could be in principle described theoretically with TPT [194–196]. When solving TPT, one has to compute the interaction parameters in the theory. There are two major routes to do this: via an "integral method" [197] or via classical density functional theory (DFT) [198–200]. Solving TPT becomes increasingly complex for inhomogeneous systems due to positional and orientational coupling [201]. While extremely powerful, the DFT-route is currently not able to predict thermodynamic equilibrium for the Wertheim theory in highly confined systems at low temperatures quantitatively. See e.g. Ref. [202], which shows excellent predicted density distributions for tetrapatch particles at large wall separation, but for small wall separations (between 1.18-3.02 times the particle diameter) shows discrepancies for three different associating density functionals. In contrast, Ref. [203], following the integral route, predicted densities accurately of spherical dipatch particles in a one-dimensional pore with a width of the particle diameter.

In this paper we take a different approach. We interpret the rotational and translational freedom against the gravitational field as an additional source of entropy which effectively reduces the reactivity. We separate the polymerization reactions of the species which gives rise to adapted expressions for the chain length distributions in the Wertheim theory. By computing the interaction parameter via the integral method with Monte Carlo (MC) sampling, we can directly calculate the excess rotational and translational entropy and capture the corresponding equilibrium reaction constants between the species.

To validate our approach, we simulate patchy particles interacting via a simple square well potential combined with different forms of orientation-dependent switching functions under various gravitational strengths. Additionally, we apply the theory to the critical Casimir dipatch colloid particle system, for which the chain length distribution was experimentally studied in Ref. [53] and an accurate effective potential model was developed recently in Ref. [182]. The extended Wertheim theory contains no fit parameters, and needs only two input parameters: the species-dependent interaction parameters and the (particle) density ρ . We compare the predicted distribution with the simulated ones, and find excellent quantitative agreement.

The paper is organized as follows: we start with a brief overview of the traditional Wertheim theory that holds both for 2D and 3D. Then, we will introduce the adapted Wertheim theory for the highly confined system in quasi-2D followed by the gravitationally confined systems. Using the quasi-2D systems, we show how we can determine the excess rotational free energy of the monomers and its effect on the chain length distribution. Next, we introduce the external gravitational field which gives also short chains additional entropy and thus higher probability of occurrence and show that the flexibility of the chain also plays a role on the distributions. This effect too can be determined via the integral method giving excellent predictions of the chain length distributions of divalent colloidal particles. Finally, we apply and validate the theory on our accurate patchy particle model interacting via critical Casimir interactions under realistic gravitational conditions. We end with concluding remarks, and a future outlook.

4.2 Theory

4.2.1 First order thermodynamic perturbation theory

Consider a 3D suspension of hard spherical particles or a 2D suspension of hard disks, in which each particle is divalent, i.e dressed with two attractive patches, usually located at opposing poles. Each patch or site is able to make a bond with a site on another particle, resulting in the association of particles into linear chains. Moreover, each site is able to make only one single bond, and each bond is equally likely to form. The aggregation of the monomers into larger clusters can then be viewed as a set of addition reactions:

$$A_1 + A_1 \rightleftharpoons A_2 \tag{4.1a}$$

$$A_1 + A_2 \rightleftharpoons A_3 \tag{4.1b}$$

. . .

$$A_1 + A_{n-1} \rightleftharpoons A_n \tag{4.1c}$$

where A_1 stands for a monomer, A_2 for a dimer, and A_n for a chain composed of n monomers. This type of reactivity is also known as isodesmic polymerization where each addition reaction of

a monomer is associated with equal amount of free energy [204]. All reactions have an equilibrium constant K, defined through the law of mass action:

$$K = \frac{[A_n]}{[A_1][A_{n-1}]}$$

$$= \frac{\rho_n}{\rho_1 \rho_{n-1}},$$
(4.2)

where $[A_n]$ denotes the concentration of A_n , and ρ_n the chain density of n-mers, i.e., chains of length n.

For this situation one can apply Wertheim's first-order thermodynamic perturbation theory (TPT1), and calculate the chain length probability distribution [112, 140]. The probability of observing a non-occupied binding site is denoted as X. Then the number fraction of chains of size n is on average given by

$$\rho_n/\rho = X^2 (1 - X)^{n-1},\tag{4.3}$$

with ρ the particle density. This expression is rationalised as follows. A chain of size n has (n-1) links. The probability of forming a link is 1-X. The probability of forming n-1 links is thus $(1-X)^{n-1}$. However, as there are two unoccupied reactive sites, that accounts for a factor X^2 . So, for a monomer this reduces to $\rho_1=\rho X^2$. To convince oneself that this is consistent, one can add up all chain lengths, which would have to add up to the total density of particles:

$$\rho = \sum_{n} n\rho_n = \rho X^2 \sum_{n} n(1 - X)^{n-1}.$$
 (4.4)

The geometric sum adds up to $1/X^2$, which is indeed consistent.

Next, using Eq. 4.3 and $\rho_1 = \rho X^2$, the equilibrium reaction constant K from Eq. 4.2 is rewritten as:

$$K = \frac{1 - X}{\rho X^2}.\tag{4.5}$$

Solving for X gives

$$X = \frac{2}{1 + \sqrt{1 + 4K\rho}}. (4.6)$$

Thus, given a density ρ as well as an equilibrium constant K, Eq. 4.3 together with Eq. 4.6 form a complete description of the system.

The slope of (the log of) the chain length distribution is:

$$K\rho_1 = \frac{\rho_n}{\rho_{n-1}}$$

$$= 1 - X \equiv X_b,$$
(4.7)

where the latter equality defines the probability X_b for binding or, equivalently, the fraction of bound sites X_b .

Traditionally, TPT computes the equilibrium constant K via the interaction parameter Δ [197], as $K \equiv \langle M \rangle \Delta$, with M the number of binding sites or patches per particle. The Δ -parameter represents the (exponential of the) free energy difference of the bonding reaction with respect to the hard particle reference state. It is calculated via an integration over space of the Boltzmann weighted energy averaged over the allowed orientations of the particles, multiplied by the probability of finding a particle at distance r, i.e. the radial distribution function $g(\mathbf{r})$. The interaction parameter Δ is then:

$$\Delta = \int g(\mathbf{r}) \langle f(r, \Omega_{\alpha}, \Omega_{\gamma}) \rangle_{\Omega_{\alpha}, \Omega_{\gamma}} d\mathbf{r}, \tag{4.8}$$

where ${\bf r}$ is the inter-particle vector of particle α and γ with their orientations Ω_{α} and Ω_{γ} , respectively, $g({\bf r})$ is the pair correlation function of the reference systems e.g. hard spheres, $f(r,\Omega_{\alpha},\Omega_{\gamma})=\exp^{-\beta V({\bf r},\Omega_{\alpha},\Omega_{\gamma})}-1$ is the Mayer function and V is the energy, and, finally, $\langle \rangle_{\Omega_{\alpha},\Omega_{\gamma}}$ denotes the orientational average of the Mayer function of particle α and γ separated at distance $|{\bf r}|=r$. This calculation of Δ is non-trivial, and depends on the geometry of the setup.

4.2.2 Wertheim theory in quasi-2D

The treatment in Sec 4.2.1 assumes that all association reactions follow identical statistics. However, the situation is slightly different when confining the chain formation to a plane by e.g. two walls at particle diameter separation (Fig. 4.1A). In principle, the above described TPT/SAFT framework also applies in that case, except for one crucial difference in the assumption about the reactivity. Upon binding of single particles (free monomers), excess rotational entropy is lost. Therefore, the first reaction in the series where two free monomers react to form a dimer (Eq. 4.9a) is fundamentally different from the others where only one free monomer reacts with an existing cluster of size n > 1 (Eq. 4.9b-4.9c):

$$A_1 + A_1 \stackrel{\mathrm{K}_2}{\rightleftharpoons} A_2 \tag{4.9a}$$

$$A_1 + A_2 \stackrel{\mathrm{K}}{\rightleftharpoons} A_3 \tag{4.9b}$$

. . .

$$A_1 + A_{n-1} \stackrel{\mathrm{K}}{\rightleftharpoons} A_n \tag{4.9c}$$

which leads to an increased monomer concentration as observed in the chain length distribution. This type of polymerization can be thought of as cooperative where an initial nucleation of the polymer is followed by elongation [205–207].

By classifying not just one type of bonding reaction, but two types of reactions (see Fig. 4.2), with corresponding free energies and equilibrium constants, we derive the extended Wertheim theory in quasi-2D. For the two addition reactions, the constants K_2 and K are given by

$$K_2 = \frac{\rho_2}{\rho_1^2},$$
 and $K = \frac{\rho_n}{\rho_1 \rho_{n-1}}.$ (4.10)

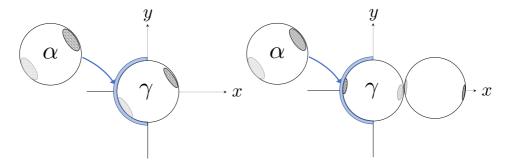


Figure 4.2: Schematic illustration of the difference in sampling K_2 and K in the left and right picture, respectively. The freely rotating α -particle is radially sampled uniformly in the integration area V (blue shaded area) around the γ -particle positioned at (0,0). Due to symmetry we can reduce the sampling volume to a hemispherical shell around the γ -particle.

Rewriting the first equation gives

$$\rho_2 = K_2 \rho_1^2 = \rho_1(K_2 \rho_1) \tag{4.11}$$

while the next addition reaction yields

$$\rho_3 = K \rho_1 \rho_2 = \rho_1(K_2 \rho_1)(K \rho_1). \tag{4.12}$$

Continuing along this line, for $n \geq 2$ it follows that

$$\rho_n = \rho_1(K_2\rho_1)(K\rho_1)^{n-2}. (4.13)$$

Note that the above equations express the densities of the chains. So adding all chain densities multiplied by the chain lengths will give the imposed particle density ρ

$$\rho = \rho_1 + \sum_{n=2} n\rho_n = \rho_1 + \sum_{n=2} n\rho_1(K_2\rho_1)(K\rho_1)^{n-2}.$$
 (4.14)

Taking out a factor K_2/K from the sum leads to

$$\rho = \rho_1 + \frac{K_2}{K} \rho_1 \sum_{n=2} n(K\rho_1)^{n-1}.$$
(4.15)

To make this a tractable sum, we add and subtract a term $\frac{K_2}{K}\rho_1$, yielding

$$\rho = \rho_1 \left(1 - \frac{K_2}{K} \right) + \frac{K_2}{K} \rho_1 \sum_{n=1} n(K\rho_1)^{n-1}. \tag{4.16}$$

When $K_2 = K$, the first term vanishes on the rhs of Eq. 4.16, recovering Eq. 4.4 in the original TPT1. In this we recover the fraction/probability of bound sites $X_b = 1 - X = K\rho_1$ (see Eq. 4.7).

The geometric sum can now be evaluated, giving

$$\rho = \rho_1 \left(1 - \frac{K_2}{K} \right) + \frac{K_2}{K} \rho_1 \frac{1}{(1 - K\rho_1)^2}.$$
 (4.17)

Next we divide by ρ , and define the monomer fraction $X_1 \equiv \rho_1/\rho$, yielding

$$1 = X_1 \left(1 - \frac{K_2}{K} \right) + \frac{K_2}{K} X_1 \frac{1}{(1 - K\rho X_1)^2}.$$
 (4.18)

Applying TPT1 amounts to solving Eq. 4.18 for the unknown monomer fraction X_1 , which in turn sets the entire chain densities ρ_2, \ldots, ρ_n in Eq. 4.11-4.13. This requires knowledge of the equilibrium constants K and K_2 that are directly proportional to Δ in Eq. 4.8, and follow from evaluating the integral. The difference between the calculations of the Δ 's corresponding to K and K_2 will be explained later in Sec. 4.3.4.

For the chain length probabilities P_n , the chain densities are normalized with the total chain density $\rho_c \equiv \sum_n \rho_n$, which, using Eq. 4.13, results, analogous to Eq. 4.17, in

$$\rho_c = \rho_1 \left(1 - \frac{K_2}{K} \right) + \rho_1 \frac{K_2}{K} \frac{1}{X} \tag{4.19}$$

so that:

$$P_{1} = \rho_{1}/\rho_{c}$$

$$P_{2} = \rho_{2}/\rho_{c}$$

$$\dots$$

$$P_{n} = \rho_{n}/\rho_{c}$$
(4.20)

In this way, also the average chain length follows: $L = \sum_{n=1} n P_n = \rho/\rho_c$.

4.2.3 Wertheim in a gravitational field

The above description for quasi-2D confinement also holds for an infinitely short gravitational height, in which translation away from the confining wall is strongly suppressed. If the gravitational field is not so strong, the particles are able to levitate on the order of the gravitational height. In turn, this translational freedom affects both the reactivity of particle association, and the free energy.

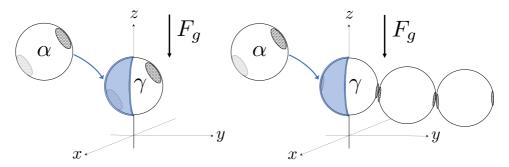


Figure 4.3: A schematic illustration of the calculation of K_2 and K_4 of particles under a gravitational field. The conformations of the γ -particle are sampled with MC allowing also translations along the gravitational field in the z-direction.

As a consequence, there may now be multiple reaction constants:

$$A_1 + A_1 \stackrel{\mathrm{K}_2}{\rightleftharpoons} A_2 \tag{4.21a}$$

. .

$$A_1 + A_{l-2} \stackrel{\mathrm{K}_{k}}{\rightleftharpoons} A_{l-1} \tag{4.21b}$$

$$A_1 + A_{l-1} \stackrel{\mathrm{K}}{\rightleftharpoons} A_l \tag{4.21c}$$

. . .

$$A_1 + A_{n-1} \stackrel{\mathrm{K}}{\rightleftharpoons} A_n \tag{4.21d}$$

where the reaction constants $K_2 \neq K_3 \neq K_k \neq K$ may not be equal with each other (see Fig. 4.3 for an illustration). Only beyond a certain chain length k (Eq. 4.21c-4.21d), the equilibrium constant can be considered to settle.

The density ρ is written as outlined in the previous section:

$$\rho = \sum_{n=1}^{\infty} n\rho_n = \rho_1 + 2\rho_2 + 3\rho_3 + \dots + n\rho_n$$

$$= \rho_1 + 2\rho_1^2 K_2 + 3\rho_1^3 K_2 K_3 + \dots + k\rho_1^k K_2 \dots K_k + \dots + (k+1)\rho_1^{k+1} K_2 \dots K_k K + \dots + n\rho_1^n \left(\prod_{m=2}^k K_m\right) K^{n-k}$$

$$= \rho_1 + \sum_{n=2}^k \left(n\rho_1^n \prod_{m=2}^n K_m\right) + \left(\prod_{m=2}^k K_m\right) \left(\sum_{n=k+1}^k n\rho_1^n K^{n-k}\right)$$

$$+ \left(\prod_{m=2}^k K_m\right) \left(\sum_{n=k+1}^k n\rho_1^n K^{n-k}\right)$$

$$(4.22)$$

The second sum in this expression converges to:

$$\sum_{n=k+1} n\rho_1^n K^{n-k} = \rho_1^k \sum_{n=k+1} n(\rho_1 K)^{n-k}$$

$$= \rho_1^k \frac{K\rho_1(k+1-kK\rho_1)}{(\rho_1 K-1)^2}$$
(4.23)

Similarly, the total chain density of the system is:

$$\rho_{c} = \sum_{n=1}^{\infty} \rho_{n} = \rho_{1} + \sum_{n=2}^{\infty} \left(\rho_{1}^{n} \prod_{m=2}^{n} K_{m} \right) + \left(\prod_{m=2}^{\infty} K_{m} \right) \left(\sum_{n=k+1}^{\infty} \rho_{1}^{n} K^{n-k} \right)$$

$$(4.24)$$

where the infinite sum converges to:

$$\sum_{n=k+1} \rho_1^n K^{n-k} = \rho_1^k \frac{K\rho_1}{1 - K\rho_1}$$
(4.25)

Again, for given density ρ and reaction constants K_2, \ldots, K_k and K, the only unknown is the monomer fraction $X_1 = \rho_1/\rho$ (Eq. 4.22 and 4.23). As Eq. 4.22 is a higher order polynomial, it should be (it is) solved numerically.

4.3 Simulation Methods

4.3.1 General patchy particle pair potential

To test our extension of TPT1 under strong confinement, we simulate several systems with a variety of potentials, from simple toy systems to more accurate ones. The general expression for the pair interaction $V_{\rm pair}$ between two patchy particles i and j with orientation Ω_i and Ω_j , respectively, and separated by a distance r_{ij} , is

$$V_{\text{pair}}(r_{ij}, \Omega_i, \Omega_j) = V_{\text{rep}}(r_{ij}) + \min_{1 \le k, l \le n_p} V_{\mathbf{p}_{ik}, \mathbf{p}_{jl}}(r_{ij}, \Omega_i, \Omega_j)$$
(4.26)

where $V_{\rm rep}$ denotes an isotropic repulsive potential and $V_{{\bf p}_{ik},{\bf p}_{jl}}$ patch-patch attractive interaction [182]. The position of each patch in the particle reference frame is given by n_p unit patch vectors ${\bf p}$, which point from the particle's center to the center of the patch (Fig. 4.4). The min function gives the minimum energy of the set of all possible patch-patch combinations and mimics the fact that we restrict our particles to form only one bond per particle pair. For our systems, the range and width of the patch interaction is relatively small, so that this condition is easily fulfilled.

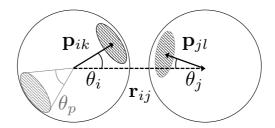


Figure 4.4: A schematic illustration of the interparticle vector \mathbf{r} (dotted arrow), patch vectors \mathbf{p} on each particle (solid arrows), and the angles θ , and the patch size is defined by the angle θ_p

The attractive patch-patch potential is defined as [182]

$$V_{\mathbf{p}_{ik},\mathbf{p}_{jl}}(r_{ij},\Omega_i,\Omega_j) = V_{\text{attr}}(r_{ij})S'(\Omega_i)S'(\Omega_j), \tag{4.27}$$

where $V_{\rm attr}(r_{ij})$ is an isotropic attractive potential. As the patches turn away from each other, the patch-patch interaction becomes weaker as the area of overlap in between the patches decreases. This anisotropy of the patch interactions is captured by the two switching functions S' that are each a function of the orientation Ω of each particle. See Ref. [182] for more details.

SQUARE WELL PAIR POTENTIAL

The simple toy systems employs a hard sphere with diameter σ and a square well attraction (Fig. 4.5). The hard sphere repulsive potential is

$$V_{\rm HS}(r) = \begin{cases} \infty & r < \sigma \\ 0 & \text{otherwise} \end{cases}$$
 (4.28)

together with a square well attraction:

$$V_{\text{squarewell}}(r) = \begin{cases} \epsilon & \sigma < r \le \sigma + \delta \\ 0 & \text{otherwise} \end{cases}$$
 (4.29)

where $\delta=0.005\sigma$, and $\beta\epsilon\in[-20,-5]$ corresponding to a reduced temperature $T^*=-1/\beta\epsilon\in[0.05,0.20]$ with $\beta=1/k_{\rm B}T$ the inverse temperature and $k_{\rm B}$ the Boltzmann constant. Note that this square well is rather narrow.

The switching function $S'(\Omega)$ is defined as:

conical, also known as the Kern-Frenkel potential [64, 208]:

$$S_{\text{KF}}(\theta, \theta_{\text{p}}) = \begin{cases} 1 & \theta \le \theta_{p} \\ 0 & \theta > \theta_{p} \end{cases} \tag{4.30}$$

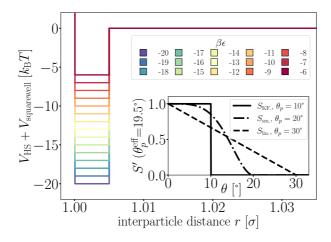


Figure 4.5: The toy model radial potential composed of the hard sphere repulsion $V_{\rm HS}$ and square well attraction $V_{\rm squarewell}$. The inset shows the three switching functions $S_{\rm KF}$ (conical, Eq. 4.30), $S_{\rm sm.}$ (smooth, Eq. 4.31), and $S_{\rm lin.}$ (linear, Eq. 4.32).

• smooth [97]:

$$S_{\text{sm.}}(\theta, \theta_{\text{p}}) = \begin{cases} \frac{1}{2} \left(1 - \cos\left(\pi \frac{\cos(\theta) - \cos(\theta_{\text{p}})}{1 - \cos(\theta_{\text{p}})}\right)\right) & \theta \le \theta_{\text{p}} \\ 0 & \theta > \theta_{\text{p}} \end{cases}$$
(4.31)

• or linear:

$$S_{\text{lin.}}(\theta, \theta_{\text{p}}) = \begin{cases} 1 - \theta/\theta_{\text{p}} & \theta \le \theta_{p} \\ 0 & \theta > \theta_{p} \end{cases}$$
(4.32)

where θ is the angle between the interparticle vector \mathbf{r} and the patch vector \mathbf{p} , and $\theta_{\rm p}$ is the patch size (Fig. 4.4). As shown in the inset in Fig. 4.5, the patch size $\theta_{\rm p}$ was varied from 10, 20, and 30° for the $S_{\rm KF}$, $S_{\rm sm.}$ and $S_{\rm lin.}$ switch functions, respectively.

THE CRITICAL CASIMIR PAIR POTENTIAL

The accurate effective critical Casimir potential of the dipatch particles has its own radial dependence and switching function. In chapter 3, we optimized the potential based on physical dimensions of the dipatch particles and theoretical critical Casimir potentials, to reproduce chain length distributions and bending rigidities observed in experiment over a weak to strong interaction range as function of the temperature [182]. The optimized parameters w=0.462, Υ =-0.09e/nm², and $\theta_p^{\rm eff}$ =19.5° were used (Fig. 5.5).

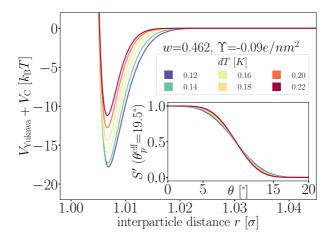


Figure 4.6: The patchy particle radial potential for dipatch particles composed of Yukawa repulsion $V_{\rm Yukawa}$ (Eq. 3.2) and critical Casimir attraction $V_{\rm C}$ (Eq. 3.6). The potential uses variables w=0.462, Υ =-0.09 e/nm^2 , and θ_p^{eff} =19.5°. The inset shows the switching functions that are additionally a function of dT.

4.3.2 EXTERNAL POTENTIAL

The external potential $V_{\rm ext}$ at quasi-2D confinement prohibits the translation in the z-direction via:

$$V_{\text{quasi-2D}}(z) = \begin{cases} 0 & z = 0\\ \infty & z \neq 0 \end{cases}$$

$$(4.33)$$

which mimics two hard walls separated by the particle diameter (Fig. 4.1a).

The external gravitational potential is composed of two terms: a hard wall represented by a steep Lennard-Jones potential V_{LJ} and a gravitational potential V_q that depends, among other things, on the mass of the particle. See the appendix B2 of Ref. [182] for more details. The resulting total gravitational potential is:

$$V_{\text{gravity}}(z) = \begin{cases} V_{\text{LJ}}(z) & z \le z_{\text{cut}} \\ V_g(z) & z > z_{\text{cut}} \end{cases}$$
(4.34)

$$V_{\text{gravity}}(z) = \begin{cases} V_{\text{LJ}}(z) & z \le z_{\text{cut}} \\ V_g(z) & z > z_{\text{cut}} \end{cases}$$

$$= \begin{cases} 4\epsilon_{\text{LJ}} \left(\left(\frac{\sigma}{z} \right)^{12} - \left(\frac{\sigma}{z} \right)^6 + \frac{1}{4} \right), & z \le z_{\text{cut}} \\ -F_g z - b, & z > z_{\text{cut}} \end{cases}$$

$$(4.34)$$

where $\epsilon_{\rm LJ}$ is an arbitrary (high) value set to $500k_{\rm B}T$ and the gravitational force F_q is varied from -3.85, to -7.70, and to -11.55 $k_{\rm B}T/\sigma$. These gravitational forces ranges from 0.5, 1.0, and 1.5 times the gravitational force of the dipatch particle of interest, respectively. Parameters b and $z_{\rm cut}$ are chosen such that both the potential and the force are continuous at $z_{\rm cut}$.

4.3.3 The system's potential energy

The system's potential energy is a sum over all pair potentials and the external field

$$V = \sum_{i < j}^{N} V_{\text{pair}}(r_{ij}, \Omega_i, \Omega_j) + \sum_{i}^{N} V_{\text{ext}}(z_i)$$
(4.36)

where i and j run over the N colloidal particles. The external potential V_{ext} is either $V_{\text{quasi-2D}}$ or V_{gravity} .

4.3.4 The calculation of Δ

The integral in Eq. 4.8 is performed using Monte Carlo integration via:

$$\Delta = V \left\langle g(\mathbf{r}) \left\langle f(r, \Omega_{\alpha}, \Omega_{\gamma}) \right\rangle_{\Omega_{\alpha}, \Omega_{\gamma}} \right\rangle_{V}$$
(4.37)

where the average over the radial distribution function and Mayer function takes place in the integration volume $V=\int d{\bf r}$. The monomers are indicated by α and the other reactant is the γ -particle. Each reaction constant K_m in the polymerization is thus defined by the orientational and positional distribution of the reactants and a separate computation of the corresponding Δ_m must be done.

Correct determination of the averages is key to calculate Δ . There are two options to measure the average: (1) sample homogeneously over space multiplied with the probability distribution or (2) sample from the correct distribution. This applies to both orientational $\langle \rangle_{\Omega_{\alpha},\Omega_{\gamma}}$ as well as the translational $\langle \rangle_{V}$ parts of the integration. An advantage of Monte Carlo integration is that it is capable of evaluating both averages simultaneously.

The α -particle, and the γ -particle if it is unbound, are free monomers and their orientational distribution is uniform. Giving them random orientations samples the distribution as option (2). The γ -particle's z-positional distribution is described by the (Boltzmann distribution of the) external potential $V_{\rm ext}$, and is sampled as option (2). If the γ -particle is restricted to bound configurations, its orientational and positional distributions are additionally described by the pair potential. So instead of uniformly sampling orientational and positional space, its configurations are sampled from a chain with MC (Fig. 4.2b). Note that this MC sampling of the γ -particle's bonding configurations is independent of the MC sampling of Δ (Eq. 4.37) and may be performed on-the-fly or beforehand. Thus, the contribution of the orientations Ω_{α} and Ω_{γ} on the average is incorporated using option (2).

The contribution of the inter-particle distance r on the average is sampled by placing the α -particle randomly in a hemispherical shell of volume V around the γ -particle. The radial distribution function then gives the probability of finding the α -particle at distance r. Thus, the contribution of the inter-particle distance on the average is incorporated using option (1).

4.3.5 SIMULATION DETAILS

EXPLICIT MC SAMPLING OF CHAIN LENGTH DISTRIBUTIONS

Systems with the square well radial potential were simulated with MC for N=1000 divalent particles in a cubic box of length 51.17σ or 62.67σ with periodic boundary conditions to resemble a density of $\rho=0.382$ or 0.255 N/σ^2 , respectively. Due to the extreme confinement forming a monolayer of particles in the (x,y)-plane, the density is expressed in units of number of particles per area in the (x,y)-plane. The particle densities were chosen to yield reasonable chain length distributions, i.e. that probabilities for longer chain were nonzero. The systems with the critical Casimir potential were taken from Ref. [53]. These simulations were done in a rectangular box of dimensions $43.5\sigma \times 60\sigma \times 43.5\sigma$ with periodic boundary conditions containing 666, or 1000 particles which corresponds to $\rho=0.255$ or 0.382 N/σ^2 , respectively.

Starting from a random starting configuration MC moves were performed to equilibrate and measure the systems as explained in detail in Ref. [182]. Depending on the interaction strength and form of switch function, the equilibration consisted of 1×10^4 to 6×10^4 MC cycles and the measurements of 5×10^4 to 2×10^5 MC cycles. Each MC cycle consists of 5×10^5 single particle (95%) and cluster moves (5%).

The chain length distribution was measured from three independent simulations after each MC cycle by counting the number N_n of chains of length n and normalize by the total number of chains in the system yielding $P_n = N_n / \sum_{n=1} N_n$. Irrespective of the use of the discontinuous (square well) or continuous (critical Casimir) attractive potential, a bond is defined for a pair of particles if $V_{\mathbf{P}_{ik},\mathbf{P}_{il}}(r_{ij},\Omega_i,\Omega_j) < 0k_BT$.

MC sampling of Δ

For the calculation of the volume average $\langle \rangle_V$ in Eq. 4.37 we employ three loops. In the first loop of 10^4 cycles, the configurations of the γ -particle are sampled. For the quasi-2D system, a monomer and dimer configuration are sufficient as there are only two reaction constants. For the gravitational systems, equilibrated chains with length $l \leq 15$ are decorrelated with 10^5 single particle MC moves. The position and orientation of the hemi-sphere of the free site is saved as the γ -particle. In the second loop of 10^2 cycles, the new position of the α -particle is set to $\vec{r}_{\alpha} = \vec{r}_{\gamma} + r\vec{e}$ where r is a random distance $r \in [\sigma, \sigma + \delta]$ and \vec{e} a random unit vector pointing to the γ hemi-sphere. The radial distribution function gives the probability of finding the particles at positions \vec{r}_{α} and \vec{r}_{γ} in the hard particle reference, more details are in section 4.3.5. In the third loop of 10^3 cycles, the α -particle is given random orientations and the Mayer function is calculated for the sampling of the $\langle \rangle_V$. To improve the calculation of the average, the α -particle was given six sites instead of two. In total there are 2×6 possible patch combinations, two from the γ and six from the α -particle, leading to a simple correction of 1/12. The final step to calculate Δ is to multiply the $\langle \rangle_V$ with the volume of the hemispherical-shell V. The loops may be repeated one to three times independently, depending on the convergence.

THE RADIAL DISTRIBUTION FUNCTION

The radial distribution function (RDF) of the hard sphere reference fluid is important for the radial component of Δ . The quasi-2D system is radially isotropic in the (x, y)-plane, we thus

may use a heuristic RDF $g_{\rm HD}(r)$ of hard disks [209, 210]. For the gravitationally confined systems, MC simulations are performed to measure the radial distribution of hard spheres at various densities and gravitational fields. The RDF was saved to a file and uses the distance between the particles $r=|\vec{r_{12}}|$, and the z-coordinates of the particles z_1 and z_2 as variables. A bin width of $dr=0.05\sigma$ and $dz=0.01\sigma$ in combination with a simple flooring of the bin was sufficient to determine the corresponding RDF during the Δ -calculation.

The reference hard particle diameter d when using the square well potential is simply $d=\sigma$ as the attractive part of the potential is taken as the perturbation. While for the critical Casimir patchy particle potential, we use the WCA separation to determine $d=\int_0^\infty (1-\exp(-\beta v_0))dr$ with v_0 being a smooth repulsive potential [111, 211]. In principle, the diameter d is also a function of the orientation, as $V_{\rm pair}$ is a function of r, Ω_i , and Ω_j (Eq. 4.26) . However, the attractive potential is rather narrow and to avoid a varying reference diameter, the repulsive potential v_0 in the WCA separation is taken at maximum attraction, i.e. $V_{\rm pair}=V_{\rm Yukawa}(r)+V_C(r)$, and used as a constant.

Numerically solving X_1

Given the density and the reaction constants, we determine the monomer fraction X_1 which is bound to $X_1 \in [0,1]$ using the *solve*-function from the *SymPy*-Python package [212]. There may be multiple (imaginary) solutions to the equations 4.18 or 4.22, and solutions containing a very small imaginary part ($\operatorname{Im}(X_1) < 10^{-30}$) were accepted. In case of multiple solutions for X_1 , the smallest one was taken to solve the chain length distribution.

4.4 RESULTS AND DISCUSSION

To check the predictions of the extended Wertheim theory, we compare predicted and simulated chain length distributions in quasi-2D of systems with a square well radial potential for the three different switching function at a wide range of attractive strengths. The resulting simulated (symbols) and predicted (solid lines) chain length distribution are shown in Fig. 4.7. The top panel shows dipatch particles with a conical switch function $S' = S_{KF}$ with patch size $\theta_p = 10^\circ$ at $\rho = 0.382 N/\sigma^2$, the middle panel $S' = S_{sm.}$ with $\theta_p = 20^\circ$ at $\rho = 0.255 N/\sigma^2$, and the lower panel a $S' = S_{lin.}$ with $\theta_p = 30^\circ$ at $\rho = 0.382 N/\sigma^2$. The hallmark of all distribution is a clear increased monomer density that does not follow the exponential decay of the sequential polymerization, and is well described by the theory. All systems show excellent agreement between model predictions and simulations for all radial interaction strengths, forms of switching function and densities.

These quasi-2D systems allow for determination of the associated excess rotational entropy which can be directly determined from the ratio of chain probabilities. For the initial dimerization, the two monomers lose an excess rotational entropy $2 \times F_{\rm rot}$ and gain a bonding free energy $F_{\rm bond}$, making $\exp(-\beta(F_{\rm bond}-2F_{\rm rot})) = P_2/P_1 = K_2\rho_1$. For the subsequent polymerization steps, only one monomer loses $F_{\rm rot}$ and $F_{\rm bond}$ is gained, thus $\exp(-\beta(F_{\rm bond}-F_{\rm rot})) = P_3/P_2 = K\rho_1$.

In Fig. 4.8, the resulting (exponents) of these free energies are collected for various patch types and sizes, and interaction strength at $\rho=0.382N/\sigma^2$. For the conical potential with $S'=S_{\rm KF}$, the excess rotational entropy is independent of the interaction strength and only a

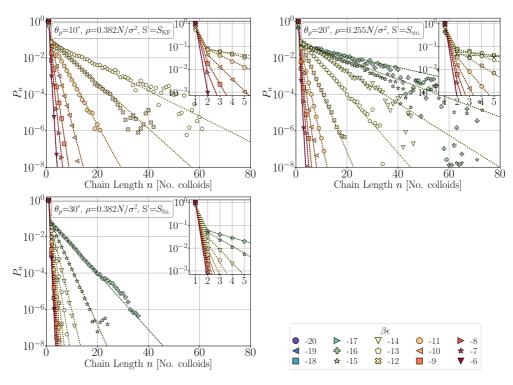


Figure 4.7: Predicted (solid lines) and simulated (symbols) chain length distributions of systems at various interactions strength ($\beta\epsilon$ indicated by colors and symbols), switch function type S' defined in Eq. 4.30-4.32, and density ρ [N/σ^2]. The inset shows the probabilities at small chain lengths.

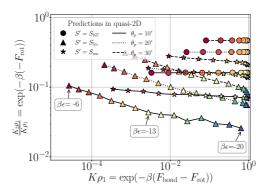


Figure 4.8: The predicted (exponents of the) excess rotational entropy $\beta F_{\rm rot}$ and the bonding free energy $\beta F_{\rm bond}$ of square well radial potentials with various switching functions in quasi-2D confined at $\rho=0.382N/\sigma^2$. The same color coding for $\beta\epsilon$ from Fig. 4.7 is used, while the symbols (S' type) and lines ($\theta_{\rm p}$) are specified in the legend.

function of the patch size θ_p . In that case, the bonding probability is a purely geometrical factor and, as expected, larger patch sizes contain less excess rotational entropy. Non-conical switch functions, namely $S_{\rm sm.}$ and $S_{\rm lin.}$, are dependent on the interaction strength. Here, stronger

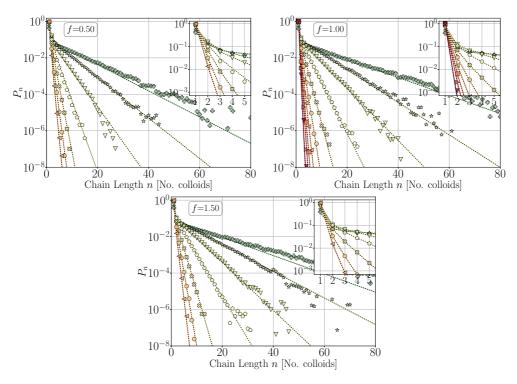


Figure 4.9: Predicted (solid lines) and simulated (symbols) chain length distributions of systems with $S'=S_{\rm sm.}$ and ρ =0.255 N/σ^2 . The gravitational force is varied form f=0.5, 1.0 and 1.5 times $F_g=-7.70k_{\rm B}T/\sigma$. The same symbol/color coding of Fig. 4.7 is used.

interaction strengths lead to stiffer chains, and thus to more excess rotational entropy for the monomers.

Fig. 4.9 shows simulated (symbols) and predicted (solid lines) chain length distribution of the square well radial potentials with switching function $S'=S_{\rm sm.}$, and $\theta_{\rm p}$ =20° at $\rho=0.255N/\sigma^2$ with a gravitational force of f=0.5, 1.0 and 1.5 times $F_g=-7.70k_{\rm B}T/\sigma$. Again, very good agreement between predicted and simulated distributions is observed. Since the predictions included a varying K up to and including chain length l=8 (Eq. 4.21b-4.21d), the distributions show a gradual change of the initial slope of the exponential decay, manifesting the gradual change of the reaction constant, as clearly shown in the insets. For f=1.50, in contrast, the distributions start to resemble more the quasi-2D systems and showing a sharp transition K_2 to K_3 and $K_3 \approx K_4$. This suggest that for higher gravitation one may consider only smaller changes, and fewer reaction constants.

Now that we have shown that our extended Wertheim theory is able to incorporate the effects of the gravitational field and the hard wall on the chain length distributions, we can show the role of chain's flexibility on its distribution at finite gravity. The binding rigidity is related to excursions of the bending angle θ due to the thermal fluctuations that are on the order of $1/\beta\epsilon$. The faster S' decays as function of θ (see e.g. the insets of Fig. 4.5 and 5.5), the stiffer the bond. When we select two systems with comparable K_2 and K, i.e. $F_{\rm rot}$ and $F_{\rm bond}$, in quasi-2D, their distributions are similar (Fig. 4.10, solid lines). If these system are in a finite gravitational field

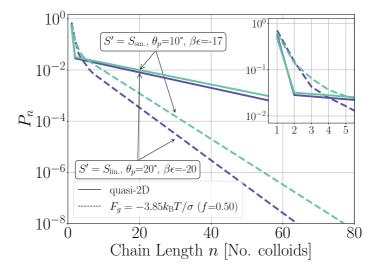


Figure 4.10: The stiff chain (purple, $S'=S_{\rm lin.}$), and the more flexible chain (green, $S'=S_{\rm sm.}$) render the same predicted distribution in quasi-2D (solid lines) at $\rho=0.382N/\sigma^2$. While when in a gravitational field with $F_g=-3.35k_{\rm B}T/\sigma$, the distribution do not overlap (dashed lines). Both potentials use a square well radial potential.

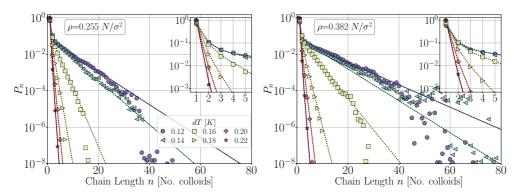


Figure 4.11: Predicted (solid lines) and simulated (symbols) chain length distributions of systems interacting via critical Casimir interactions under a realistic gravitational field at ρ =0.255 and 0.382 N/σ^2 . Both graphs use the legend in the left graph.

instead, their statistics start to diverge significantly from each other (Fig. 4.10, dashed lines). We assign this divergence to the flexibility of the chains: higher stiffness makes the alignment of the particles with the wall more prominent and reduces their reactivity. This example emphasizes the complexity of the orientation-position-dependent reactivity. As a results, there is no direct mapping of the statistics in quasi-2D to finite gravitational strength.

Finally, we can apply the extended Wertheim theory to the experimentally relevant system of patchy particles interacting via the critical Casimir force shown in Fig. 4.11. We can confirm that the approximations done for the RDF, namely using the WCA separation of the repulsion and attraction, and fixing the hard sphere reference diameter d are sufficient. The theory predicts the distribution at various interaction strengths well, except for the strong interaction

strengths at dT=0.14 and 0.12K. At this region, the simulations at dT=0.14K and $\rho=0.382N/\sigma^2$ show significantly longer chain lengths than predicted due to the formation of nematic phases that promote longer chains[53]. The current theory uses an isotropic distribution in the (x,y)-plane and can thus not predict the enhanced reactivity due to the nematic phase.

Nematic phases additionally slow down the growth kinetics [53]. This is also where the simulations have difficulty converging; at dT=0.12K at both densities, the chains in simulation are still shorter than predicted. In addition, the slowdown of the growth kinetics may be caused by the relatively narrow switching function in combination with the strong attraction of the critical Casimir potential.

4.5 Conclusions

In this work we have extended the Wertheim first-order perturbation theory to describe self-assembly of divalent particles under extreme confinement by introducing additional reaction equilibrium constants that account for the reduction of rotational and translational entropy and bond free energy of the polymerization. In the tested systems, the confinement to a monolayer of particles is created by a gravitational field that leads to sub-diameter gravitational heights and an anisotropy of particle density in the direction perpendicular to a wall.

Explicit calculation of these reaction constants from the interaction potential via the integral method allowed for a prediction of the entire chain length distribution functions that agree excellently with direct simulations of these systems. An essential part of the theory is the radial distribution function of the reference hard particle. For finite gravity, this reference hard particle distribution is computed explicitly, but only once for a certain density. The computation of the interaction parameters Δ can then be done for all densities simultaneously.

In quasi-2D, we can separate the excess rotational entropy from the bonding free energy; the results show that the patch form, size and interaction strength all play a role on the rotational free energy for non-conical potentials, while for conical potentials only the patch size matters. Additionally, we illustrate that there is no direct or straightforward mapping of the statistics in quasi-2D onto the gravitational systems as the chain's flexibility – thereby availability of the bonds – defines its reactivity. This complex position-orientation-dependent reactivity can be explicitly determined by our method.

As one might expect, due to the formation of nematic phases that are, in fact, also observed in experiments, our approach breaks down. One of the assumptions, that the chains will form isotropically in the (x,y)-plane no longer holds. This situation is beyond the scope of the current work.

The advantage of the approach is that it only needs an approximate form of a reference radial distribution function to allow quantitative prediction of an entire range of densities and does not rely on various forms of associating density functionals. Moreover, the approach allows to understand and explain the anomalous small chain concentration of self-assembly under sedimentation conditions.

Finally, we foresee that for other (molecular) self-assembling systems that are described by Wertheim's theory in bulk, our novel extended theory can be applied to describe the system's behavior in extreme confinement or under an external field, e.g. in nanoslits, as the theory is validated not only for toy models but also for realistic potentials.

5

ACTIVITY AFFECTS THE STABILITY, DEFORMATION AND BREAKAGE DYNAMICS OF COLLOIDAL ARCHITECTURES

Living network architectures, such as the cytoskeleton, are characterized by continuous energy injection, leading to rich but poorly understood non-equilibrium physics. There is a need for a well-controlled (experimental) model system that allows basic insight into such non-equilibrium processes. Activated self assembled colloidal architectures can fulfill this role, as colloidal patchy particles can self-assemble into colloidal architectures such as chains, rings and networks, while self-propelled colloidal particles can simultaneously inject energy into the architecture, alter the dynamical behavior of the system, and cause the self-assembled structures to deform and break. To gain insight, we conduct a numerical investigation into the effect of introducing self-propelled colloids modeled as active Brownian particles, into a self-assembling colloidal dispersion of dipatch and tripatch particles. For the interaction potential, we use a previously designed model that accurately can reproduce experimental colloidal self-assembly via the critical Casimir force [182]. Here, we focus primarily on the breakage dynamics of three archetypal substructures, namely, dimers, chains, and rings. We find a rich response behavior to the introduction of self-propelled particles, in which the activity can enhance as well as reduce the stability of the architecture, deform the intact structures and alter the mechanisms of fragmentation. We rationalize these finding in terms of the rate and mechanisms of breakage as function of the direction and magnitude of the active force by separating the bond breakage process into two stages: escaping the potential well and separation of the particles.

5.1 Introduction

Structural architectures in living cells, such as the cytoskeleton in muscle or plant tissue, are both viscoelastic and active, i.e. undergo continuous injection of energy, leading to remarkable collective, non-equilibrium properties. Networks made of these living polymer filaments can be viewed as active gels [104], a fascinating class of materials that show rich, responsive and functional mechanical properties such as cell motility, replication and growth, and tissue repair [213, 214]. Therefore, such soft biological materials are of great fundamental and technological relevance. Indeed, one of the promising directions in material science is to mimic driven biological systems in the form of active (gel) architectures, where active particles provide continuous energy injection.

While much research is being done in this area, both on biological materials [214, 216–220] as well as simplified physical systems[131, 221–225], there is a need for well controlled model systems that would allow us to investigate the fundamental physical properties of such driven materials in a systematic way. In this work we investigate activated breakage of self-assembled colloidal architectures.

Experimental breakthroughs in nanostructure assembly and active matter provide such prototypical systems. For instance, novel synthesis routes enable the design of colloidal particles surface-decorated with DNA [51, 52] or patches of a materials with different surface properties compared to bulk enabling formation of directed bonds [38, 50, 63, 226]. Suspending the latter type of patchy particles in a near-critical binary liquid mixture (e.g. water and lutidine), induces attractive directed bonds between the patches on the surface of neighboring particles via a solvent mediated critical Casimir force. These attractive bonds allow the controlled self-assembly into complex structure such as chains, rings, and networks [38, 53, 54, 57, 138]. Experiencing thermal motion, such patchy particles obey the Boltzmann distribution, and thus can be seen as mesoscopic analogs of atoms. As they can be directly observed via, e.g., confocal microscopy, patchy particles can act as an experimental model system to explore complex self-assembled colloidal architectures analogous to their molecular counterparts [53, 57, 58, 227].

At the same time, well-controlled self-propelling particle systems allow experimental control of microscopic energy injection [228, 229]. Examples of these particles are gold coated Janus particles that are self-propelled by catalysis of e.g. hydrogen peroxide, or colloids that are driven via external electric, magnetic or optical fields. [122, 133] These processes induce an active force aligned along the particle orientation. As the particle is still free to rotate in the suspension, such active particles' dynamics are often modeled as Active Brownian Particles (ABPs).

Here, we combine the two experimental breakthroughs in a simulation study to explore the collective non-equilibrium response of colloidal architectures to the introduction of activity. We aim to obtain microscopic insight into the two main effects of introducing activity: 1) how does the active force lead to the breaking of colloidal chains? In particular, what effect does activity have on the bond configurations before escaping the potential well, and how does activity affect separating the particles into the bulk. Specifically, we look into the breakage mechanism, position and - rate. 2) how is the dynamics of a colloidal architecture, such as a ring or a network, altered by such active forces. For that, we investigate global bending modes of rings.

To address these questions, we combine ABPs with patchy particles interacting via the critical Casimir force in Brownian dynamics simulations. To make a connection to the experimental realization of these systems, we would like to stay as close as possible to the experimental condi-

$$\text{TPP} \phi = 120^{\circ} \quad \text{DP} \phi = 180^{\circ}$$

Figure 5.1: TPP particles have a 120° angle and DP particles a 180° angle between their patches.

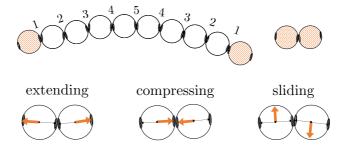


Figure 5.2: Schematic illustrations of the DP particle decamer (including irreducible bond numbers) and dimer. The orange colored particles are made active using three directions of active forces (orange arrows) opposing the patch (black arrow), along the patch, perpendicular to the patch indicated as extending, compressing or sliding forces, respectively.

tions. Therefore, we employ our accurate potential model for patchy particle systems that was benchmarked on experiments [182].

We find that the response to activity yields a rich behavior, in which activity can both enhance and reduce the stability of architecture, as well as alter the mechanism of fragmentation.

The paper is organized as follows. In the next section we introduce the systems, the potential model, and simulation and analysis methods. In Sec. 5.3, we present and discuss the simulation results for dimers, decamers and rings. We end with concluding remarks.

5.2 Methods

5.2.1 Simulation Details

PATCHY PARTICLE ARCHITECTURES

In this work, we investigate two types of self-assembled structures: chains, and rings. The chains are composed of colloidal divalent patchy, or dipatch (DP), particles that have two attractive patches at opposite sites of the particle (Fig. 5.1). We consider two chain lengths: dimers consisting of just two, and decamers consisting of ten self-assembled DP particles. The outer two particles in the chains are made active by considering self-propelled forces acting on the centers of the particles in three qualitatively different ways, by compressing, extending, and sliding along the patch-patch bond (see Fig. 5.2). In contrast to a dimer, for which the activity is directly mediated by a single bond, the decamer can and must propagate the active force along the passive particles in the chain. For analysis purposes, we give each bond in the decamer an index; due to symmetry, there are only five irreducible bond numbers (Fig. 5.2).

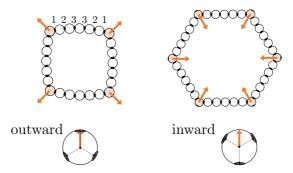


Figure 5.3: Schematic illustrations of the ring structures with four, illustrated with outward-facing forces, or six, illustrated with inward-facing forces, TPP particles connected by five DP particles named T4D5 and T6D5, respectively. The orange colored particles are made active TPP particles with their force directing towards a patch or between two patches creating outward-facing or inward-facing forces in the ring, respectively.

The ring structures are symmetric and composed of four or six trigonal planar patchy (TPP) particles connected via 5 or 15 DP particles. Figure 5.3 illustrates the structures T4D5 and T6D5 where the number after the T indicates the number of TPP particles, and after the D the number of DP particles connecting the TPP particles in the chain. Also the bonds in the rings are labeled, due to symmetry, there are only three or eight irreducible bond numbers for the 5 and 15 DP particle-based rings, respectively. The square structures with four TPP particles naturally contain an additional tension due to the mismatching bond angle of the TPP particle. Figure 5.3 shows how the self-propulsion forces acting on the TPP particle either point toward the patch and creates outward-facing forces with respect to the ring, or between two patches resulting in inward-facing forces with respect to the ring.

The ring simulations are performed in the presence of a gravitational potential that makes the particles sediment to a horizontal surface with a gravitational height of 0.13 times the diameter σ similar to the typical experimental setup employing critical Casimir forces.

Interaction potential

The effective anisotropic pair interaction between two patchy particles i and j with orientation Ω_i and Ω_j , respectively, and interparticle distance r_{ij} is given by

$$V_{\text{pair}}(r_{ij}, \Omega_i, \Omega_j) = V_{\text{Yukawa}}(r_{ij}) + V_{\text{C}}(r_{ij})S(\Omega_i, \Omega_j), \tag{5.1}$$

where V_{Yukawa} denotes an isotropic repulsion and the second term denotes the relevant patchpatch attraction between the particles i and j, where we assume that each particle pair can only form a single bond. This condition is easily fulfilled for our systems, as the range and width of the patchy critical Casimir interaction is relatively small, and only one patch combination will result in an effective attraction.

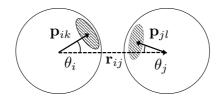


Figure 5.4: A schematic illustration of the inter-particle vector \mathbf{r} (dotted arrow), patch vectors \mathbf{p} on each particle (solid arrows), and the angles θ .

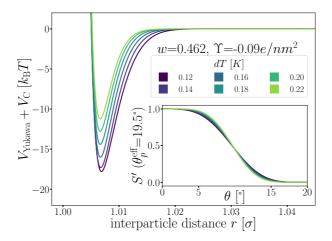


Figure 5.5: The patchy particle radial potential for dipatch particles composed of Yukawa repulsion $V_{\rm Yukawa}$ (Eq. 3.2) and critical Casimir attraction $V_{\rm C}$ (Eq. 3.6). The inset shows the switching functions S' that are additionally a function of dT.

The anisotropy of the patch interactions is captured by two switching functions $S'(\theta)$ that are in principle a function of the orientations Ω of both particles, but are simplified to a dependency on the angles θ of each particle

$$S(\Omega_i, \Omega_j) = \max_{1 \le k, l \le n_n} S'(\theta_{ik}) S'(\theta_{jl})$$
(5.2)

where the position of each patch in the particle reference frame is given by n_p unit patch vectors \mathbf{p} , which point from the particle's center to the center of the patch as shown in Fig. 5.4. Each particle pair can only form one bond which is mimicked by the max function in S resulting in the minimum attractive energy of the set of all possible patch-patch combinations in Eq. 5.1.

Figure 5.5 shows the optimized patchy particle potential that is capable of reproducing the experimental system of DP particles. The exact functional forms of the Yukawa electrostatic repulsion, critical Casimir attraction, and the switching functions S' can be found in the Appendix of Chapter 3 and Ref. [182] Appendix B.

The total potential energy of the system is the sum of all patchy particle pair interactions, and an external gravitational potential $V_{\rm ext}(z_i)$

$$V = \sum_{i < j}^{N} V_{\text{pair}}(r_{ij}, \Omega_i, \Omega_j) + \sum_{i}^{N} V_{\text{ext}}(z_i)$$
(5.3)

where i and j run over the N colloidal particles, and z is the vertical distance to the surface. Details about $V_{\text{ext}}(z_i)$ can be found in Ref. [182] section II.D and Appendix B of Chapter 3.

EQUATIONS OF MOTION

See Sec. 2.4 for a detailed description of the equation of motion of (active) Brownian particles. The translational and rotational diffusion constant are $D_{\rm T}$ =0.0034 σ^2/s , $D_{\rm R}$ =0.05 rad $^2/s$ and as experimentally measured for dipatch particles with diameter $\sigma=3.2\mu m$ [54, 56].

Monte Carlo

The BMD simulations are started from configurations that are equilibrated and decorrelated. To create this collection of starting configurations, we use Monte Carlo (MC) [182]. For a given colloidal architecture, only single particle MC moves are performed and those MC steps that lead to bond breakage, i.e. $E_{\rm pair} \geq 0$, are rejected. In the single particle move, a randomly selected particle is randomly rotated (50% of the MC steps) around their center of mass with a randomly selected rotation magnitude $dq \in [0, \theta_{\rm max}]$ or randomly translated with a magnitude $dr \in [0, r_{\rm max}]$. When the gravitational potential is applied, the z-direction of the random translation is divided by 10 to prevent placing the particle inside the wall or against the gravitational field which leads to unfavorable energies.

5.2.2 Analysis

BOND BREAKAGE PROCESS

Starting from equilibrated structures, we conducted straightforward, "brute force" BMD simulations to analyze bond breakage. Due to the random fluctuations or with the aid of the active force, a bonded particle pair can escape its attractive well. The particle pair either rebinds going back into the attractive well, or increases their interparticle distance to $r=1.5\sigma$ at which we assume the probability of rebinding is sufficiently low [230]. Only the latter criterion is considered a true bond breakage upon which the simulation is halted.

To analyze the bond breakage mechanism and lifetime, we separate the bond phase space into four regions indicating a strongly bound (1), weakly bound (2), diffusive (3), and truly broken (4) state as illustrated in Fig. 5.6. We define these four regions using the energy E_{λ} that is a parameter between zero and one:

$$E_{\lambda} = V_{\rm C}(r_{\lambda}) \cdot S/E_{\rm C,min} \tag{5.4}$$

where $V_{\rm C}\cdot S$ is the attractive (Casimir) part of the pair potential, and $E_{\rm C,min}$ is the value of the attractive part of $E_{\rm min}=V_{\rm pair}(r_{\rm min},S=1)$ which is the minimum of the pair potential

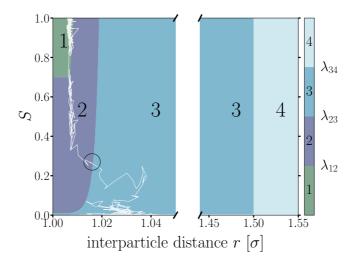


Figure 5.6: Contour map of the bond breakage reaction coordinate $\lambda(r, S)$. An example trajectory of a breaking bond is shown with the white solid line for which its bond breakage mechanism is measured when crossing λ_{23} as highlighted by the black circle. The four states strongly bound (1), weakly bound (2), free diffusion (3), and fully broken (4) as defined in Table 5.1.

(see Eq. 5.1), with $r_{\rm min}$ the corresponding interparticle distance. The distance parameter $r_{\lambda} = \max(r, r_{\rm min})$ to prevent the λ -boundaries to lie in the repulsive part of the potential. See Table 5.1 for the criteria that define the four regions.

λ	region	energy	distance
1	strongly bound	$E_{\lambda} \leq 0.70$	
2	weakly bound	$0.70 < E_{\lambda} \le 0.01$	
3	diffusive	$E_{\lambda} > 0.01$	
4	truly broken		$r_{\lambda} > 1.50\sigma$

Table 5.1: The energy (E_{λ} in Eq. 5.4) and distance criteria defining the four region as depicted in Fig. 5.6.

We used the label λ as a (fictitious) order parameter that determines whether a configuration is inside a certain region, and, more importantly, when crossing a boundary between these regions. We denote the boundary (a.k.a. as an interface) between region i and j as λ_{ij} . Initiated from the strongly bound region 1, trajectories can only escape via region 2 and 3 to finally reach region 4, crossing the interface λ_{34} , after which the bond is considered truly broken and the simulation is halted. This strict condition is necessary, as even after escaping the attractive well and entering region 3, the particles diffuse around and actually have a significant chance of rebinding. Counting trajectories that enter region 3 as being broken thus would severely underestimate the lifetime. However, since the time to diffuse from the particles from the λ_{23} - to the λ_{34} -interface is very dependent on the location of λ_{34} , the bond lifetime τ itself is measured as the last timestamp the trajectory crossed the λ_{23} -interface.

The lifetime of the bond is strongly related to the rate constant for the breaking process. Considering bond-breaking as a two state dissociation process, we can express the corresponding rate as the inverse of the bonds' lifetime (a.k.a. residence time) $k_{\rm break} = 1/\tau$. An alternative

way to compute the rate constant for breakage is to compute the flux for trajectories starting in the strongly bound state to escape: [137]

$$k_{\text{break}} = \Phi_{\lambda_{12}} P(\lambda_{23} | \lambda_{12}) P_{\text{sep}} \tag{5.5}$$

where $\Phi_{\lambda_{12}}$ is the (effective positive) flux though the λ_{12} -interface, $P(\lambda_{23}|\lambda_{12})$ is the conditional probability of escaping the potential well, i.e. reaching λ_{23} , given that the system comes from region 1, and $P_{\rm sep}$ is the probability the particles successfully separate, i.e. reaching λ_{34} . Respectively, they are defined as:

$$\Phi_{\lambda_{12}} = \frac{N_{\lambda_{12}}}{\tau_{\text{sim}}} \tag{5.6}$$

$$P(\lambda_{23}|\lambda_{12}) = \frac{N_{1\to 3}}{N_{\lambda_{12}}}$$
 (5.7)

$$P_{\rm sep} = \frac{N_{2\to 4}}{N_{1\to 3}} \tag{5.8}$$

where $\tau_{\rm sim}$ is the duration of the simulation, $N_{\lambda_{12}}$ the number of positive crossings through the λ_{12} interface, i.e. from region 1 toward 2, and $N_{1\rightarrow 3}(N_{2\rightarrow 4})$ is the number of times region 3(4) is reached given that you came from 1(2), or, in other words, the number of first crossings of $\lambda_{23}(\lambda_{34})$ subsequent to $\lambda_{12}(\lambda_{23})$. One can quickly verify that the breakage rate is then $k_{\rm break}=N_{2\rightarrow 4}/\tau_{\rm sim}\equiv 1/\tau$, as expected. (see Ref. [137] for a discussion)

Measuring the quantities in Eq. 5.5-5.8 per bond provides microscopic insight into the influence of activation on the breakage dynamics. The first stage of bond breakage, i.e. escaping the potential well, is defined by $\Phi_{\rm esc}=\Phi_{\lambda_{12}}P(\lambda_{23}|\lambda_{12})$ which expresses the rate at which the particles escape their potential well. The second stage of bond breakage, i.e. successfully separating the particles to $r=1.5\sigma$, is expressed as the probability $P_{\rm sep}$. Separating the reaction coordinate into two stages helps to identify the role of activity as stage I is mainly defined by the shape and depth of the pair potential and buckling of the bond, and stage II by for example the position of the bond in the structure or crowding effects by other particles.

As patchy particles have rotational and translational degrees of freedom, one can characterize the mechanism of breaking a critical Casimir induced bond between two particles as a combination a two qualitatively different limiting cases. Figure 5.7 schematically illustrates the two breakage mechanisms along the (r,S)-reaction coordinate: 1) a pure radial mechanism, where particles move away from each other along the bond vector, keeps the particles' patches aligned and S=1. And 2) a purely rotational, angular mechanism in which particles rotate along each other perpendicular to the bond vector, until the overlap area between the patches is vanishing, makes S=0. In practice, both routes are available to the particles and the breakage mechanism is naturally a combination of these limiting routes. Accordingly, we can follow the breakage mechanism along the value of S as it can distinguish between radial (S=1) or angular (S=0) trajectories.

For analyzing the breakage mechanism, we again use the separation of the two stages of breakage. In the first stage, the system escapes the potential well and reaches the λ_{23} -interface for the first time at a particular S-value, which we denote $S_{\rm mech}$. These $S_{\rm mech}$ -values are counted as

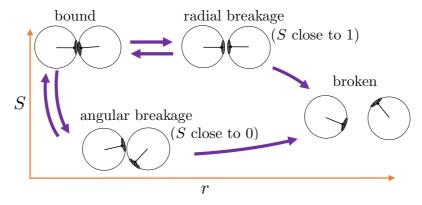


Figure 5.7: Two distinct breakage mechanisms illustrated along the (r, S)-reaction coordinate. Starting from the bound state (top left corner), the bond breaks via the radial mechanism keeping the patches aligned (S-value close to 1), or via the angular mechanism where the patches rotate away (S-value close to 0). Both routes may lead to the broken state or rebind back into the bound state.

 $n_{1 \to 3}(S_{\mathrm{mech}})$ which' probability distribution is given by Eq. 5.9. Note that the counts $N_{i \to j}$ from Eq. 5.7-5.8 equal the sum over all S_{mech} -values as $N_{i \to j} = \sum_S n_{i \to j}(S)$. Continuing the simulation, the trajectory either rebinds, adding a count to $n_{3 \to 1}(S_{\mathrm{mech}})$, or breaks, adding a count to $n_{2 \to 4}(S_{\mathrm{mech}})$. Then, noting that $n_{1 \to 3}(S) = n_{2 \to 4}(S) + n_{3 \to 1}(S)$, the probability of breaking at given S is written in Eq. 5.10. Only upon true breakage, the last $n_{2 \to 4}(S_{\mathrm{mech}})$ is counted and normalized as the breakage mechanism P_{mech} in Eq. 5.11. One can see that the breakage mechanism also follows from $P_{\mathrm{mech}}(S) = P_{1 \to 3}(S)P_{2 \to 4}(S)P_{\mathrm{sep}}^{-1}$ where P_{sep}^{-1} is the normalization.

$$P_{1\to 3}(S) = \frac{n_{1\to 3}(S)}{N_{1\to 3}} \tag{5.9}$$

$$P_{2\to 4}(S) = \frac{n_{2\to 4}(S)}{n_{1\to 3}(S)} \tag{5.10}$$

$$P_{\text{mech}}(S) = \frac{n_{2\to 4}(S)}{N_{2\to 4}} \tag{5.11}$$

By only considering the values of S at λ_{23} under the condition the system came from region 1, λ_{23} -recrossing events are filtered out of the breakage mechanism analysis. Recrossing events, as observed for the example trajectory in Fig. 5.6 where the trajectory recrosses λ_{23} at $S\approx 0.1$ after escaping the well at $S\approx 0.3$, are mainly determined by free diffusion and do not contain information on how the system escaped the potential well.

Many of the observables, e.g. the bond lifetime, show an exponential decay over time. Therefore, we report averages with a 95% confidence interval of the mean calculated using block averaging. As the start configurations are equilibrated before the measurements start, and the breakage itself is a rare event, all breakage events are uncorrelated and we take blocks of minimal 100 simulations. [231, 232]

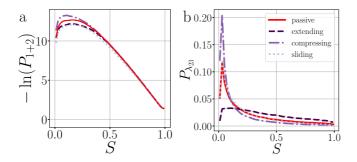


Figure 5.8: Exploring the potential well of passive and active dimers at dT=0.12K. The probability histogram of S (Eq. 5.2) of a passive dimer (red solid line) and active dimers with $F_{\rm A}$ =100 $k_{\rm B}T/\sigma$ and force directions: extending, compressing, and sliding. The measurements are taken in (a) the full bonding volume, i.e. region 1 + 2, and (b) when crossing (positively and negatively) the λ_{23} -interface. There are 50 bins for $S\in[0.0,1.0]$. As the λ_{23} -interface has minimally a value of S=0.01 (at $E_{\lambda}=0.01$), the first bin in (b) is approximately twice as low as the second bin.

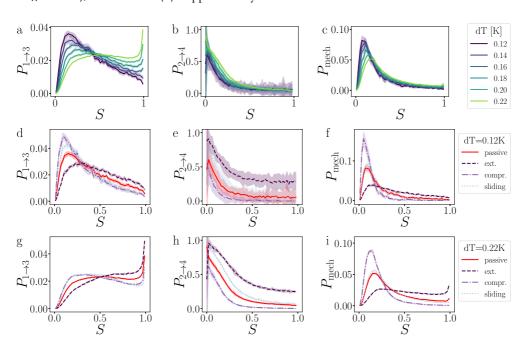


Figure 5.9: Analysis of the breakage mechanism of the dimers by $P_{1\rightarrow3}$, $P_{2\rightarrow4}$, and $P_{\rm mech}$ from Eq. 5.9-5.11, respectively. (a-c) Passive dimers at dT=0.12-0.22 K. (d-i) Active dimers at dT=0.12 (d-f) and 0.22K (g-i) with extending, compressing, and sliding active forces at $F_{\rm A}$ =100 $k_{\rm B}T/\sigma$. Each row shows it legend on the right.

5.3 Results and Discussion

In this section, we present and discuss the numerical simulations. We start with the simplest colloidal architectures in section 5.3.1 and 5.3.2: the dimers and decamers. We performed 1000 brute force BMD simulations at various attraction depths, tuned by the critical Casimir interac-



Figure 5.10: For a configuration at λ_{23} , its probability to rebind depends on the overlap between the bonding volume (purple region between patches), and the positional density distribution (orange halo around the particles) which' probability is amplified in the direction of the active force(orange arrow). This is a schematic representation and not based on simulations. [233] See Fig. 5.9 for measured $P_{2\rightarrow4}(S)=1-P_{\rm rebind}(S)$ at the various force directions.

tion via the temperature dT. The activity is tuned by the force magnitude F_A and direction (see Methods and Fig. 5.2).

In section 5.3.3, we increase the complexity of the architectures toward rings, and evaluate the influence on strained and relaxed rings of different sizes. Here we include the gravitational field to mimic the experimental setup.

5.3.1 Dimer

Before the bond breaks, activity naturally affects the exploration of phase space and we show this effect with probability histograms in Fig. 5.8. Measurements are taken at each timestep during BMD simulations in a volume or isosurface of interest. For the effect on the bond orientation of the dimer, we measure S inside the bonding volume , i.e. region 1 and 2, at which the bond is intact (Fig. 5.8a) and we observe that activity does not significantly buckle the bond as the histogram of S of passive and active dimers overlap.

The histogram shown in Fig. 5.8b shows the distribution of the S-values at crossing the λ_{23} -interface positively and negatively. In equilibrium, this histogram, if taken as $-\ln(P)$, represents the free energy in units of k_BT and we observe that bonds mostly sample values with $\theta>0^\circ$. Each particle in the bond can rotate around the interparticle vector to maintain $S'(\theta)$ and r at a constant value (Fig. 5.4), resulting in a bonding volume proportional to $\sin\theta$. Such behavior leads to an entropic contribution to the free energy, and configurations with $\theta>0^\circ$ are found to be more prevalent.

Activity has a specifically large effect where the gradient of the potential is comparable or smaller than the active force, such as when crossing λ_{23} (Fig. 5.8b). Under extending forces, the probability density shift to higher S-values compared to the passive case. This has two reasons: First, the particles start out in the strongly bound region 1 where S is close to one and activity pulls the particles apart keeping S high. Second, recrossing λ_{23} at low S-values will be suppressed for extending forces as they direct away from the λ_{23} -interface. Both arguments are indirectly measured using $P_{1\to 3}$ and $P_{2\to 4}$ next. Conversely, under compressing forces, the active forces' direction is reversed and thus more density is observed at low S-values.

Breakage Mechanism. Figure 5.9 presents the probability distributions $P_{1\to 3}(S)$, $P_{2\to 4}(S)$ and $P_{\rm mech}(S)$ (Eq. 5.9-5.11) for passive and active dimers. For the passive case, the attraction strength is varied between dT=0.12-0.22K. For the active case, the active force magnitude is set to F_A =100 $k_{\rm B}T/\sigma$ and the dimers experience extending, compressing and sliding force directions at dT=0.12 and 0.22K

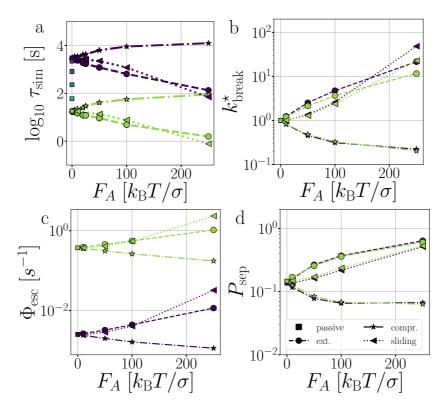


Figure 5.11: Passive and active dimers. (a) The measured average bond lifetime $\tau_{\rm sim}$ in the passive case at dT=0.12-0.22K and in the active cases at dT=0.12 and 0.22. The scaled rate constant $k_{\rm break}^{\star}$ (b), stage I ($\Phi_{\rm esc}$) (c), and stage II ($P_{\rm sep}$) (d) at dT=0.12 and 0.22K and F_A =10, 50, 100, and 250 $k_{\rm B}T/\sigma$. The color coding indicates the dT, similar to Fig. 5.5, and the line coding is shown in figure on the right.

Starting with the passive case, Fig. 5.9a shows that to reach λ_{23} , the patches rotate significantly more in the strong attraction potential ($dT=0.12\mathrm{K}$) compared to the weak attraction potential ($dT=0.22\mathrm{K}$). At the same time, the conditional probability to break $P_{2\to4}(S)$ peaks around $S\approx0$, i.e. the patches are rotated away, decreases quickly, and plateaus at a low value for S>0.5 (Fig. 5.9b). The peak at low S is reduced for stronger attraction. Since $P_{1\to3}(S)$ and $P_{2\to4}(S)$ show opposing trends, the effect of dT on the breaking mechanism is reduced (Fig. 5.9c). Nevertheless, the majority of bond breakage events clearly occur via the angular mechanisms. The maximum of $P_{\mathrm{mech}}(S)$ shifts from $S_{\mathrm{max}}\approx0.2$ to $S_{\mathrm{max}}\approx0.1$ with increasing attraction strength.

Although the translational and rotational diffusion constants have no influence on equilibrium distributions, they do play a critical role in bond breakage dynamics as demonstrated in Refs. [146] and [234]. Hence, the introduction of active particles that experience directional enhanced translation is expected to significantly impact the breakage mechanism. As hypothesized above, when using extending forces, $P_{1\rightarrow 3}(S)$ shows a shift toward high S-values (Fig. 5.9d,g), indicating radial breakage, as the active force pulls the particles from high S in region 1 toward the λ_{23} -interface. Subsequently, the probability of successfully separating the particles increases for all values of S (Fig. 5.9e,h), as extending forces are directed away from the bonding volume

(see Fig. 5.10 for a schematic illustration). The breakage mechanism probability distribution in Fig. 5.9f,i shows that for extending forces both angular and radial routes are likely, with only a small bias toward smaller S, i.e. angular breakage. In contrast, for compressing forces, $P_{1\to 3}(S)$ shows a shift toward lower S-values, indicating angular breakage, with respect to the passive case. Moreover, the corresponding $P_{2\to 4}(S)$ indicates that configurations with S>0.5 are completely blocked from particle separation as the compressing active force restores the particles back into the bound state (Fig. 5.10). The breakage mechanism probability distribution $P_{\rm mech}(S)$ shows now a significant shift toward lower S-values indicating that all bonds must break via the angular route. Finally, sliding forces result in a distribution $P_{1\to 3}$ similar to that of compressing forces. Thus, one would expect also a shift of $P_{\rm mech}(S)$ toward and angular breakage. However, the probability to separate $P_{2\to 4}(S)$ is relatively (compared to passive case) more affected for S>0.5. This results in the sliding forces showing a breakage mechanism probability $P_{\rm mech}(S)$ similar to the passive dimers, even if the two stages of breakage are very different from passive breakage.

This analysis clearly indicates that the breakage mechanism of dimers is strongly affected by the separation probability $P_{2\rightarrow4}$, both in the passive or active case, and at strong or weak interaction strength.

Bond Lifetime. Fig. 5.11a-d presents, respectively, the measured bond lifetimes in the simulation τ_{sim} , the ratio of the active and passive rate constants k^*_{break} , the flux out of the potential well (stage I) Φ_{esc} , and the separation probability P_{sep} of stage II. Naturally, in the passive case, the bond lifetimes τ_{sim} depend strongly on dT, as a shallower potential leads to exponentially faster breakage (Fig. 5.11a) [235, 236]. Under the influence of activity, τ_{sim} can either be enhanced or suppressed depending on the direction of the applied force.

As expected, only stage I of breakage (Fig. 5.11c), i.e. the rate of escaping the potential well, depends on the potential depth as determined by dT. Compressing and extending forces, respectively, exponentially decrease and increase the rate constant of stage I proportional to the magnitude of $F_{\rm A}$. Because in the dimer the particles are bound with directed patches, forming a relatively stiff bond, and which maintain the active forces at a $\pm 180^\circ$ angle, the effect of activity inside the potential well of the dimer resembles an equilibrium problem in an effective tilted potential along the direction of r [237]. This effect can be qualitatively captured with an Arrhenius type expression

$$k_{\text{tilt}}(F_A) = \nu e^{-\beta V(r) + \beta \alpha F_A \Delta r}$$
 (5.12)

with $\alpha=-1,1$ for compressing and extending forces, respectively, and Δr the distance from the potential minimum to the barrier location. As this distance is roughly $\Delta r \approx 0.007\sigma$, the expected increase/decrease is roughly a factor of 2 for $F_A=100$, in agreement with the observation (see Fig. 5.11c). Note that this analysis does not hold for sliding force case where the force direction is not aligned with the interparticle distance vector.

The effect of activity on stage II of breakage, i.e. successful particle separation, was qualitatively explained using Fig. 5.10 and quantitatively measured in Fig. 5.9. Figure 5.11d confirms that extending and sliding forces enhance the probability of separation $P_{\rm sep}$, while compression reduces it. Additionally, $P_{\rm sep}$ does not show a potential depth dependency.

Considering that activity can be viewed as an effective tilt on the potential, and $P_{\rm sep}$ is dT independent, the contribution of the potential depth can be separated from the activity by dividing the breakage rate constant $k_{\rm break}$ by the rate constant at zero activity, as shown in

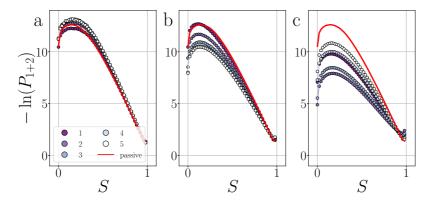


Figure 5.12: Deformations in decamers at dT=0.12K. The probability histogram of S (Eqn. 5.2) of a passive chain (red solid line) and active chain with $F_{\rm A}=100~k_{\rm B}T/\sigma$ (dots) and the force directions: extending (a), compressing (b), and sliding (c). The measurement is taken at region 1 and 2. The colored dots indicate the reduced bond number as shown in the legend.

Fig. 5.11b as k_{break}^{\star} . Consequently, for the active dimer, activity with the same magnitude and direction have an equivalent effect on the breakage rate.

5.3.2 Decamer

In contrast to a dimer, a longer chain can transmit stresses resulting from active forces exerted on its outer particles through the other bonds in the chain (Fig. 5.2). Although the breakage mechanism of the bonds in decamers remains qualitatively similar to that of dimers (see Fig. 5.18 in Appendix 5.5.1), activity has a significant impact on the dynamics and conformational distributions of the chain, leading to opposing effects in bond lifetime compared to a dimer. [221]

Before any bond has broken, activity already affects the bond distributions, causing the chain to buckle or straighten.[238] Fig. 5.12 shows the probability's distribution of S for each bond in a passive chain and active chains with $F_{\rm A}=100~k_{\rm B}T/\sigma$ at dT=0.12K. In the freely moving passive chain, all nine bonds are statistically identical, in line with Boltzmann's equipartition theorem, and appear as a single (red) curve.

Passive Chain. Although the bonds are energetically identical, both breakage stages show an enhancement at the passive chain's end, leading to bond 1 breaking twice as likely compared to the bonds in the center, as the breakage rate constant of bond 1 is approximately twice as high as those of bond 2-5 (see Fig. 5.13e). The breakage profile of passive semi-flexible chains has been shown to depend on the non-linearity (i.e. anharmonicity) of the interaction potential, stiffness of the chain, and ratio between bending relaxation times and bond lifetime. [239–243] The critical Casimir patchy particle chains, that have a persistence length between 250-150 particles for dT=0.12-0.22K (see Fig. 11 in Ref. [182]), are relatively stiff and thus show end-of-chain breakage.

Extending forces. When applying extending forces to the decamer, the chain straightens, rendering lower S-values less likely (as can be observed in Fig. 5.12a). Simultaneously, the bonds at the center (bonds 2-5) are more stabilized compared to bonds at the end (bond 1), evidenced by the probability distribution of the bond energy $-\ln P(E_{\rm pair})$ (see Fig. 5.19 in Appendix 5.5.1). This stabilization impacts stage I of breakage with F_A =100, and to a lesser extent with

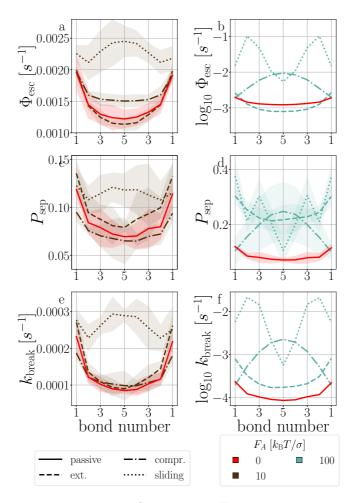


Figure 5.13: Passive and active decamer at dT=0.12 K with $F_{\rm A}$ =10 (left) and 100 (right) $k_{\rm B}T/\sigma$. Stage I $\Phi_{\rm esc}$ (a,b), stage II $P_{\rm sep}$ (c,d), and breakage rate $k_{\rm break}$ (e,f) per bond. Color and line coding in the legends at the bottom.

 $F_A = 10$: bond 2 to 5 diffuse slower out of the well compared to the passive chain as shown in Fig. 5.13a and b, respectively.

The stabilization of the chain and lowering of the rate of stage I would predict an increased lifetime. However, Fig. 5.14 indicates $\tau_{\rm sim}$ exponentially decreases with the extending force magnitude F_A . It is the increase of stage II probability $P_{\rm sep}$, that is tripled when $F_A=100$, that is primarily responsible for the decrease in the decamer's lifetime (Fig. 5.13c,d). [244] The increase of the stage II probability is bond number independent, leaving the breakage profile in Fig. 5.13e,f largely unaffected compared to the passive decamer.

Compressing and Sliding Forces. Under compressing and sliding forces, the chain primarily buckles around the center and the second bond, respectively, as the distributions of S in Fig. 5.12b,c indicate.[245] The buckling leads to a strong destabilization of the chain, which in turn increases the rate of stage I at high activity (see Fig. 5.13b). At low activity (Fig. 5.13a), the effect on stage I is not as strong. The particle separation probability (stage II) is less severely

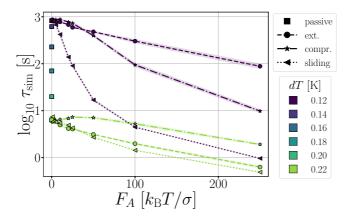


Figure 5.14: The $\tau_{\rm sim}$ of passive decamers (dT=0.12-0.22K) and active decamers (dT=0.12, and 0.22K) with extending, compressing, and sliding forces.

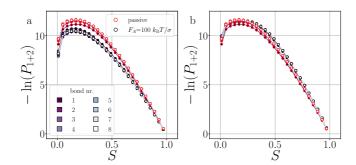


Figure 5.15: Deformations in T6D15 at dT=0.16K. The probability histogram of S (Eqn. 5.2) of a passive and active rings with $F_{\rm A}=100~k_{\rm B}T/\sigma$ and the force directions: inward (a), and outward (b). The measurement is taken in region 1 + 2. The inner color of the dots indicate the position of the bond, and the edgecolor the passive (red) or active ring (black).

impacted compared to stage I (Fig. 5.13a-d). Thus, the lowering of the (free) energy barrier of stage I is the main driving force of breakage and largely explains the breakage rate profile in Fig. 5.13e,f.

Weak interaction strength. When the attraction strength is weak (dT=0.22K), the architecture is not able to adjust its shape and mediate the effect of activity. These systems break fast and often near the active force. Data not shown.

5.3.3 Ring structures

Complex networks or gels, in contrast to freely moving chains, can contain tension even when energy minimized at zero temperature. The simplest architecture for which such tension can occur, is a ring structures. In our assessment, we consider two types of rings: those with tension, composed of four TPP particles, and those without tension, composed of six TPP particles (see Fig. 5.3). Additionally, we vary the length of the DP-chain from 5 to 15 particles, which can mediate the tension within the rings. We set the critical Casimir temperature to $dT=0.16~{\rm K}$,

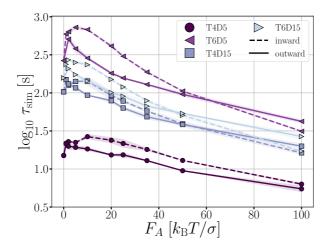


Figure 5.16: The ring structures' lifetime $\tau_{\rm sim}$ at dT=0.16K.

striking a balance between ensuring a reasonable simulation length until breakage and allowing the structures to remain intact long enough to observe the effects of activity on the deformations in the architectures.

The average bond lifetime of the rings is presented in Fig. 5.16. As anticipated, the presence of tension reduces the lifetime of the structures, and larger number of bonds leads breakage. The lifetimes $\tau_{\rm sim}$ of the structures follow the order T4D5 \ll T4D15 < T6D15 < T6D5. For all structures and both directions of active forces, the lifetime of the rings initially increases with increasing active force, but eventually decreases.

We use the T6D15 structure for an in-depth analysis of how the deformations (Fig. 5.15) and breakage rate are affected by the active forces (Fig. 5.17). This structure does not suffer from the misalignment of the TPP-DP bond nor from a limited number of bonds that can mediate the activity.

Passive Rings. While each bond is energetically equal, not all bonds are conformationally equal. The filled red circles in Fig. 5.15 indicate the TPP-DP bond (bond 1) in the ring visits lower values of *S* compared to bond 2-8 (Fig. 5.15). The rate constant of stage I around bond 1, as well as stage II, are enhanced, making it the most preferred breakage position (Fig. 5.17).

Inward-Facing Forces. Under inward-facing forces, the dipatch particle chains buckle, as follows from the strong shift of the black curves in Fig. 5.15a) toward lower S values. Remarkably, the buckling is distributed evenly over the bonds. The uniform buckling makes all bonds more prone to escape the potential well (see Fig. 5.17a). Stage II is affected differently, depending the magnitude of force (Fig. 5.17c). At low force ($F_A = 10$), only bond 1 is blocked from particle separation, similar to what is observed in the decamer under compressing forces. Figure 5.17e shows this blocking leads to a flat breakage rate (and profile). At high force ($F_A = 100$), due to a leverage effect of the activity, the bonds close to the active force (bond 1-4) shows enhancement of particle separation, while bond 5-8 are suppressed. Overall it leads to enhanced breakage close to the focal point of the active force.

Outward-Facing Forces. Under outward-facing forces, the dipatch particle chains show a minor stabilization by evenly straightening the bonds, as indicated by the shift of the black curves to higher S values in Fig. 5.15b). Both large and small forces marginally suppress the first stage, the

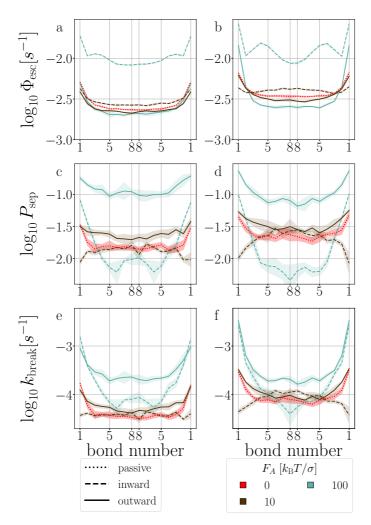


Figure 5.17: Stage I (a,b), stage II (c,d), and breakage rate (e,f) per bond of T6D15 (a,c,e), and of T4D15 (b,d,f).

potential escape (see Fig. 5.17a), but have a more significant effect on the stage II, the probability $P_{\rm sep}$. All bonds show enhanced probability of particle separation proportional to the force magnitude (Fig. 5.17c). For outward-facing forces, the second stage of bond breakage results in an enhancement of the breakage rate that is flat at small active force and is more pronounced at bonds close to the center of activity (i.e, low bond number) at large force.

Tension. Next, we will compare the T4D15 and T6D15 structures to identify the role of the misaligned TPP-DP bond on the response of activity using Fig. 5.17.

In the passive case and at low activity, we observe that the tension is evenly distributed over all bonds as T6D15 and T4D15 show the same shape of stage I and stage II versus bond number. However, T4D15 is faster in both stages.

At high activity, in the first stage with outward-facing forces, all bonds in T6D15 straighten and strengthen, while for T4D15, the straightening of the chain between the active particles

expose the misalignment of the TPP-DP bond making it prone to break shown in Fig. 5.17b where $\Phi_{\rm esc}$ at bond 1-2 is higher and bond 3-8 and lower than the passive case. [246] Both structures shows similar increased stage II throughout all the bonds. Using inward-facing forces, bond 1, and 4 to 6 are faster in stage 1 in T4D15. However, in both structures, $P_{\rm sep}$ (stage II) of bond 4-8 is below 1% and the differences of stage I cannot be observed in the breakage rate $k_{\rm break}$. Thus, for both force directions, the largest difference is observed at bond 1, which indeed is the misaligned TPP-DP bond.

5.4 Conclusions

In this work we have given microscopic insight into the effect of activity, modeled as active patchy Brownian particles connected to various patchy particle architectures: dimers, decamers, and rings. To do so, we separated the contribution on the two stages of breakage: the rate of escaping the pair potential well (stage I) and the probability of successful particle separation (stage II). We unraveled the observed behavior in the bond breakage rate, breakage mechanism, and breakage profile and identify at which stage the influence of activity dominates.

Table 5.2 summarizes the effects of small and large active forces on dimers and decamers with $F_{\rm A}$ directions: extending, compressing and sliding.

For the dimers, the effect of activity on the first stage of bond breakage resembles an equilibrium problem in an effective tilted potential along the direction of r, and the second stage of bond breakage was potential depth independent. Therefore, the effect of activity on the bonds' lifetime is roughly a function of the magnitude and direction of the active force only. When active forces point toward or away from the bonding volume, the bond life time τ increases or decreases, respectively.

The dimers and decamers showed qualitatively similar breakage mechanisms in both passive and active systems. Under extending (compressing) forces, the mechanism shifted to a radial (angular) route which is explained by the direction of the active force pointing away (toward) from the bonding volume. The sliding mechanism lies in between these two extremes.

The active decamers showed under all force directions and magnitudes reduced or comparable lifetimes compared to passive decamers. Extending forces straighten the chain, energetically stabilize the bonds, and suppress the rate constant of stage I. However, the chains still show an exponentially decaying lifetime proportional to the magnitude of the active force because simultaneously stage II is enhanced. For sliding and large compressing forces, the chains buckle and weaken their bonds leading to breakage peaked around the highest curvature in the chain. The weakened bond strength (stage I) dominates in explaining the effect of activity on the decreased lifetimes. However, at small compressing forces, stage II is suppressed at the ends of the chain and balances the effect of stage I. The active chain then shows an approximately equal breakage rate compared to passive chains.

All ring structures, with and without tension, show an initial stabilization of the structures upon small active forces ($F_{\rm A}=10$). The initial stabilization of the structure is caused by a minor suppression of stage I. Subsequently, for inward-facing forces, we observe an significant suppression of stage II in bonds close to the active force leading to a strong enhancement of the lifetime τ . However, for the outward-facing forces, the opposite is observed. The minor stabiliza-

bonds halfway the middle. breakage location is given as: edge: bonds close to the end of the chain, flat: uniform distribution, center: bonds in the middle of the chains, and w-shape: increase (orange \Uparrow), increase (yellow \uparrow), approximately equal (gray -), and decrease (blue \downarrow) with respect to the passive case. For the decamer and rings, the Table 5.2 : Summarizing table for the breakage behavior of the dimer, decamer and rings as function of active force magnitude and direction. Dimer at dT=0.12K, mechanism: S (angular) r (radial). The breakage rate and breakage stages are qualitatively compared to $F_{\rm A}=0$ using arrows for: strong

Rings					Decamer		Dimer								
$k_{ m break}$	$P_{ m sep}$ stage II	$\Phi_{ m esc}$ stage ${ m I}$	breakage location	$F_{ m A} ightarrow$		$k_{ m break}$	$P_{ m sep}$ stage II	$\Phi_{ m esc}$ stage I	breakage location	$k_{ m break}$	$P_{ m sep}$ stage II	$\Phi_{ m esc}$ stage ${ m I}$	breakage mechanism	$F_{ m A} ightarrow$	
			edge	0					edge				S	0	
1	\rightarrow	←	edge	10	ou:	1	\rightarrow	←	edge	\rightarrow	\rightarrow	\rightarrow	S	10	exte
\rightarrow	\Rightarrow	\leftarrow	edge	100	outward	\rightarrow	\rightarrow	\leftarrow	edge	\rightarrow	\rightarrow	\rightarrow	S & r	100	extending
←	←	ı	flat/center	10	inward	1	←	\rightarrow	edge	←	←	←	\mathcal{S}	10	compressing
\rightarrow	←	\Rightarrow	edge	100	ď	\rightarrow	\rightarrow	\Rightarrow	center	←	←	←	S	100	sing
						\Rightarrow	\rightarrow	\Rightarrow	flat	\rightarrow	\rightarrow	\rightarrow	S	10	S
						\Rightarrow	\rightarrow	\Rightarrow	w-shape	\rightarrow	\rightarrow	\rightarrow	S	100	sliding

tion of stage I is followed by a minor enhancement of stage II leading to lifetimes approximately equal to the passive case.

At larger activity ($F_{\rm A}=100$), the bond lifetime τ has reduced significantly and converges for both directions of the forces to the same value. Additionally, this case shows most breakage near the active force at bond 1. However, the two directions of the force each target a different breakage stage. Inward facing forces induce buckling in the ring and weaken all bonds. Stage I shows an overall enhancement, but stage II is only enhanced at bonds close to the active force and suppressed at the bond in the center. Outward-facing forces show very little effect on the conformations of the ring as well as on stage I; it is stage II that has the largest effect on the breakage rate.

Lastly, we looked at the effect of the misaligned bond (bond 1) in the T4D15 structure compared to T6D15. At low activity and in the passive case, the tension caused by the misalignment can be distributed over all bonds. The lifetime of T4D14 is lower than T6D15, but there is no enhanced reactivity in bond 1; only at large forces, we observe differences. Outward- and inward-facing forces expose the weakness of bond 1 and enhances stage I of bond 1 significantly. Simultaneously, as observed in T6D15, the second stage at bond 4 to 8 is very low . Effectively, both directions of the force leads to enhanced breakage at the misaligned bond via stage I.

We can draw some general conclusions from our findings, summarized in Table 5.2. First of all, the preferred breakage mechanism is in all cases via an angular mechanism. This might at first seem surprising, since it seems only natural that a bond breaks along the radial axis. However, the entropic contribution of larger angles is substantially enlarged to counteract this, and most bonds will break at low S value, i.e. via the angular mechanism.

Second, it is a well-known fact that breakage is a combination of an activated well escape stage, and a diffusive separation stage. When applying an active force most of the time both stages will respond qualitatively identically: for the dimer extending and sliding force will enhance breakage rate, while compression will suppress it. For the decamer and the rings things are different: the extending/outward forces surprisingly lower the escape probability due to stiffening of the chain. However, the final result is still that breakage is enhanced, as the separation stage compensates. In contrast, sliding is significantly enhancing chain breakage. Compressing forces are most complex, they enhance stage I but decrease stage II. The contrasting effect of forces occurring in ring structure: inward force first stabilize rings, before they enhance breakage at higher forces.

It is clear that activity can both enhance and suppress breakage rates and mechanisms, depending on the precise magnitude and direction. We expect therefore that activity also will have a large effect on the dynamical behavior of network formation in colloidal patchy particle systems.

Our findings will thus be important for designing adaptive and responsive active physical gels, and rationalising their behavior. In addition, if one wants to control breakage – and formation – of bonds one might target the different stages of breakage using activity. In a future study, we will report on how colloid gels self-assembled from patchy particle mixtures respond to activity.

The predictions made in this work can be experimentally tested by using particle systems that behave according to the potential used here [182]. Using microscopy the breaking behavior can be followed and tracked, see e.g. Ref [139] and [55].

While our predictions were made specifically for critical Casimir interactions, we believe that they can be generalized to a large class of patchy interaction potentials, that are qualitatively similar: strong short range attractions induced by a relatively small patch in combination with ABP dynamics. As long as the rotational and translational diffusion constants behave similarly

to those of the colloids we consider here, and the ABP model applies to the self-propulsion mechanism, the resulting breakage dynamics should be qualitatively similar, irrespective of the origin of the attraction and the self-propulsion.

5.5 Appendix

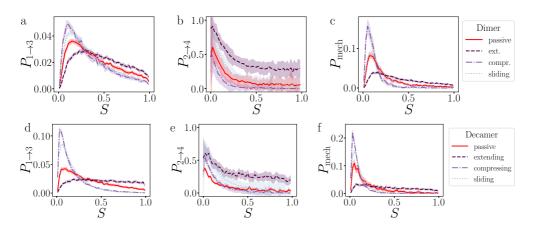


Figure 5.18: Analysis of the breakage mechanism by $P_{1\rightarrow3}$, $P_{2\rightarrow4}$, and $P_{\rm mech}$ from Eq. 5.9-5.11, respectively. Dimers (a-c) and decamers (d-f) with dT=0.12K and active force directions with extending, compressing, and sliding active forces at $F_{\rm A}$ =100 $k_{\rm B}T/\sigma$. Note that breakage mechanism and both stages are in principle bond number dependent, but here we take the average over the whole chain.

5.5.1 Decamers' Breakage Mechanism

Figure 5.18 presents the $P_{1\to 3}$, $P_{2\to 4}$, and $P_{\rm mech}$ of passive and active dimers and decamers at dT=0.12K and F_A =100 $k_{\rm B}T/\sigma$.

Stage I of breakage in a decamer is affected by the shape of the chain. As shown in Fig. 5.12 by the distribution of S per bond, and in Fig. 5.19 the distribution of $E_{\rm pair}$, under activity the decamer changes its shape. This shape change: straightening under extending forces, and buckling under compressing and sliding forces is reflected in the $P_{1\to 3}$ of Fig. 5.18d as a shift toward high and low S meaning radial and angular breakage, respectively.

Figure 5.18b,e show that the effect of activity on probability of successful particles separation in the decamer is lower than in the dimer, especially at S<0.5. The particles in the chains are not freely diffusing in region 3, as they may be still bound to their neighbours. This effect is explicitly measured in Fig. 5.13c, that shows that the ends of the chain separate twice as successful compared to the center.

Comparing the breakage mechanism of the dimer and decamer (Fig. 5.18c,f), we observe qualitative similarities. The passive case it is practically similar, the active case shows an exaggeration of the shift in breakage mechanism. Extending forces: no preferred breakage route, and compressing and sliding forces: angular breakage.

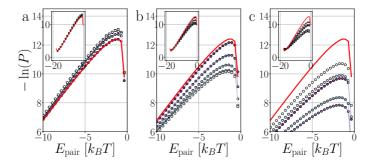


Figure 5.19 : Passive and active decamers. The probability histogram of $E_{\rm pair}$ (Eqn. 5.1) of a passive chain (red solid line) and active chain with $F_{\rm A}=100~k_{\rm B}T/\sigma$ (dots) and the force directions: extending (a), compressing (b), and sliding (c). Due to symmetry, only the first to fifth bond are shown with symbols as depicted with the colored dots in the legend of Fig. 5.12. The inset shows a zoom out of the distributions. The measurement is taken at $E_{\rm pair}<0~k_{\rm B}T$.

5.5.2 Fluctuations

To be able to understand the response of the ring structures to the introduction of activity, we can analyse their dynamical fluctuations using Principle Component Analysis (PCA). [247] We perform PCA on long straightforward Brownian dynamics simulation trajectories of rings using the MDAnalysis software package[248, 249]. We focus on the ring system with 4 TPP and 15 DP particles (T4D15), as this system contains long chains that allow significant buckling, but is smaller than the 6 TPP structures and thus decorrelates significantly faster.

We start with the analysis of the influence of active forces on the fluctuation dynamics and deformations of an elastic ring using Principal Component Analysis (PCA), as depicted in Fig. 5.20 and reported Table 5.3. To enhance the likelihood of observing intact structures during the fluctuation and deformation simulations, we set the interaction strength to $dT=0.12~\rm K$.

We conducted Principal Component Analysis (PCA) on long trajectories, with all simulations lasting at least 30,000 seconds. However, for an inward-directed active force $F_{\rm A}=15$, the simulation duration was reduced to 5,000 seconds due to observed buckling and a high probability of breaking.

The eigenvectors corresponding to the two dominant modes, which account for approximately 80% of the variance, are depicted in Fig. 5.20, and their respective eigenvalues are listed in Table 5.3. These dominant modes are particularly prevalent since they correspond to the lowest curvature in the semi-flexible polymers, resulting in minimal energy cost.

For small outward-directed forces up to $F_{\rm A} \leq 25$ and inward-directed forces up to $F_{\rm A} \leq 5$, no significant deformations were observed, and the contribution to the variance was not notably different from the passive case. Any observed differences between the systems can be attributed to limited sampling.

Conversely, larger inward-facing active forces ($F_{\rm A} \geq 15$) caused the DP-particle chains to buckle, as evidenced by the average positions of these trajectories (Fig. 5.20b). The buckling is caused by the movement of the first mode (Fig. 5.20d) which indeed shows a significantly higher contribution compared to the passive case (Table 5.3) [55]. In this deformed structure, the two dominant modes still exist, albeit with different amplitudes.

Table 5.3: The contributions to the variance of the first two modes (shown in Fig. 5.20) retrieved via PCA. Column wise the magnitude and direction of the active force, the loading of the variance of mode 1 and 2 and their sum are shown. * In the trajectory of inward-facing $F_{\rm A}$ =15 forces, buckling and breaking was observed.

 $F_{\rm A} \left[k_{\rm B} T / \sigma \right]$ direction magnitude mode 1 mode 2 sum 0.55 0.26 0.81 0 2 0.59 0.25 0.84 in 5 in 0.56 0.310.87 15* 0.78 0.11 0.89 in 2 0.27 0.82 0.55 out 5 0.49 0.28 0.77 out 15 out 0.50 0.25 0.75 25 0.20 0.470.67 out

Since the active force, whether inward or outward, primarily affects the radial part of the potential through the translational displacement of particles, it is not expected to have a substantial impact on the fluctuation spectrum. The fluctuations primarily depend on the bending rigidity, as defined by the shape of the S'-function. Moreover, the active force is fixed to the particles and constrained by two bonds. Consequently, the active force cannot reorient along fluctuation modes to drive them, as observed in the actuated elastic solid in Ref. [250].

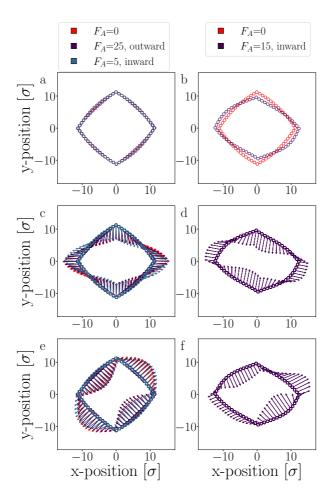


Figure 5.20: PCA: The particles' average position(a,b), and the two dominating fluctuation modes: first mode (c,d), and second mode (e,f) of passive and activated T4D15 rings. For clarity, the eigenvectors of the two fluctuation modes are illustrated with 10x magnified arrows for clarity. Each column has its legend shown at the top.

6 ACTIVATION OF COLLOIDAL PATCHY PARTICLE NETWORKS

Active matter systems contain components that consume energy to generate motion, leading to various collective behaviors observable in both biological and synthetic realms. These systems differ from equilibrium systems where interactions are typically due to interparticle forces or thermal fluctuations. In particular, active matter can display unique behaviors such as flocking, clustering, and motility-induced phase separation. A notable type of active matter is active physical gels, which are observed in biological systems such as the cytoskeleton in muscle and plant tissues; these gels are vital for processes such as cell motility and tissue repair. This study addresses the behavior of physical gels, specifically patchy colloidal gels composed of divalent and trigonal planar patchy colloidal particles interacting via the critical Casimir force [182], aiming to deepen our understanding of their activity-driven dynamics. The trigonal planar particles, that make up the nodes of the network, have been made active as Active Brownian Particles and exert forces into the colloidal network. Upon increasing activity, three distinct global structures are observed: a homogeneous, an inhomogeneous, and phase separated structure. The first structural transition is initiated at low (high) active force magnitude in combination with strong (weak) attractive patchy potentials. The subsequent transition arises when the network is broken and active particles push the passive particles into a high-density regions. These structural responses are intimately related to the system's bond probability that may increase or decrease as function of active force magnitude and direction, and attractive potential depth affecting both the rate of bond formation and breakage.

6.1 Introduction

Active matter consists of individual components consuming energy to produce motion, resulting in collective behaviors [251]. Such self-driven systems are evident across multiple length scales, ranging from biological phenomena such as the motility and morphogenesis of cells [103] and bird swarms, to synthetic systems such as colloidal Janus particles and colloidal rollers [122, 133, 252–254]. Active particles with different shapes [129, 130], repulsive potentials [255, 256], including attractive potentials [128, 253], alignment [257], or with different velocities [132], and mixtures of passive and active particles [130, 258–261] have demonstrated a diverse phase behavior and dynamics. This includes altering the position of phase transitions and introducing entirely new dynamical phases. Being distinct from equilibrium systems, where dynamics arise from interparticle forces or thermal fluctuations, active matter is intrinsically out of equilibrium. Their unique dynamics can lead to such as flocking motion [257], clustering [262], and motility-induced phase separation (MIPS) where active particles segregate into distinct regions [263, 264].

An intriguing class of active matter is active physical gels, exemplified by the cytoskeleton found in muscle and plant tissues. These gels are characterized by their viscoelastic properties and inherent activity, resulting in distinct non-equilibrium behavior [104, 105]. Central to the cytoskeleton's function is the actin protein, which can polymerize, forming varied structures such as the crosslinked and branched networks seen in the cell cortex and lamellipodium [103]. The mechanical properties of actin, combined with its dynamic assembly and disassembly in conjunction with the molecular motor myosin, enable it to function as the cell's biological springs. This gives actin a pivotal role in processes such as cell motility, replication, growth, and tissue repair [213, 214].

Patchy particles, that are colloidal particles characterized by their distinct attractive binding sites or "patches", facilitate the self-assembly of complex colloidal architectures such as chains, rings, and networks [38, 53, 54, 57, 138]. The colloidal networks can be constructed by mixing patchy particles of different valencies (see Fig. 6.1), with an average valency beyond two, and can be viewed as a physical gel, characterized by reversible bond formation and adaptive character. Patchy colloidal gels create *open* architectures that achieve equilibrium [93, 94], contrasting with non-equilibrium gels made of isotropically interacting particles [265]. This distinction is for example evident in their spatially uniform dynamics [266]. Utilizing colloidal patchy particles as a model system, we aim to unlock a deeper understanding of the behavior of physical gels under activity.

For that, we employ the critical Casimir model developed and explored in the previous chapters. The structure of this paper is as follows: In the subsequent section, we detail the patchy particle model, elaborating on its interaction potential, simulation specifics, and analysis techniques. In the Results section, we explore the phase behavior of activated colloidal patchy particle networks. We observe that the connectivity (or bond probability) of the architecture that influences phase behavior displays non-monotonic trends, correlating with the attractive strength of patchy particles and the magnitude and direction of active forces. To elucidate this behavior, we discuss the effects of activity on bond formation and dissociation rates, which together dictate the bond probability. We end with conclusion and perspectives on future research.

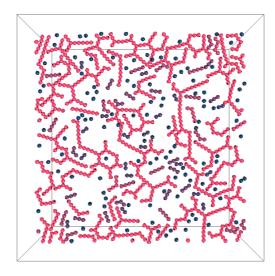


Figure 6.1: An example of a colloidal network composed of trigonal planar and dipatch particles in a ratio of 30:70 percent with a color coding indicates its cluster size N_c , ranging from 1 (dark blue) to >4 (bright pink). The density $\rho=0.382N/\sigma^2$ and the patchy pair potential is strong (dT=0.12K).

6.2 Methods

6.2.1 Model

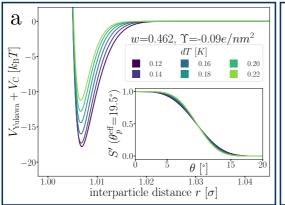
Recent progress in colloid chemistry has made it possible to synthesize micrometer-sized particles that feature patches with distinct surface properties differing from the main body of the particles [63]. Suspending such patchy particles in a near-critical binary liquid mixture (e.g. water and lutidine), attractive directed bonds, i.e., only one bond per patch, are induced between the patches on the surface of neighboring particles via a solvent mediated critical Casimir force [72, 182]. While patchy particles experience thermal motion and adhere to Boltzmann statistics, they can be directly observed using techniques such as confocal microscopy [57]. Thus, they can be regarded as mesoscopic analogs of atoms [92] and can act as an experimental model system to explore complex self-assembled colloidal architectures analogous to their molecular counterparts [38, 53, 54, 57, 138].

Interaction potential

As explained in the previous chapters, the anisotropic pair interaction between two patchy particle, i and j, with orientations Ω_i and Ω_j , respectively, and interparticle distance r_{ij} is described by

$$V_{\text{pair}}(r_{ij}, \Omega_i, \Omega_j) = V_{\text{Yukawa}}(r_{ij}) + V_{\text{C}}(r_{ij})S(\Omega_i, \Omega_j), \tag{6.1}$$

Here, V_{Yukawa} signifies an isotropic repulsion, while the second term represents the directed patch-patch attraction between the particles i and j. It is important to note that we assume each particle pair can form only a singular bond. Given the relatively limited range and width of the



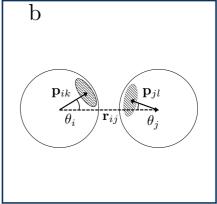


Figure 6.2: (a) The patchy particle radial potential for dipatch particles composed of Yukawa repulsion $V_{\rm Yukawa}$ (Eq. 3.2) and critical Casimir attraction $V_{\rm C}$ (Eq. 3.6). The inset shows the switching functions S' that are additionally a function of dT. (b) A schematic illustration of the inter-particle vector ${\bf r}$ (dotted arrow), patch vectors ${\bf p}$ on each particle (solid arrows), and the angles θ .

patchy critical Casimir interaction, this condition is readily met in our systems, ensuring that only one combination of patches results in an effective attraction.

The patch interactions' anisotropy is captured by the two switching functions $S'(\theta)$. While these functions, in principle, depend on the orientations Ω of both particles, they are simplified to depend solely on the angles θ associated with each particle. The function is represented as:

$$S(\Omega_i, \Omega_j) = \max_{1 \le k, l < n_p} S'(\theta_{ik}) S'(\theta_{jl})$$
(6.2)

where k and l run over the n_p patches of each particle. The angle θ is the angle between the patch vector and the interparticle vector as depicted in Fig. 6.2b.

Figure 6.2a presents the optimized patchy particle potential that is capable of reproducing the experimental system of dipatch particles. The specific functional forms of the Yukawa electrostatic repulsion, critical Casimir attraction, and the switching functions S', can be found in Chapter 3 and Ref. [182].

Active Janus particles, when subjected to an AC field, exhibit a propelling motion and hover over the capillary surface[122]. Hence, beyond the gravitational potential (see Sec. 3.2.4 and 3.6.3), the external potential also incorporates an alignment potential. This alignment potential ensures that the active force is oriented in line with the wall's direction.

$$V_{\text{align}}(\hat{e}_{A,z}) = \frac{1}{2} \epsilon_{\text{align}} \arcsin^2(\hat{e}_{A,z})$$
(6.3)

where $\hat{e}_{\mathrm{A},z}$ signifies the z-component of the active force direction as described in Sec. 2.4. The prefactor $\epsilon_{\mathrm{align}} = 500\,k_{\mathrm{B}}T$ was chosen such that a lift-off of the particle against the gravitational field did not occur.

The alignment of the active force of the TPP particle will additionally causes one patch to always direct along the quasi-2D plane which is the patch in the direction or opposite of direction of the active force for type I and II, respectively. In quasi-2D systems, patches orientated along

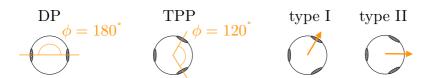


Figure 6.3: Illustrations of particle architectures. The divalent patchy (DP) particle exhibits a 180° angle between its patches, whereas the trigonal planar patchy (TPP) particle displays a 120° angle. There are two varieties of active TPP particles: one where the active force (depicted by the orange arrow) points toward one patch (type I) and the other where it lies between two patches (type II).

the quasi-2D plane show an enhanced reactivity compared to patches facing the wall as shown in previous work in Chapter 4 and Ref. [267]. Therefore, in active systems, the reactivity of active TPP particles will be influenced by both their enhanced diffusion and the alignment. While in a passive system there would in principle no *active* alignment, we have opted to include it. In the limit of $F_A \to 0$, the dynamics of the active systems approaches the dynamics of the passive system and any observed distinctions between passive and active systems are attributable exclusively to active propulsion effects.

The total potential energy of the system is the sum of all patchy particle pair interactions, and the external potential $V_{\rm ext}(z,\hat{e}_A)$. The latter includes both the active force alignment potential (Eq. 6.3) and the gravitational potential (Eq. 3.14):

$$V = \sum_{i < j}^{N} V_{\text{pair}}(r_{ij}, \Omega_i, \Omega_j) + \sum_{i}^{N} V_{\text{ext}}(z_i, \hat{e}_{A,i})$$

$$(6.4)$$

where i and j run over the N colloidal particles, and z is the vertical distance to the wall, and \hat{e}_A is the unit vector of the direction of the active force.

6.2.2 Simulation Details

PATCHY PARTICLE ARCHITECTURES

In this chapter, we investigate self-assembled networks composed of colloidal dipatch (DP) and trigonal planar patchy (TPP) particles. As depicted in Fig. 6.3, DP particles have two attractive patches at opposite sites, while TPP particles possess three patches arranged in a planar configuration with a 120° angle between them. The DP particles are allowed form bonds with both DP and TPP particles, but the TPP particles are restricted to only bind with DP particles. This is to prevent the TPP particles to cluster and form small rings or honeycomb lattices [59]. In this way, the (active) TPP particles are distributed throughout the architectures and activate the passive DP chains.

Networks are constructed by mixing 70% DP and 30% TPP particles of in total N=1000 or 500 patchy particles in a cubic simulation box of length 51.17 or 36.18 σ with periodic boundary conditions, respectively. The strong attractive systems at dT=0.12 K contains 1000 particles, while the others comprise 500 particles. The resulting quasi-2D system has an area coverage of roughly η =30% or density ρ =0.382 N/σ^2 . This combination of density and ratio of DP:TPP

particles was chosen as it resulted in a highly connected network at the strongest attraction strength at passive conditions.

Monte Carlo

See Sec. 2.3, for a detailed description of Monte Carlo and the explanation of single particle and cluster moves that are performed to self-assemble a colloidal network.

EQUATIONS OF MOTION

See Sec. 2.4, for a detailed description of the equations of motion of (active) Brownian particles. The translational and rotational diffusion constant are set to $D_{\rm T}$ =0.0034 $\sigma^2/{\rm s}$, $D_{\rm R}$ =0.05 rad $^2/{\rm s}$, as experimentally measured for dipatch particles with diameter $\sigma=3.2\mu m$ [54,56].

6.2.3 Analysis

We perform long straightforward molecular dynamics simulations on three independent samples and after reaching a steady state, i.e. when the bond probability does not drift over time, measurements are taken from the self-assembled architectures.

The static observables include: bond probability $P_{\rm b}=N_{\rm p,bound}/N_{\rm p,tot}$, which is the number of bound sites $N_{\rm p,bound}$ divided by the total number of sites $N_{\rm p,tot}$. The cluster size distribution, $P_j=\frac{n_j}{\sum_i n_i}$, where n_j is the number of clusters of size n, and $\sum_i n_i$ is the total number of clusters. The bond occupancy of TPP particles, which is the distribution of the number of bonds the TPP particles make. Finally, the local density distribution $\rho_{\rm L}$ is measured by drawing a square grid (with a grid size of approximately $26\sigma^2$) and counting the number of particles in each grid cell.

The bonding of two patches can be seen as a (chemical) reaction in which the patch transitions from an unbound to a bound state:

unbound
$$\stackrel{\mathrm{K}}{\rightleftharpoons}$$
 bound, $\mathrm{K} = \frac{\rho_{\mathrm{b}}}{\rho_{\mathrm{u}}} = \frac{k_{\mathrm{bu}}}{k_{\mathrm{ub}}}$ (6.5)

where K is the bonding reaction constant, while $\rho_{\rm b}$ and $\rho_{\rm u}$ are the density of bound and unbound (free) patches, respectively. The $k_{\rm ub}$ and $k_{\rm bu}$ are the binding and unbinding rate constant, respectively. The bound state is defined when a patch has an attractive interaction with another patch, i.e. their attractive part of the pair potential $V_{\rm C} \cdot S < 0$ (Eq. 3.6). A breakage event is detected if two particles have separated more than half a diameter 0.5 σ , which indicates the transition to the unbound state. Note that $k_{\rm ub}$ and $k_{\rm bu}$ do not refer to a single breakage or binding mechanism but, instead, contain many possible breakage rates depending on colloidal architecture and breakage location as observed in Chapter 5.

From the brute force simulations, the state of each patch is monitored and the survival probability $P_{\rm S}$, i.e. the probability that patch did not change state, as function of time t is then recorded. Assuming that binding and unbinding times are exponentially distributed processes

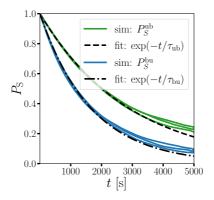


Figure 6.4: The survival probability of the bound and unbound state of the patches as measured in brute force simulations at dT=0.12 K, F_A =50 $k_{\rm B}T/\sigma$, and type II active particles. A fit of Eq. 6.6 measures the binding and unbinding rate $k_{
m ub}=1/ au_{
m ub}$ and $k_{
m bu}=1/ au_{
m bu}$, respectively. Solid colored lines are the measurements from three independent samples, and the black dotted lines are the fits.

and are independent events, dominated by a single timescale. The survival probability then follows the relation

$$P_{\rm S}(t) = \exp(-t/\tau) \tag{6.6}$$

where the binding and unbinding rates, $k=1/\tau$, are subsequently deduced through a fit. Fig. 6.4 shows an example of such a measurement and fit of the bound and unbound survival probability.

Instead of direct counting, an alternative way to measure the bond probability $P_{
m b}$ is via the rates $k_{\rm ub}$ and $k_{\rm bu}$:

$$P_{\rm b} = \frac{\rho_{\rm b}}{\rho_{\rm u} + \rho_{\rm b}}$$

$$= \frac{1}{k_{\rm ub}/k_{\rm bu} + 1}.$$
(6.7)

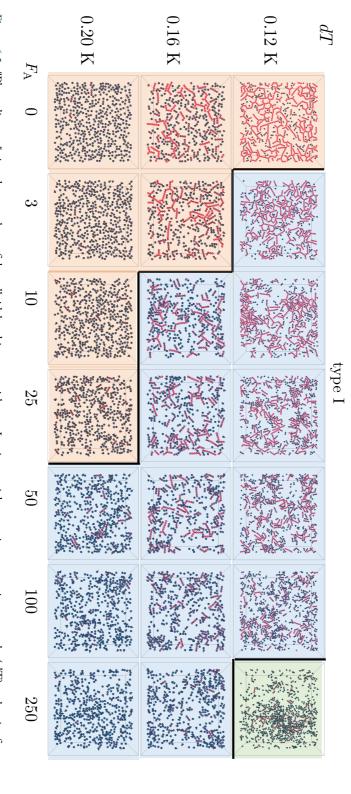
$$=\frac{1}{k_{\rm ub}/k_{\rm bu}+1}. (6.8)$$

Therefore, the changes observed in measure $P_{\rm b}$ will be explained by the effect of activity on $k_{\rm ub}$ and $k_{\rm bu}$.

6.3 Results

6.3.1 Phase Behavior

A mixture consisting of DP and TPP particles in a ratio of 70:30, respectively, initiated as a random fluid, form a network structure after an equilibration with $1 \times 10^7 N$ to $1 \times 10^6 N$ MC steps for the strongest to weakest interaction strength, respectively. Snapshots of the resulting structures can be seen in the left most column of Fig. 6.5. Upon increasing the bond attraction, a well-connected equilibrium colloidal network, or gel, forms where chains of DP particles are interconnected via nodes composed of TPP particles (top left snapshot in Fig. 6.5 and 6.6) [179].



separated densities that forms MIPS or a nematic regions (top right, green) architectures different global structure: homogeneous densities (bottom-left corner, red), a void forming, inhomogeneous densities (center, blue), and a magnitudes (F_A) . The color of the particles indicates its cluster size N_c , ranging from 1 (dark blue) to >4 (bright pink). The shaded colors represent Figure 6.5 : "Phase diagram" given by snapshots of the colloidal architecture with type I active particles at various attraction strengths (dT) and active force

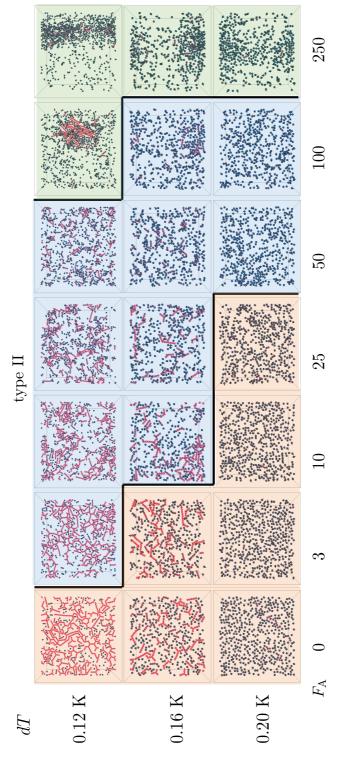


Figure 6.6: "Phase diagram" given by snapshot of the colloidal architecture with type II active particles at various attraction strengths (dT) and active force magnitudes (F_A) . The color of the particles indicates its cluster size N_c , ranging from 1 (dark blue) to >4 (bright pink). The shaded colors represent architectures global structure: homogeneous densities (bottom-left corner, red), a void forming, inhomogeneous densities (center, blue), and a separated densities that forms MIPS or a nematic regions (top right, green).

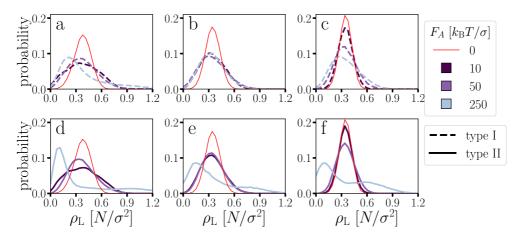


Figure 6.7 : The local density $\rho_{\rm L}$ at various active force magnitudes (F_A =0, 10, 50, and 100 $k_{\rm B}T/\sigma$) and both directions (top row: type I, bottom row: type II), and attraction strengths (from left to right column: dT=0.12, 0.16, 0.20 K).

Despite achieving thermodynamic equilibrium, we still observe an abundance of monomers. Previous work has indicated that this anomaly can be attributed to the gravitational confinement inherent in our experimental setup[267]. To follow the effect of activity on the phase behavior of the colloidal network, we conduct extensive Brownian Dynamics simulations (lasting more than 20,000 seconds of simulation time) for various active force magnitudes that reached steady state after approximately 10,000 seconds of simulation time. We observe structural changes of the architectures attributable to active propulsion effects, as depicted by the snapshots at the end of the runs in Fig. 6.5 and 6.6 for type I and II active particles, respectively.

In the low to moderate activity regime and with both directions of active fores, an inhomogeneous structure with more dense and a dilute regions compared to the passive case appears which is observed in the center (blue colored) systems in Fig. 6.5 and 6.6. What differentiates the inhomogeneous (blue) from the homogeneous (red) structures is the distribution of the local density ρ_L as depicted in Fig. 6.7. In the inhomogeneous structures, we observe values of local density, specifically at $\rho_L < 0.15$ and $\rho_L > 0.6$, that are not present in the passive systems. The onset of this inhomogeneous structure is almost immediate, i.e. for low F_A , for strong bonds (dT = 0.12K), starting at $F_A \geq 3~k_{\rm B}T/\sigma$. A snapshot of such a system was shown in the Introduction in Fig. 1.9a. However, as bond strengths weaken (dT > 0.12K), the threshold force magnitude for this phase shift toward inhomogeneity increases. Such immediate structural responses to activity are not observed for isotropically interacting particles, as they quickly form a non-equilibrium gel at low temperatures, arresting the dynamics of the system [128, 268, 269].

If the system is well-connected and active TPP are anchored to the architectures, low activity leads to better void formation compared to moderate activity. Compare, for example, at the snapshots at dT=0.12 K and F_A =10 and 50 $k_{\rm B}T/\sigma$ in Fig. 6.5 and 6.6, and their local density distribution in Fig. 6.7d. While activity initiates separation by persistently pushing the colloidal clusters together, it also leads to enhanced bond breakage. Smaller (active) clusters possess faster effective rotations and translations compared to large clusters [270, 271], leading to the dissolution of the high-density regions and homogenization of the systems' density.

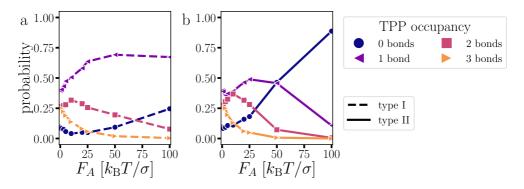


Figure 6.8: Bonding occupancy of the active TPP particle type I (a) and II (b) at dT =0.12 K.

When the passive DP particles exhibits limited connectivity with the active TPP particles, especially in combination with type II active particles, the systems resembles a system of passive particles immersed in an active bath [268, 269, 272]. At dT=0.20 K, activity initially has hardy any effect on the local density distribution. From $F_A \leq 50~k_{\rm B}T/\sigma$, we start observing void formation leading to a separated phase at F_A =250 $k_{\rm B}T/\sigma$. The separated phase is identified by the appearance of two peaks in ρ_L (Fig. 6.7). At dT=0.12 K, due to high activity from $F_A \geq 100~k_{\rm B}T/\sigma$, the colloidal network breaks down as type II TPP particles break their bonds, thereby losing their ability to function as nodes (Fig.6.8b). The passive DP particles are then pushed together to from high density regions; prompting them to aggregate into a nematic phase at F_A =100 $k_{\rm B}T/\sigma$ as seen in the green systems of Fig. 6.6. When increasing the activity further to F_A = 250 $k_{\rm B}T/\sigma$, the long nematic chains fragment into shorter chains. Nevertheless, the high-density phase remains. The strength of the interaction between DP particles influences when this phase separation occurs; stronger interactions lead to earlier separation as the patchy interaction prevents the particles from moving to less dense areas.

Despite the pronounced structural changes witnessed in the high activity regime, our primary interest lies in the intermediate, experimentally accessible, region (up to $F_A=50~k_{\rm B}T/\sigma$). In this regime, a significant portion of the network structure remains intact, albeit being influenced by activity.

6.3.2 Breaking and forming bonds

The structure of the colloidal network, which determines the phase behavior, is directly related to bond probability. We observe a non trivial behavior, either effectively reducing or increasing bond probability depending on bond strength, active force magnitude, and direction, as shown in Fig. 6.9a.

At F_A =0 $k_{\rm B}T/\sigma$, the measured binding rate $k_{\rm ub}$ is lower for systems with stronger attraction potentials due to fewer available patches, as seen in Fig.6.9c. This can be explained as follows: an alternative way to write the bonding reaction is:

$$2P \stackrel{\mathrm{K}}{\rightleftharpoons} P_2, \qquad \qquad \mathrm{K} = \frac{[P_2]}{[P]^2} = \frac{k_{\mathrm{on}}}{k_{\mathrm{off}}}$$
 (6.9)

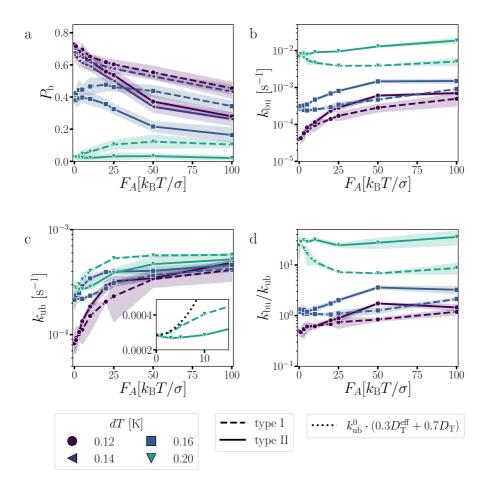


Figure 6.9 : The bond probability measured at steady state (a), the breaking (b) and binding (c) rate of the particles, and their ratio (d) at various active force magnitude and direction. Note that dT=0.14 K is not shown for clarity in b-d, as it is very similar to dT=0.12 K. The inset of (c) shows a zoom-in of $k_{\rm ub}$ at dT=0.20K and an effective binding rate (black dotted line) calculated by multiplying the measured passive binding rate $k_{\rm ub}^0$ with an effective diffusion $D_{\rm T}^{\rm eff} = D_{\rm T} + \frac{v_0^2}{2D_{\rm R}}$ and the normal diffusion $D_{\rm T}$ for the active TPP and DP, respectively. [133] The shaded area represents a 95% confidence interval of the error of the mean from three independent samples.

where two free patches P form a bond P_2 with its reaction constant K is defined by $k_{\rm on}$ and $k_{\rm off}$, the association and dissociation rate constants, respectively [234]. Both reaction equations in Eq. 6.5 and Eq. 6.9 describes the same process, and setting $\frac{[P_2]}{[P]} = \frac{\rho_{\rm b}}{\rho_{\rm u}}$ gives $k_{\rm ub} = [P]k_{\rm on}$. Thus, means that $k_{\rm ub}$ as defined in Eq. 6.5 is directly proportional to the density of free patches [P] in the system confirming the observed trend in Fig.6.9c.

Upon increasing activity, the binding rate constant $k_{\rm ub}$ rises with the active force magnitude for all studied systems. This increased binding rate is partially attributed to the activity enhanced diffusion of the TPP particles. To shed light on this underlying mechanism, consider the system at dT=0.20 K, predominantly comprising free (TPP) particles. In this context, we can approximate

the effect of enhanced diffusion on $k_{\rm ub}$ assuming that rates are proportional to the diffusion constant $k \propto D$ as written in the Smoluchowski diffusion-limited reaction rate constant [234, 273]. Given that the system has a 70:30 ratio of DP to TPP particles, the measured passive binding rate $k_{\rm ub}^0$ is multiplied by the factor $(0.3D_{\rm T}^{\rm eff}+0.7D_{\rm T})$ with $D_{\rm T}^{\rm eff}=D_{\rm T}+\frac{v_0^2}{2D_{\rm R}}$ and $v_0=\beta F_A D_{\rm T}$ [133]. In the system with type I activity, the approximation is qualitatively similar to the the measured $k_{\rm ub}$ at low activity as shown in the inset of Fig.6.9c by the black dotted line.

The breakage rate constant $k_{\rm bu}$ at F_A =0 $k_{\rm B}T/\sigma$ is directly related to the potential depth, set by dT; deeper attraction translates into slower breakage, as depicted in Fig. 6.9b. However, upon increasing activity, we observe non-monotonic behavior: at weak attraction strength, type I active particles show reduced breakage rate constants. In contrast, type II particles and those with stronger attraction strengths display an increase in these rate constants.

To delve deeper into this topic, one might revisit Chapter 5, which details the influence of activity on bond breakage rates. The main results are summarized here. When the active force induces buckling, it becomes the prime factor in amplifying the rate of bond breakage. This particularly impacts the first stage of bond breakage – the rate at which particles escape the potential well. The activation of the initial stage of bond breakage can lead to changes in the order of magnitudes different compared to passive cases. This is, for example, evident in applying sliding forces on the decamer, as shown in Fig. 5.13. For systems that do not buckle—such as compressed dimers, extended forces applied to a decamer, or forces directed outwardly in a ring structure—the orientation of the active force plays a decisive role. Depending on its direction, either toward or against the bonding volume, it can either suppression or enhancement the bond breakage rate, respectively.

In passive systems with strong attraction, the clusters are relatively large with long DP chains, visible in the cluster size distribution in Fig. 6.10, and most TPP particles are bound to the colloidal architectures as shown in Fig. 6.8a. Upon increasing activity in both directions to F_A =25 $k_{\rm B}T/\sigma$, forces are exerted on the colloidal architectures leading to the fragmentation of the clusters and a noticeable decline in triple-bound TPP particles. For type I, they mainly become double and single-bound states (Fig.6.8a). For the type II TPP particles, we observe that the majority shift to a monomeric state. Akin to what is observed in the lifetime of colloidal rings (Fig. 5.16), a maximum in double-bound TPP particles around F_A =10 $k_{\rm B}T/\sigma$ is observed (Fig.6.8b).

Moreover, alongside the TPP-DP bond breakages, DP-DP bonds also show susceptibility to increased activity as for example observed in decamers with sliding and extending forces captured in Fig. 5.14. The cluster size distribution at dT=0.12 K indeed immediately shows breaking into smaller clusters upon applying activity in both force directions (Fig. 6.10a).

At activity levels of $F_A=$ 50 $k_{\rm B}T/\sigma$, a clear distinction between type I and II particles is observed. Although the monomeric type II TPP particles are not anchored to any colloidal architecture structure (Fig.6.8b), their potential to catalyze bond breakage via collisions remains. Conversely, type I TPP particles predominantly exist in a singly-bound state (Fig. 6.8a), bonding with DP particles to form what we term an "active chain". By inspecting the snapshots, we can identify two variants of these active chains: those with one or with two active particles capping a DP chain. Both varieties exhibit enhanced stability due to activity, evident from the increased prevalence of small clusters (of size $N_c < 20$) under both weak and strong attraction potentials as function of F_A , as depicted in Fig. 6.10a and b.

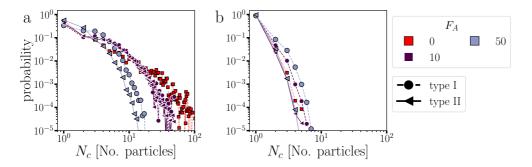


Figure 6.10 : Cluster size distributions at dT =0.12 (a), and 0.20 K (b). The magnitude of activity is F_A =0, 10, or 50 $k_{\rm B}T/\sigma$ and has directions as type I or II as indicated by the colors and symbols, respectively.

Can we understand why these active chains are stabilized? For chains featuring a single type I particle, the active force, aligned tangentially, reduces the likelihood of particle separation i.e. the second stage of bond breakage (see Chapter 5). Coupled with enhanced diffusion, the free patch at the other side of the chain becomes significantly more reactive yielding more short chains ($N_c < 20$). For chains with two active particles exerting a compressive force, our measurements indicated that a decamer breaks faster at dT=0.12, yet displays lifetimes analogous to passive scenarios at dT=0.22 K (see Fig. 5.14). For non-buckling chains, such as the dimers covered in Chapter 5 (see Fig. 5.11), or those made up of one or two DP particle paired with two TPP particles, compressing forces will extend their lifetime, again leading to enhanced stability for short chains.

6.4 Conclusions

In this study, extensive numerical Brownian simulations of have been carried out on colloidal networks representing active physical gels. The architectures, initially self-assembled by passive divalent colloidal patchy particles and trigonal planar patchy particles in a 70:30 ratio, are then activated by modeling the trigonal planar patchy particles as active Brownian particles. By modulating the magnitude and direction of the active force, we observe inhomogeneous-structure characterized formation of low density voids and high density clusters, showing a broadening of the local density distribution toward densities that are not observed in the passive systems. The inhomogeneous structures are observed at strong (weak) attraction strength of the patchy particles and small (large) active force magnitude at both directions of the force.

In systems characterized by strong binding where the majority of active particles are bound within the colloidal architectures, an increase in the active force magnitude results in effectively less bonds. Although, both rate of bond breakage, as well as rate of bond formation are enhanced, their ratio confirms the trend in observed reduced bond probability. Activity leads to fragmentation of the colloidal network, suppresses the formation of inhomogeneous structures. For the system at dT=0.12 K, there is an optimal active force magnitude of F_A =10 $k_{\rm B}T/\sigma$ at which a balance is struck: the architectures develop the inhomogeneous structure akin to phase separation but still retain a sufficient number of bonds to form a coherent network structure. As a result, this specific system displayed a broader local density distribution opposed to those at directly lower or higher activity levels.

In systems where bonding is sparse either due to weak patchy attractions or high activity in strong attractive systems, there is a noticeable difference between the two active force directions. Type I particles, which have the active force pointing in the direction of one patch, tend to bind with DP particles, forming small, stable chains though enhanced effective diffusion of the chains and a suppression of the second stage of bond breakage as in detail discussed in Chapter 5. Interestingly, the formation of small stable chains with type I active particles leads to an effective decrease of the breakage rate for the weakly attractive systems at dT=0.16 and 0.20 K compared to passive systems. In these active systems, we can observe a growth of bond probability as function of active force magnitude, something which is not observed for type II active particles.

At high active forces $F_A \geq 100~k_{\rm B}T/\sigma$, type II active particles that become monomeric and push the passive DP particles into high density regions form motility induced phase separation or, specifically at dT=0.12 K, a nematic phase. The type I active particles, forming the stable small chains, suppress the formation of this separated phase which is only observed at F_A =250 $k_{\rm B}T/\sigma$ and dT=0.12 K.

In summary, using accurate models for patchy particles, we predict an extremely rich behavior of colloidal architectures in response to activity. Depending on the attractive patchy potential, and magnitude and direction of the active force, the bond probability of the systems show can show an increase or decrease, which leads to the observation of a homogeneous, inhomogeneous, and separated structures. In the near future, experiments will test these predictions.

6.4.1 Future Outlook

For our next steps, a primary and straightforward suggestion is to simply consider larger systems with more particles. The phase behavior may be shifted or influenced by the constrained size of the current system. Additionally, we have not discussed any (global) relaxation pathways of bond breakage and formation.

A logical next step would be to change the density, or adjust the fraction of active particles. Colloidal gels formed from particles with limited valence, such as patchy particles, are known to form equilibrium gels that, at strong attraction/low temperature, form highly connected and percolated networks. With fewer active particles, the networks will form open structures might keep more bonds intact and initiates the inhomogeneous structure and separated phase at lower activity. Now, the latter phase may contain network architectures instead of only chain in the system in the current study.

Although we observed similarities in stable structures, notably the small active chains and double-bonded TPP particles under low activity as observed in Chapter 5, we did not examine the breakage dynamics, specifically the breakage location in the colloidal architectures in this study. Inhomogeneous breakage dynamics is in contrast to what is observed in passive equilibrium gels that shows spatially homogeneous dynamics [266].

Drawing inspiration from biology, active physical gels, which may not have a continuous energy injection by molecular motors gives the physical gels the opportunity to restructure their network in between external stimuli. The repair dynamics in a far-from-equilibrium state could offer valuable insights into the adaptability of the actin network within the cytoskeleton. Such insight can enhance our understanding of cellular resilience and functionality.

7 Summary

Materials possess properties and functionalities that arise from the collective organization of their constituent building blocks such as molecules or colloidal particles. Through non-covalent bonds such as hydrogen bonds or Van der Waals, Coulomb, and hydrophobic interactions, the building blocks self-assemble into architectures much larger than their individual sizes. Compared to the covalent bonds between atoms, these non-covalent bonds are weak. As a result, they often give rise to a soft and deformable rather than rigid character to a material. Many functions and structure in biological matter, think of the hydrogen bonding network between DNA basepair nucleotides, the stacked fatty chains and hydrophilic head groups forming the lipid bilayer of the cell membrane, or ligand-protein interactions, and the self-assembly of virus capsids are encoded by their non-covalent bonds. Understand such complex matter, that is inherently out of equilibrium in living organisms, remains a grand challenge.

In this thesis, we use patchy colloidal particles interacting via critical Casimir interactions that act as mesoscopic structural analogs of molecular, supramolecular and bio-inspired architectures. As such patchy particles can make directed bonds, i.e., only one bond per patch, they can be viewed as a coarse-grained, mesoscopic analog of (carbon) atoms. Due to their micrometer-sized scale, they are directly observable via confocal microscopy. Yet, they still experience thermal motion, ensuring their adherence to statistical behaviors intrinsic to molecules and atoms, such as the Boltzmann distribution. Hence, colloidal patchy particles are well suited as an experimental and computational model system to explore complex structures analogous to molecular, supramolecular or bio-inspired architectures. Incorporating actively propelled colloidal particles into the architectures, we can give insight into the structural behaviors of such materials in and out of equilibrium.

Chapter 2 gives an introduction to the basics of statistical mechanics and thermodynamics, focused on the canonical ensemble, describing phase behavior including coexistence and the Van der Waals equation. When interested in phase behavior of molecular or colloidal systems, one may resort to theory such as thermodynamic perturbation theory, including Wertheim Theory, that allows for predicting phase behavior. Or one resorts to computer simulations, for which two algorithms were explained: Monte Carlo, and Brownian molecular dynamics. We ended with a few measurement algorithms that were not explained in-depth in their respective chapters.

In Chapter 3, we developed an accurate patchy particle model for particles that interact via the critical Casimir force when immersed in off-critical binary liquids. The potential is based on theoretical critical Casimir potentials valid for isotropically interaction particles and the geometry of the patchy particle of interest. Through an integration over the patch geometry, three fitting parameters were used to benchmark the simulation outcomes onto experimentally measured chain length distributions and bending rigidities of colloidal semi-flexible polymers composes of divalent patchy particles in a series of varying attractive conditions. Such an accurate model

allows for microscopic structural and dynamical insight, and provide large-scale and long-time behavior when used in a multi-scale simulation, enabling the exploration of new hypotheses.

In Chapter 4, we extend Wertheim's theoretical framework for associating divalent particles under extreme confinement. Our inspiration stemmed from observing the influence of the gravity, which led colloidal particles to sediment with sub-diameter gravitational heights in both simulations and real-world experiments. We observed a significant presence of monomers that displayed reduced reactivity compared to larger chains, ascribed to the loss of rotational entropy experienced by monomers during bond formation. By factoring in this effect into the theory, we were able to predict the chain length distributions for a large range variety of potentials, from toy-models to our accurate critical Casimir potential, in excellent agreement with explicit Monte Carlo simulations. Given the accuracy of our predictions, we give insight into the influence of confinement and provide a quantitative explanation on how the persistence length of semi-flexible chains affects their reactivity under extreme confinement. Another advantage of the accurate predictions of chain length distributions, the procedure of optimizing potential parameters, as done in Chapter 3, can now be done in minutes instead of weeks.

In Chapter 5, we delve into the microscopic mechanisms behind bond breakage within colloidal patchy particle architectures, specifically under the influence of activity. We conduct a numerical investigation by introducing self-propelled colloids modeled as active Brownian particles into a self-assembling colloidal dispersion of dipatch and tripatch particles that form three archetypal substructures, namely, dimers, chains, and rings. We find a rich response behavior to the introduction of self-propelled particles, in which the activity can enhance as well as reduce the stability of the architecture, deform the intact structures and alter the mechanisms of fragmentation. We rationalize these finding in terms of the rate and mechanisms of breakage as function of the direction and magnitude of the active force by separating the bond breakage process into two stages: escaping the potential well and separation of the particles. Notably, when the active force induces buckling, it becomes the prime factor in amplifying the rate of bond breakage. This particularly impacts the first stage of bond breakage – the rate at which particles escape the potential well. For systems that do not buckle—such as compressed dimers, extended forces applied to a decamer, or forces directed outwardly in a ring structure—the orientation of the active force plays a decisive role. Depending on its direction, either toward or against the bonding volume, it can either suppression or enhancement the bond breakage rate, respectively.

In Chapter 6, we explore the responses of physical gels under the influence of activity. Active physical gels are an interesting type of active matter, which are observed in biological systems such as the cytoskeleton in muscle and plant tissues; these gels are vital for processes such as cell motility and tissue repair. For this, we use patchy colloidal gels composed of divalent and trigonal planar patchy colloidal particles interacting via the critical Casimir force as a model system. Similar as for the active colloidal molecules from Chapter 5, we find a rich response behavior when introduction of self-propelled particles in the colloidal networks leading to growth or fragmentation of clusters. In addition, we observe three distinct global structures upon increasing activity: a homogeneous, an inhomogeneous, and phase separated structure. The first structural transition is initiated at low (high) active force magnitude in combination with strong (weak) attractive patchy potentials. The subsequent transition arises when the network is broken and active particles push the passive particles into a high-density regions.

By building an accurate model that mimics the experimental conditions patchy colloidal particles immersed in a binary liquid interacting via critical Casimir forces gave a unique microscopic

insight into the dynamical and structural behavior of molecular and bio-inspired architectures in and out of equilibrium. Examples outside of this thesis are: the gravitationally confined self-assembly semi-flexible chains can act as a model system of confined polymerization of DNA, microtubules, or amyloids on membranes or under other confines spaces [53] which is a topic closely related to our Wertheim predictions that have shown the non-negligible effects of using *realistic* models for assembly under confinement. Additionally, our simulations could confirm noisy experimental measurements of colloidal molecules and showed that the conformation distribution of colloidal molecules, specifically colloidal cyclopentane, is influenced by the gravitational confinement [57].

8

Nederlandstalige samenvatting

Materialen kunnen eigenschappen en functionaliteiten bezitten die voortkomen uit de collectieve organisatie van hun samenstellende bouwstenen, zoals moleculen of colloïdale deeltjes. Via nietcovalente bindingen zoals waterstofbruggen of Van der Waals, Coulomb en hydrofobe interacties, assembleren de bouwstenen zichzelf tot structuren die vele malen groter kunnen zijn dan hun individuele afmetingen. In vergelijking met de covalente bindingen tussen atomen, zijn deze niet-covalente bindingen zwak. Als gevolg daarvan geven ze vaak een zacht en vervormbaar in plaats van een star karakter aan materialen. Veel structuren, en daarbij hun functies, in biologisch materiaal ontstaan vanuit niet-covalente bindingen, denk aan het waterstofbrugnetwerk tussen nucleotiden van DNA-basenparen, de gestapelde vetzuren en hydrofiele kopgroepen van de lipide dubbellaag van het celmembraan, of ligand-eiwit interacties, en de zelfassemblage van viruscapsiden. Het begrijpen van dergelijk complex materiaal, dat inherent uit evenwicht is in levende organismen, blijft een grote uitdaging.

In deze dissertatie gebruiken we colloïdale deeltjes met 'patches' die niet-covalente bindingen maken via kritische Casimir interacties en dienen als mesoscopische structurele analogen van moleculaire, supramoleculaire en bio-geïnspireerde architecturen. Aangezien dergelijke deeltjes via hun patches gerichte bindingen kunnen maken, d.w.z. slechts één binding per patch, kunnen ze worden beschouwd als een grofkorrelig, mesoscopisch analoog van (koolstof)atomen. Vanwege hun micrometergrootte zijn ze direct waarneembaar via bijvoorbeeld confocale microscopie. Toch ervaren ze nog steeds thermische beweging, wat zorgt voor hun naleving van statistische gedragingen die intrinsiek zijn aan moleculen en atomen, zoals de Boltzmann-distributie. Daarom zijn colloïdale patchy deeltjes geschikt als een experimenteel en computationeel modelsysteem om complexe structuren te verkennen die analoog zijn aan moleculaire, supramoleculaire of biogeïnspireerde architecturen. In combinatie met actief aangedreven colloïdale deeltjes geankerd aan de architecturen, krijgen we inzicht in de structurele gedragingen van dergelijke materialen in en uit evenwicht.

Hoofdstuk 2 geeft een inleiding van de basisprincipes van de statistische mechanica en thermodynamica, specifiek in het canonieke ensemble, waarbij het fasengedrag wordt beschreven, inclusief coëxistentie en de Van der Waals vergelijking. Wanneer men geïnteresseerd is in het fasengedrag van moleculaire of colloïdale systemen, kan men zich wenden tot theorieën zoals de thermodynamische perturbatietheorie, inclusief de Wertheim Theorie, die het voorspellen van fasengedrag mogelijk maakt. Of men wendt zich tot computersimulaties, waarvoor twee algoritmen werden uitgelegd: Monte Carlo en Brownse moleculaire dynamica. We eindigden met een paar meetalgoritmen die niet diepgaand werden uitgelegd in hun respectievelijke hoofdstukken.

In Hoofdstuk 3 hebben we een nauwkeurig model ontwikkeld voor colloïdale deeltjes met patches die interacteren via de kritische Casimir kracht wanneer ze zich in bijna-kritische binaire mengsels bevinden. Het potentiaal is gebaseerd op theoretische kritische Casimir potentialen geldig voor isotrope interacterende deeltjes en de geometrie van het colloïdale deeltje met patches.

Door middel van een integratie over de geometrie van de patch werden drie fitparameters gebruikt om de simulatie-uitkomsten te benchmarken op experimenteel gemeten ketenlengteverdelingen en flexibiliteit van colloïdale semi-flexibele polymeren samengesteld uit divalente patchy deeltjes in een reeks van sterk en zwak interacterende omstandigheden. Zo'n nauwkeurig model maakt microscopisch structureel en dynamisch inzicht mogelijk, en wanneer het wordt gebruikt in een multi-schaal simulatie biedt toegang tot grootschalig en langdurig gedrag, waardoor de verkenning van nieuwe hypothesen mogelijk wordt.

In Hoofdstuk 4 breiden we Wertheim's theoretische kader uit voor het associëren van divalente deeltjes onder extreme insluiting. Onze inspiratie kwam voort uit observaties van colloïdale deeltjes die zonken naar de bodem van een capillair tot sub-diameter hoogtes in zowel simulaties als echte experimenten door de zwaartekracht. We observeerden een overvloed van monomeren die een verminderde reactiviteit vertoonden in vergelijking met langere ketens, toegeschreven aan het verlies van rotatie-entropie ervaren door monomeren tijdens de vorming van bindingen. Door dit effect in de theorie mee te nemen, konden we de ketenlengteverdelingen voor een grote verscheidenheid aan potentieel voorspellen, van speelgoedmodellen tot ons nauwkeurige kritische Casimir model, in uitstekende overeenstemming met expliciete Monte Carlo-simulaties. Gezien de nauwkeurigheid van onze voorspellingen, geven we inzicht in de invloed van insluiting en bieden we een kwantitatieve verklaring voor hoe de flexibiliteit van semi-flexibele ketens hun reactiviteit beïnvloedt onder extreme insluiting. Een ander voordeel van de nauwkeurige voorspellingen van ketenlengteverdelingen is dat de procedure voor het optimaliseren van potentieelparameters, zoals gedaan in Hoofdstuk 3, nu in minuten in plaats van weken kan worden uitgevoerd.

In Hoofdstuk 5 duiken we in het breken van colloïdale patchy deeltjesarchitecturen, specifiek onder invloed van activiteit. We voeren een numeriek onderzoek uit door zelfaangedreven colloïden, gemodelleerd als actieve Brownse deeltjes, te introduceren in een zelfassemblerende colloïdale dispersie van dipatch- en tripatchdeeltjes die drie archetypische substructuren vormen, namelijk twee- en tien-deeltjes-lange-ketens en ringen. We vinden een rijk reactiegedrag op de introductie van zelfaangedreven deeltjes, waarbij de activiteit zowel de stabiliteit van de architectuur kan versterken als verminderen, de intacte structuren kan vervormen en de mechanismen van fragmentatie kan veranderen. We rationaliseren deze bevindingen in termen van de snelheid en mechanismen van breken als functie van de richting en grootte van de actieve kracht, door het proces van bindingbreuk in twee stadia te scheiden: ontsnappen uit de potentiaalput en scheiding van de deeltjes. Opvallend is dat wanneer de actieve kracht knikken veroorzaakt, het de belangrijkste factor wordt bij het versterken van de bindingbreuksnelheid. Dit heeft vooral invloed op het eerste stadium van bindingbreuk - de snelheid waarmee deeltjes de potentiaalput ontsnappen. Voor systemen die niet knikken - zoals gecomprimeerde dimeren, uitgerekkende krachten toegepast op een decameren, of naar buiten gerichte krachten in een ringstructuur speelt de oriëntatie van de actieve kracht een beslissende rol. Afhankelijk van de richting, naar of van het bindingsvolume af, kan het de snelheid van bindingbreuk respectievelijk onderdrukken of versterken.

In Hoofdstuk 6 verkennen we de reactie van fysische gels onder invloed van activiteit. Actieve fysische gels zijn een interessant type actieve materie, die wordt waargenomen in biologische systemen zoals het cytoskelet in spier- en plantenweefsels; deze gels zijn essentieel voor processen zoals celbeweeglijkheid en weefselherstel. Als modelsysteem hiervoor gebruiken we colloïdale gels bestaande uit divalente en trigonaal planaire *patchy* colloïdale deeltjes die interacteren via de

kritische Casimir kracht. Net als bij de actieve colloïdale moleculen uit Hoofdstuk 5, vinden we een rijk reactiegedrag bij de introductie van zelfaangedreven deeltjes in de colloïdale netwerken, wat leidt tot groei of fragmentatie van clusters. Bovendien observeren we drie verschillende globale structuren bij het introduceren van activiteit: een homogene, een inhomogene en een gescheiden structuur. De eerste structurele overgang wordt geïnitieerd bij lage (hoge) actieve krachtmagnitude in combinatie met sterke (zwakke) aantrekkingen tussen de colloidiale deeljes. De daaropvolgende overgang ontstaat wanneer het netwerk wordt verbroken en actieve deeltjes de passieve deeltjes naar hoogdichtheidsgebieden duwen.

Door het gebruik van een nauwkeurig patchy colloïdale deeltjes model dat experimentele waarnemingen kan voorspelling, geven we een uniek microscopisch inzicht in het dynamische en structurele gedrag van moleculaire en bio-geïnspireerde architecturen in en uit evenwicht. Voorbeelden buiten deze dissertatie zijn: de gravitationeel ingesloten zelfassemblage van semiflexibele ketens die dienen als een modelsysteem voor ingesloten polymerisatie van bijvoorbeeld DNA, microtubuli of amyloïden op membranen of onder andere ingesloten ruimtes [53]. Dit onderwerp is nauw verwant aan onze Wertheim voorspellingen die een niet te verwaarlozen effect hebben aangetoond van het gebruik van *realistische* modellen voor assemblage onder insluiting. Bovendien konden onze simulaties de experimentele metingen met ruis van colloïdale moleculen bevestigen en aantonen dat de conformatieverdelingen van colloïdale moleculen, specifiek colloïdaal cyclopentaan, worden beïnvloed door de gravitationele insluiting [57].

ACKNOWLEDGMENTS

After finishing my master degree and giving myself to time to think a bit about my future, I applied to the PhD position of Peter and Peter on using colloidal patchy particles to investigate active physical gels in a collaboration between experiment and simulations. I don't really know how I got the job, as I didn't know what patchy particles were, or active physical gels, and told them that "my life's dream was to have a farm to cuddle animals". Anyway, here I was.

First and foremost I would like to thank Peter Bolhuis as I am very grateful for a supervisor like you. Your door was always open and you listened to my ideas, gave me the confidence and freedom to try and test them, and gave me a push in the forward direction whenever I was stuck. From a scientific perspective, I am amazed by how you are able to still understand me when I couldn't express my thoughts clearly, and how you can boil complex matter down to its basics and expose its flaws or mistakes during group meetings. Especially knowing the variety of topics you work on: proteins, patchy particles, path sampling techniques, chemical reactions, and many more. From the perspective as a member of your group, I admire that you stick out for your group members and protect them if necessary. You always checked in during covid if things were still okay. It has been a pleasure to have you as my supervisor, I couldn't have wished for a better one.

The other Peter is Peter Schall. You are one of the kindest, warmest persons I have ever met in the scientific field. Thank you for your critical thinking and expertise during the colloid meetings. You are always able to elevate our research to a higher level.

The group of people I collaborated with most are the *colloid people*: Simon, thank you for taking me by the hand when I just started my PhD and felt like a noob all the time. Especially, your patience to explain me the critical Casimir force and hours of discussions on how to build the patchy particle model really helped me out. Piet, thank you for the hours of scientific and non-scientific discussions we had; your genuine interest in science is infectious. Nick, I always introduced you as my "experimental counterpart". Although covid took too much of our time working together, we still had the chance to go to a conference together in Crete. I am so happy we were able to do so. We found out we were not just an experimental/simulation match, but also really good friends.

Also of course the group members of Computational Chemistry. When I arrived there were Alberto, Yuliia, Verena, Ambuj, Nitish, Rakesh, Arjun, Johan, Sander and Becca. Thanks everybody for the Indian dinners and dances, and drinks on Fridays. Then, when I arrived again after covid there were Tamika (sorry for saying you name wrong for so long, and thanks for the daily online coffee breaks), Ferry, Bernadette, Florent, Gianmarco Gyorgy, Lingshu, Longijoa, Ashique, Alwan, Daria, Jacobus, Massimiliano, Rik, RV, Youri, Albert, Benjamin, and Suzanne. Of course also Evert Jan, Jocelyne, David, Bernd, and Ioana. A special thanks to Bernd who introduced me to computational chemistry and invested a lot of time in me to during my bachelor project. Without you I might have never chosen the direction of physical chemistry. I enjoyed everybody's company and I feel joy looking back on the great group dynamics we had. Somebody

once told me that you can change topic, but you cannot change people. I feel blessed I never wanted to.

Then a shout out to my students: Muriel, Hajo, Toon, Sayesha and Peiting. Muriel, you are one of the hardest working students I have met and I hope you are doing well. I really enjoyed our hours long Zoom calls. Hajo, you were my last student and a very bright one. You taught me many tricks in coding in c and smart algorithms. I admire your strength and I hope I was a listening ear for you. Toon, you were the student with the most perseverance and your eagerness to understand science is contagious. Sayesha and Peiting, although your stay was very short, I enjoyed your enthusiasm about a non-chemical topic which was probably not easy for you. For each of you, I hope that you learned a lot from your projects and a little bit from me too.

During the last months of my PhD, I visited the group of Mike Hagan in Boston. Special thanks to Sarvesh for helping me finding housing and picking me up on my first day at Brandeis. Anthony, for your patience to explain Optimal Control and helping me implement your code. Chris, for our many discussions on the train and inviting me to your home. Of course Saaransh, James, Layne, Danny, Smriti, Naren, Yingyou and Saptorshi. You guys were so kind throughout my stay. I hope you enjoyed the Sinterklaas sweets I brought. Let me know if you are ever in The Netherlands!

Marloes and Sanne, my chemistry friends dating all the way back from our bachelor. I vividly remember the first day at the university when I met you. I still have the blouse that I wore that day hanging in my closet; I cannot throw it away. It was the start of a strong friendship and I would have never guessed we would all do a PhD, especially how I sometimes felt as a total noob during our studies. But look at us now! On the day of my defense, we will celebrate our 12.5 years of friendship! A milestone which I am ever more proud of.

Lastly, I would like to thank Steven. It doesn't matter to me that you have no idea of what I am doing behind the computer, because whatever happens in life, wherever I am in the world, I can come home to you. Without your support, especially in the last phase of my PhD, I would not have made it. You make all my worries fade and make me instantly happy.

LIST OF PUBLICATIONS

As part of this thesis

Chapter 3: H.J. Jonas, S.G. Stuij, P. Schall & P.G. Bolhuis, A temperature-dependent critical Casimir patchy particle model benchmarked onto experiment, *J. Chem. Phys.*, 2021, **155**, 034902. doi: 10.1063/5.0055012

HJJ - Equal: 1, 3, 6, 5, 13, 14. Lead: 2, 9, 11, 12.

SGS -Support: 1, 6, 5, 11, 9, 14.

PS - Equal: 4, 6, 7. Support 1, 10, 14.

PGB - Equal: 1, 3, 4, 6, 5, 7, 13, 14. Lead: 10. Support: 9

Chapter 4: H.J. Jonas, P. Schall & P.G. Bolhuis, Extended Wertheim theory predicts the anomalous chain length distributions of divalent patchy particles under extreme confinement, *J. Chem. Phys.*, 2022, **157**, 094903. DOI: 10.1063/5.0098882

HJJ - Equal: 1, 3, 6, 5, 13, 14. Lead: 2, 9, 11, 12.

PS - Equal: 4, 7. Support: 10, 14.

PGB - Equal: 1, 3, 4, 6, 5, 7, 13, 14. Lead: 10.

Chapter 5: H.J. Jonas, P. Schall & P.G. Bolhuis, Activity affects the stability, deformation and breakage dynamics of colloidal architectures. *Under review at Soft Matter*

HJJ - Equal: 1, 3, 6, 5, 13, 14. Lead: 2, 9, 11, 12.

PS - Equal: 4, 7. Support: 10, 14.

PGB - Equal: 1, 3, 4, 6, 5, 7, 13, 14. Lead: 10.

Chapter 6: H.J. Jonas, P. Schall & P.G. Bolhuis, Activation of Colloidal Patchy Particle Networks. *In preparation*

HJJ - Equal: 1, 3, 6, 5, 14. Lead: 2, 9, 11, 12, 13.

PS - Equal: 4, 7. Support: 10.

PGB - Equal: 1, 3, 4, 6, 5, 7, 14. Lead: 10.

- 1. Conceptualization
- 2. Data Curation
- 3. Formal Analysis
- 4. Funding Acquisition
- 5. Investigation
- 6. Methodology
- 7. Project Administration

- 8. Resources
- 9. Software
- 10. Supervision
- 11. Validation
- 12. Visualization
- 13. Writing Original Draft
- 14. Writing Review & Editing

BIBLIOGRAPHY

- 1. P. W. Anderson, Science, 1972, 177, 393–396.
- 2. https://iupac.org/what-we-do/periodic-table-of-elements/. Accessed: 2023-08-08.
- 3. P. Atkins and R. Friedman. Oxford University Press, 2005, 69–98.
- 4. K. J. H. Giesbertz, Hartree-Fock and Density Functional Theory, 2020.
- 5. J. C. Slater, Phys. Rev., 1930, 36, 57-64.
- 6. M. Born and J. R. Oppenheimer, *Ann. Physik.*, 1927, **84**, 457.
- 7. https://www.britannica.com/animal/ant/. Accessed: 2023-10-20.
- 8. https://www.twinkl.nl/teaching-wiki/timeline-of-human-evolution/. Accessed: 2023-10-20.
- 9. M. Rubenstein and R. H. Colby. Oxford University Press, 2003, 309–402.
- 10. J. P. Lagerwall and G. Scalia, Curr. Appl. Phys., 2012, 12, 1387–1412.
- 11. L. Vicarelli, S. J. Heerema, C. Dekker, and H. W. Zandbergen, ACS Nano, 2015, 9, 3428-3435.
- 12. M. Varga. In: Fabr. Self-Assembly Nanobiomaterials. Elsevier, 2016, 57-90.
- 13. D. Luque and J. R. Castón, Nat. Chem. Biol., 2020, 16, 231-239.
- 14. B. Sun, E. J. Meeus, F. J. de Zwart, E. O. Bobylev, T. J. Mooibroek, S. Mathew, and J. N. H. Reek, *Chem. A Eur. J.*, 2023, **29**.
- 15. https://www.noaa.gov/stories/how-do-snowflakes-form-science-behind-snow. Accessed: 2023-08-08.
- 16. M. Allman, V. Betz, and M. Hairer, Stoch. Process. their Appl., 2011, 121, 2014-2042.
- 17. N. A. Wasio, R. C. Quardokus, R. P. Forrest, C. S. Lent, S. A. Corcelli, J. A. Christie, K. W. Henderson, and S. A. Kandel, *Nature*, 2014, **507**, 86–89.
- 18. G. M. Whitesides and M. Boncheva, Proc. Natl. Acad. Sci., 2002, 99, 4769-4774.
- 19. G. M. Whitesides and B. Grzybowski, *Science*, 2002, **295**, 2418–2421.
- C. Rossi-Gendron, F. El Fakih, L. Bourdon, K. Nakazawa, J. Finkel, N. Triomphe, L. Chocron, M. Endo, H. Sugiyama, G. Bellot, M. Morel, S. Rudiuk, and D. Baigl, *Nat. Nanotechnol.*, 2023.
- J. Lee Tin Wah, C. David, S. Rudiuk, D. Baigl, and A. Estevez-Torres, ACS Nano, 2016, 10, 1978–1987.
- S. H. Shin, S. Chung, B. Sanii, L. R. Comolli, C. R. Bertozzi, and J. J. De Yoreo, *Proc. Natl. Acad. Sci. U. S. A.*, 2012, 109, 12968–12973.
- 23. G. Sinawang, M. Osaki, Y. Takashima, H. Yamaguchi, and A. Harada, *Chem. Commun.*, 2020, **56**, 4381–4395.
- 24. N. Kang, J. Zhu, X. Zhang, H. Wang, and Z. Zhang, J. Am. Chem. Soc., 2022, 144, 4754–4758.
- 25. M. F. Hagan and D. Chandler, *Biophys. J.*, 2006, **91**, 42–54.
- 26. R. Tenchov, R. Bird, A. E. Curtze, and Q. Zhou, ACS Nano, 2021, 15, 16982–17015.
- 27. S. Ashique, A. Garg, A. Hussain, A. Farid, P. Kumar, and F. Taghizadeh-Hesary, *Cancer Med.*, 2023, 1–29.
- 28. I. E. Mba and E. I. Nweze, World J. Microbiol. Biotechnol., 2021, 37, 108.
- 29. P. Dauber-Osguthorpe and A. T. Hagler, J. Comput. Aided. Mol. Des., 2019, 33, 133–203.
- 30. R. Alessandri, F. Grünewald, and S. J. Marrink, Adv. Mater., 2021, 33, 2008635.
- 31. A. Neophytou, D. Chakrabarti, and F. Sciortino, Proc. Natl. Acad. Sci. U. S. A., 2021, 118, 1-7.

- 32. J. Russo, F. Romano, L. Kroc, F. Sciortino, L. Rovigatti, and P. Šulc, *J. Phys. Condens. Matter*, 2022, **34**, 354002.
- 33. B. Mohr, K. Shmilovich, I. S. Kleinwächter, D. Schneider, A. L. Ferguson, and T. Bereau, *Chem. Sci.*, 2022, **13**, 4498–4511.
- 34. M. Kamp, B. de Nijs, M. N. van der Linden, I. de Feijter, M. J. Lefferts, A. Aloi, J. Griffiths, J. J. Baumberg, I. K. Voets, and A. van Blaaderen, *Langmuir*, 2020, **36**, 2403–2418.
- 35. M. Kumar, A. Singh, B. Del Secco, M. V. Baranov, G. van den Bogaart, S. Sacanna, and S. Thutupalli, *Soft Matter*, 2022, **18**, 1757–1766.
- 36. M. He, J. P. Gales, É. Ducrot, Z. Gong, G.-R. Yi, S. Sacanna, and D. J. Pine, *Nature*, 2020, **585**, 524–529.
- 37. W. M. McFadden, A. A. Snyder, K. A. Kirby, P. R. Tedbury, M. Raj, Z. Wang, and S. G. Sarafianos, *Retrovirology*, 2021, **18**, 41.
- 38. Y. Wang, Y. Wang, D. R. Breed, V. N. Manoharan, L. Feng, A. D. Hollingsworth, M. Weck, and D. J. Pine, *Nature*, 2012, **491**, 51–55.
- 39. E. G. Noya, C. Vega, J. P. K. Doye, and A. A. Louis, *J. Chem. Phys.*, 2007, **127**.
- 40. F. Sciortino and E. Zaccarelli, Curr. Opin. Solid State Mater. Sci., 2011, 15, 246-253.
- 41. Zhang, A. S. Keys, T. Chen, and S. C. Glotzer, *Langmuir*, 2005, **21**, 11547–11551.
- 42. I. M. Ilie, W. K. den Otter, and W. J. Briels, J. Chem. Phys., 2016, 144.
- 43. A. C. Newton, R. Kools, D. W. H. Swenson, and P. G. Bolhuis, *J. Chem. Phys.*, 2017, **147**, 155101.
- 44. A. C. Newton, T. A. Nguyen, S. J. Veen, D. J. Kraft, P. Schall, and P. G. Bolhuis, *Soft Matter*, 2017, **13**, 4903–4915.
- 45. A. C. Newton, T. A. Nguyen, S. J. Veen, D. J. Kraft, P. Schall, and P. G. Bolhuis, *Soft Matter*, 2017, **13**, 4903–4915.
- 46. É. Duguet, C. Hubert, C. Chomette, A. Perro, and S. Ravaine, *Comptes Rendus Chim.*, 2016, 19, 173–182.
- 47. J. R. Wolters, G. Avvisati, F. Hagemans, T. Vissers, D. J. Kraft, M. Dijkstra, and W. K. Kegel, *Soft Matter*, 2015, **11**, 1067–1077.
- 48. K. Zhao and T. G. Mason, Reports Prog. Phys., 2018, 81, 126601.
- 49. T. Hueckel, G. M. Hocky, and S. Sacanna, Nat. Rev. Mater., 2021, 6, 1053–1069.
- 50. Y. Shelke, S. Marín-Aguilar, F. Camerin, M. Dijkstra, and D. J. Kraft, *J. Colloid Interface Sci.*, 2023, 629, 322–333.
- 51. X. Xia, H. Hu, M. P. Ciamarra, and R. Ni, *Sci. Adv.*, 2020, **6**, 1–8.
- 52. M. R. Jones, N. C. Seeman, and C. A. Mirkin, *Science*, 2015, **347**, 1260901–1260901.
- 53. S. Stuij, J. Rouwhorst, H. J. Jonas, N. Ruffino, Z. Gong, S. Sacanna, P. G. Bolhuis, and P. Schall, *Phys. Rev. Lett.*, 2021, **127**, 108001.
- 54. S. G. Stuij, H. J. Jonas, Z. Gong, S. Sacanna, T. E. Kodger, P. G. Bolhuis, and P. Schall, *Soft Matter*, 2021, **17**, 8291–8299.
- 55. S. G. Stuij, A. Biebricher, Z. Gong, S. Sacanna, E. Peterman, I. Heller, and P. Schall, *Phys. Rev. Mater.*, 2022, **6**, 035603.
- 56. S. G. Stuij. Available at https://dare.uva.nl/search?identifier=e514daaa-0046-4f1a-9e0f-8799c5bd4e31. PhD thesis. University of Amsterdam, 2020.
- 57. P. J. M. Swinkels, S. G. Stuij, Z. Gong, H. Jonas, N. Ruffino, B. van der Linden, P. G. Bolhuis, S. Sacanna, S. Woutersen, and P. Schall, *Nat. Commun.*, 2021, **12**, 2810.
- 58. P. J. M. Swinkels, Z. Gong, S. Sacanna, E. G. Noya, and P. Schall, *Nat. Commun.*, 2023, 14, 1524.
- P. J. M. Swinkels, Z. Gong, S. Sacanna, E. G. Noya, and P. Schall, *Soft Matter*, 2023, 19, 3414–3422.

- 60. P.J.M. Swinkels. Available at https://dare.uva.nl/search?identifier=5fd09f9c-a3b5-4c98-91af-b82cc6fe78a3. PhD thesis. University of Amsterdam, 2022.
- 61. L. Rossi, S. Sacanna, W. T. M. Irvine, P. M. Chaikin, D. J. Pine, and A. P. Philipse, *Soft Matter*, 2011, 7, 4139–4142.
- 62. L. Boltzmann. University of California Press, 1964.
- 63. Z. Gong, T. Hueckel, G.-r. Yi, and S. Sacanna, *Nature*, 2017, **550**, 234–238.
- 64. N. Kern and D. Frenkel, J. Chem. Phys., 2003, 118, 9882-9889.
- 65. D. Frenkel, Science, 2006, 314, 768-769.
- J. R. Espinosa, J. A. Joseph, I. Sanchez-Burgos, A. Garaizar, D. Frenkel, and R. Collepardo-Guevara, Proc. Natl. Acad. Sci., 2020, 117, 13238–13247.
- 67. D. Dantchev and S. Dietrich, *Phys. Rep.*, 2023, **1005**, 1–130.
- 68. J. M. Beggs and D. Plenz, *J. Neurosci.*, 2003, **23**, 11167–11177.
- 69. J. Scheinkman and M. Woodford, Am. Econ. Rev. Pap. Proc., 1994, 84, 417.
- 70. E. Ising, Zeitschrift für Phys., 1925, 31, 253-258.
- 71. A. Pelissetto and E. Vicari, *Phys. Rep.*, 2002, **368**, 549–727.
- 72. S. G. Stuij, M. Labbé-Laurent, T. E. Kodger, A. Maciołek, and P. Schall, *Soft Matter*, 2017, **13**, 5233–5249.
- 73. M. Tröndle, S. Kondrat, A. Gambassi, L. Harnau, and S. Dietrich, J. Chem. Phys., 2010, 133.
- 74. M. Tröndle, L. Harnau, and S. Dietrich, J. Phys. Condens. Matter, 2015, 27, 214006.
- 75. T. A. Nguyen, A. Newton, S. J. Veen, D. J. Kraft, P. G. Bolhuis, and P. Schall, *Adv. Mater.*, 2017, **29**, 1–6.
- E. Marino, D. M. Balazs, R. W. Crisp, D. Hermida-Merino, M. A. Loi, T. E. Kodger, and P. Schall, J. Phys. Chem. C, 2019, 123, 13451–13457.
- 77. H. Guo, G. Stan, and Y. Liu, *Soft Matter*, 2018, **14**, 1311–1318.
- 78. O. A. Vasilyev, E. Marino, B. B. Kluft, P. Schall, and S. Kondrat, *Nanoscale*, 2021, 13, 6475–6488.
- 79. C. L. Kennedy, D. Sayasilpi, P. Schall, and J.-M. Meijer, J. Phys. Condens. Matter, 2022, 34, 214005.
- 80. M. Fisher and P. de Gennes, C. R. Acad. Sci. Paris B, 1978, 287, 207–209.
- 81. A. Stein, S. J. Davidson, J. C. Allegra, and G. F. Allen, J. Chem. Phys., 1972, 56, 6164-6168.
- 82. O. A. Vasilyev and S. Dietrich, EPL (Europhysics Lett., 2013, 104, 60002.
- 83. T. F. Mohry, S. Kondrat, A. Maciołek, and S. Dietrich, Soft Matter, 2014, 10, 5510–5522.
- 84. L. R. White, J. Colloid Interface Sci., 1983, 95, 286–288.
- 85. U. Gasser, E. R. Weeks, A. Schofield, P. N. Pusey, and D. A. Weitz, Science, 2001, 292, 258-262.
- 86. J. R. Savage, D. W. Blair, A. J. Levine, R. A. Guyer, and A. D. Dinsmore, *Science*, 2006, 314, 795–798.
- 87. A. M. Alsayed, M. F. Islam, J. Zhang, P. J. Collings, and A. G. Yodh, *Science*, 2005, **309**, 1207–1210
- 88. X. Wang, B. Li, M. Li, and Y. Han, Nat. Phys., 2023, 19, 700-705.
- N. Tanjeem, W. H. Wilkin, D. A. Beller, C. H. Rycroft, and V. N. Manoharan, *ACS Appl. Nano Mater.*, 2021, 4, 10682–10691.
- 90. X. Xiao, L. Wang, Z. Wang, and Z. Wang, Nat. Commun., 2022, 13, 1599.
- 91. K. Oura, M. Katayama, A. V. Zotov, V. G. Lifshits, and S. A. A. Springer-Verlag Berlin Heidelberg, 2003.
- 92. W. Poon, Science, 2004, 304, 830-831.
- 93. J. Russo, F. Leoni, F. Martelli, and F. Sciortino, Reports Prog. Phys., 2022, 85, 016601.
- 94. E. Bianchi, J. Largo, P. Tartaglia, E. Zaccarelli, and F. Sciortino, Phys. Rev. Lett., 2006, 97, 168301.

- 95. A. W. Wilber, J. P. K. Doye, A. A. Louis, E. G. Noya, M. A. Miller, and P. Wong, *J. Chem. Phys.*, 2007, **127**.
- 96. C. De Michele, T. Bellini, and F. Sciortino, Macromolecules, 2012, 45, 1090–1106.
- 97. R. Guo, J. Mao, X.-M. Xie, and L.-T. Yan, Sci. Rep., 2015, 4, 7021.
- 98. P. Song, Y. Wang, Y. Wang, A. D. Hollingsworth, M. Weck, D. J. Pine, and M. D. Ward, *J. Am. Chem. Soc.*, 2015, **137**, 3069–3075.
- N. Skar-Gislinge, M. Ronti, T. Garting, C. Rischel, P. Schurtenberger, E. Zaccarelli, and A. Stradner, Mol. Pharm., 2019, 16, 2394–2404.
- 100. D. Fusco and P. Charbonneau, *Phys. Rev. E*, 2013, **88**, 012721.
- C. Gögelein, G. Nägele, R. Tuinier, T. Gibaud, A. Stradner, and P. Schurtenberger, J. Chem. Phys., 2008, 129.
- 102. I. M. Ilie, W. K. den Otter, and W. J. Briels, J. Chem. Phys., 2014, 141, 065101.
- 103. L. Blanchoin, R. Boujemaa-Paterski, C. Sykes, and J. Plastino, *Physiol. Rev.*, 2014, **94**, 235–263.
- 104. J. Prost, F. Jülicher, and J.-F. Joanny, *Nat. Phys.*, 2015, **11**, 111–117.
- 105. B. Najma, M. Varghese, L. Tsidilkovski, L. Lemma, A. Baskaran, and G. Duclos, *Nat. Commun.*, 2022, **13**.
- 106. D. F. Tracey, E. G. Noya, and J. P. K. Doye, J. Chem. Phys., 2019, 151.
- 107. F. Romano, J. Russo, L. Kroc, and P. Šulc, *Phys. Rev. Lett.*, 2020, **125**, 118003.
- 108. S. Marín-Aguilar, F. Camerin, and M. Dijkstra, *J. Chem. Phys.*, 2022, **157**, 154503.
- 109. J. Clerk-Maxwell, Nature, 1874, 10, 477-480.
- 110. https://www.nobelprize.org/uploads/2018/06/waals-lecture.pdf. Accessed: 2023-09-31.
- 111. J.-P. Hansen and I. R. McDonald. In: *Theory of Simple Liquids (Fourth Edition)*. Ed. by J.-P. Hansen and I. R. McDonald. Fourth Edition. Academic Press, Oxford, 2013, 149–202.
- 112. M. S. Wertheim, J. Stat. Phys., 1984, 35, 35-47.
- 113. M. S. Wertheim, J. Stat. Phys., 1984, 35, 19-34.
- 114. M. S. Wertheim, *J. Stat. Phys.*, 1986, **42**, 477–492.
- 115. M. S. Wertheim, J. Stat. Phys., 1986, 42, 459–476.
- 116. W. G. Chapman, K. E. Gubbins, G. Jackson, and M. Radosz, *Fluid Phase Equilib.*, 1989, **52**, 31–38.
- 117. W. Zmpitas and J. Gross, *Fluid Phase Equilib.*, 2016, **428**, 121–152.
- 118. K. A. Fichthorn and W. H. Weinberg, *J. Chem. Phys.*, 1991, **95**, 1090–1096.
- 119. F. Romano, C. De Michele, D. Marenduzzo, and E. Sanz, J. Chem. Phys., 2011, 135, 124106.
- 120. I. M. Ilie, W. J. Briels, and W. K. den Otter, J. Chem. Phys., 2015, 142, 048102.
- 121. M. P. Allen and G. Germano, *Mol. Phys.*, 2006, **104**, 3225–3235.
- 122. D. Nishiguchi, J. Iwasawa, H.-R. Jiang, and M. Sano, New J. Phys., 2018, 20, 015002.
- 123. K. Dietrich, D. Renggli, M. Zanini, G. Volpe, I. Buttinoni, and L. Isa, *New J. Phys.*, 2017, **19**, 065008
- 124. N. Oikonomeas, D. Kraft, and P. Schall, *unpublished*.
- 125. B. Szabó, G. J. Szöllösi, B. Gönci, Z. Jurányi, D. Selmeczi, and T. Vicsek, *Phys. Rev. E*, 2006, **74**, 061908.
- 126. S. van Teeffelen and H. Löwen, *Phys. Rev. E*, 2008, **78**, 020101.
- 127. S. Henkes, Y. Fily, and M. C. Marchetti, *Phys. Rev. E*, 2011, **84**, 040301.
- 128. G. S. Redner, A. Baskaran, and M. F. Hagan, *Phys. Rev. E*, 2013, **88**, 012305.
- S. E. Moran, I. R. Bruss, P. W. A. Schönhöfer, and S. C. Glotzer, *Soft Matter*, 2022, 18, 1044– 1053.
- 130. J. Eglinton, M. I. Smith, and M. R. Swift, *Phys. Rev. E*, 2022, **105**, 044609.

- D. Rogel Rodriguez, F. Alarcon, R. Martinez, J. Ramírez, and C. Valeriani, Soft Matter, 2020, 16, 1162–1169.
- 132. T. Kolb and D. Klotsa, *Soft Matter*, 2020, **16**, 1967–1978.
- C. Bechinger, R. Di Leonardo, H. Löwen, C. Reichhardt, G. Volpe, and G. Volpe, *Rev. Mod. Phys.*, 2016, 88, 045006.
- 134. L. Fang, L. Li, J. Guo, Y. Liu, and X. Huang, Phys. Lett. A, 2022, 427, 127934.
- 135. W. R. Hamilton, Trans. R. Ir. Acad., 1837, 17, 293-422.
- 136. P. G. Bolhuis and C. Dellago. In: *Reviews in Computational Chemistry*. John Wiley and Sons, Ltd, 2010. Chap. 3, 111–210.
- 137. T. S. van Erp, D. Moroni, and P. G. Bolhuis, J. Chem. Phys., 2003, 118, 7762-7774.
- 138. T. Nguyen, A. Newton, D. Kraft, P. G. Bolhuis, and P. Schall, Materials, 2017, 10, 1265.
- 139. S. Stuij, J. M. van Doorn, T. Kodger, J. Sprakel, C. Coulais, and P. Schall, *Phys. Rev. Res.*, 2019, **1**, 023033.
- 140. F. Sciortino, E. Bianchi, J. F. Douglas, and P. Tartaglia, J. Chem. Phys., 2007, 126, 194903.
- 141. E. Bianchi, P. Tartaglia, E. La Nave, and F. Sciortino, J. Phys. Chem. B, 2007, 111, 11765–11769.
- 142. J. Russo, P. Tartaglia, and F. Sciortino, *Soft Matter*, 2010, **6**, 4229–4236.
- L. Rovigatti, D. De Las Heras, J. M. Tavares, M. M. Telo Da Gama, and F. Sciortino, *J. Chem. Phys.*, 2013, 138, 164904.
- 144. K. T. Nguyen and C. De Michele, Eur. Phys. J. E, 2018, 41, 141.
- 145. S. Roldán-Vargas, L. Rovigatti, and F. Sciortino, Soft Matter, 2017, 13, 514-530.
- A. C. Newton, J. Groenewold, W. K. Kegel, and P. G. Bolhuis, *Proc. Natl. Acad. Sci.*, 2015, 112, 15308–15313.
- 147. A. Gambassi, J. Phys. Conf. Ser., 2009, **161**, 012037.
- 148. F. Soyka, O. Zvyagolskaya, C. Hertlein, L. Helden, and C. Bechinger, *Phys. Rev. Lett.*, 2008, **101**, 208301.
- 149. N. Farahmand Bafi, P. Nowakowski, and S. Dietrich, *J. Chem. Phys.*, 2020, **152**, 114902.
- 150. A. Maciołek and S. Dietrich, *Rev. Mod. Phys.*, 2018, **90**, 045001.
- W. B. Russel, D. A. Saville, and W. R. Schowalter. Cambridge Monographs on Mechanics. Cambridge University Press, 1989.
- 152. J.-P. Hansen and H. Löwen, Annu. Rev. Phys. Chem., 2000, 51, 209-42.
- 153. V. A. Parsegian. January. Cambridge University Press, 2005, 1–380.
- 154. O. Vasilyev and A. Maciołek, *J. Non. Cryst. Solids*, 2015, **407**, 376–383.
- 155. A. Hanke, F. Schlesener, E. Eisenriegler, and S. Dietrich, *Phys. Rev. Lett.*, 1998, **81**, 1885–1888.
- 156. M. Tröndle, O. Zvyagolskaya, A. Gambassi, D. Vogt, L. Harnau, C. Bechinger, and S. Dietrich, *Mol. Phys.*, 2011, **109**, 1169–1185.
- 157. F. Pousaneh, A. Ciach, and A. Maciołek, *Soft Matter*, 2014, **10**, 470–483.
- 158. T. F. Mohry, A. Maciołek, and S. Dietrich, *Phys. Rev. E*, 2010, **81**, 061117.
- 159. K. Sadakane, A. Onuki, K. Nishida, S. Koizumi, and H. Seto, *Phys. Rev. Lett.*, 2009, **103**, 167803.
- 160. K. Sadakane, M. Nagao, H. Endo, and H. Seto, *J. Chem. Phys.*, 2013, **139**, 234905.
- 161. F. Pousaneh and A. Ciach, *Soft Matter*, 2014, **10**, 8188–8201.
- 162. T. F. Mohry, A. Maciołek, and S. Dietrich, *J. Chem. Phys.*, 2012, **136**, 224902.
- 163. F. Gittes, B. Mickey, J. Nettleton, and J. Howard, J. Cell Biol., 1993, 120, 923-934.
- 164. C. P. Brangwynne, G. H. Koenderink, E. Barry, Z. Dogic, F. C. MacKintosh, and D. A. Weitz, *Biophys. J.*, 2007, **93**, 346–359.
- 165. M. Krech, Phys. Rev. E, 1997, 56, 1642–1659.
- 166. C. Hertlein, L. Helden, A. Gambassi, S. Dietrich, and C. Bechinger, *Nature*, 2008, 451, 172–175.

- C. van der Wel, R. K. Bhan, R. W. Verweij, H. C. Frijters, Z. Gong, A. D. Hollingsworth, S. Sacanna, and D. J. Kraft, *Langmuir*, 2017, 33, 8174–8180.
- 168. SigmaAldrich. https://www.sigmaaldrich.com/catalog/product/sigma/89904. Sigma Aldrich.
- 169. Y. Jayalakshmi, J. S. Van Duijneveldt, and D. Beysens, J. Chem. Phys., 1994, 100, 604-609.
- S. Z. Mirzaev, R. Behrends, T. Heimburg, J. Haller, and U. Kaatze, *J. Chem. Phys.*, 2006, 124, 144517.
- 171. G. Avvisati and M. Dijkstra, *Soft Matter*, 2015, **11**, 8432–8440.
- 172. W. G. Chapman, K. E. Gubbins, G. Jackson, and M. Radosz, *Ind. Eng. Chem. Res.*, 1990, **29**, 1709–1721.
- 173. P. Tartaglia and F. Sciortino, J. Phys. Condens. Matter, 2010, 22, 104108.
- 174. W. Rzysko, S. Sokołowski, and T. Staszewski, *J. Chem. Phys.*, 2015, **143**, 064509.
- 175. D. Stopper, H. Hansen-Goos, R. Roth, and R. Evans, *J. Chem. Phys.*, 2020, **152**, 111101.
- 176. W. H. Stockmayer, *J. Chem. Phys.*, 1943, **11**, 45–55.
- 177. A. Oleksy and P. I. C. Teixeira, *Phys. Rev. E*, 2015, **91**, 012301.
- 178. P. I. C. Teixeira and J. M. Tavares, Curr. Opin. Colloid Interface Sci., 2017, 30, 16–24.
- 179. F. Sciortino and E. Zaccarelli, Curr. Opin. Colloid Interface Sci. Interface Sci., 2017, 30, 90–96.
- S. Biffi, R. Cerbino, F. Bomboi, E. M. Paraboschi, R. Asselta, F. Sciortino, and T. Bellini, Proc. Natl. Acad. Sci., 2013, 110, 15633–15637.
- 181. B. Ruzicka, E. Zaccarelli, L. Zulian, R. Angelini, M. Sztucki, A. Moussaïd, T. Narayanan, and F. Sciortino, *Nat. Mater.*, 2011, **10**, 56–60.
- 182. H. J. Jonas, S. G. Stuij, P. Schall, and P. G. Bolhuis, *J. Chem. Phys.*, 2021, **155**, 034902.
- 183. F. Sciortino, *Riv. del Nuovo Cim.*, 2019, **42**, 511–548.
- 184. H. Li, J. Xiao, Q. Fu, and X. Bao, Proc. Natl. Acad. Sci., 2017, 114, 5930-5934.
- D. Dubbeldam, K. S. Walton, T. J. H. Vlugt, and S. Calero, Adv. Theory Simulations, 2019, 2, 1900135.
- 186. B. Radha, A. Esfandiar, F. C. Wang, A. P. Rooney, K. Gopinadhan, A. Keerthi, A. Mishchenko, A. Janardanan, P. Blake, L. Fumagalli, M. Lozada-Hidalgo, S. Garaj, S. J. Haigh, I. V. Grigorieva, H. A. Wu, and A. K. Geim, *Nature*, 2016, **538**, 222–225.
- 187. V. Mouarrawis, R. Plessius, J. I. van der Vlugt, and J. N. H. Reek, Front. Chem., 2018, 6, 1–20.
- 188. A. Esfandiar, B. Radha, F. C. Wang, Q. Yang, S. Hu, S. Garaj, R. R. Nair, A. K. Geim, and K. Gopinadhan, *Science*, 2017, **358**, 511–513.
- 189. D. Muñoz-Santiburcio and D. Marx, Chem. Sci., 2017, **8**, 3444–3452.
- 190. L. Bocquet, Nat. Mater., 2020, 19, 254–256.
- 191. S. Seo, D. Ha, and T. Kim, *Nat. Commun.*, 2021, **12**, 1336.
- 192. W. H. Thompson, J. Chem. Phys., 2018, 149, 170901.
- 193. S. Faucher, N. Aluru, M. Z. Bazant, D. Blankschtein, A. H. Brozena, J. Cumings, J. Pedro de Souza, M. Elimelech, R. Epsztein, J. T. Fourkas, A. G. Rajan, H. J. Kulik, A. Levy, A. Majumdar, C. Martin, M. McEldrew, R. P. Misra, A. Noy, T. A. Pham, M. Reed, E. Schwegler, Z. Siwy, Y. Wang, and M. Strano, J. Phys. Chem. C, 2019, 123, 21309–21326.
- 194. S. Sokołowski and Y. V. Kalyuzhnyi, *J. Phys. Chem. B*, 2014, **118**, 9076–9084.
- 195. B. D. Marshall, *Phys. Rev. E*, 2016, **94**, 012615.
- R. Braz Teixeira, D. de las Heras, J. M. Tavares, and M. M. Telo da Gama, J. Chem. Phys., 2021,
 155, 044903.
- 197. W. G. Chapman, G. Jackson, and K. E. Gubbins, *Mol. Phys.*, 1988, **65**, 1057–1079.
- 198. E. Kierlik and M. L. Rosinberg, *J. Chem. Phys.*, 1992, **97**, 9222–9239.
- 199. E. Kierlik and M. L. Rosinberg, *J. Chem. Phys.*, 1993, **99**, 3950–3965.

- 200. E. Kierlik and M. L. Rosinberg, *J. Chem. Phys.*, 1994, **100**, 1716–1730.
- 201. P. I. C. Teixeira and F. Sciortino, J. Chem. Phys., 2019, 151, 174903.
- 202. E. L. Camacho Vergara, G. M. Kontogeorgis, and X. Liang, Mol. Phys., 2020, 118, e1725668.
- 203. B. D. Marshall, J. Chem. Phys., 2015, 142, 234906.
- P. van der Schoot. In: Engineering Aspects of Self-Organizing Materials. Ed. by R. J. Koopmans.
 Vol. 35. Advances in Chemical Engineering. Academic Press, 2009, 45–77.
- 205. R. P. Sear and G. Jackson, J. Chem. Phys., 1996, 105, 1113-1120.
- 206. J. F. Douglas, J. Dudowicz, and K. F. Freed, J. Chem. Phys., 2008, 128, 224901.
- 207. M. M. J. Smulders, M. M. L. Nieuwenhuizen, T. F. A. de Greef, P. van der Schoot, A. P. H. J. Schenning, and E. W. Meijer, *Chem. A Eur. J.*, 2010, **16**, 362–367.
- 208. W. Bol, Molecular Physics, 1982, 45, 605-616.
- 209. A. Santos and M. L. de Haro, Phys. Rev. E, 2016, 93, 062126.
- 210. S. B. Yuste and A. Santos, *J. Chem. Phys.*, 1993, **99**, 2020–2023.
- 211. J. D. Weeks, D. Chandler, and H. C. Andersen, J. Chem. Phys., 1971, 54, 5237-5247.
- 212. A. Meurer, C. P. Smith, M. Paprocki, O. Čertík, S. B. Kirpichev, M. Rocklin, A. Kumar, S. Ivanov, J. K. Moore, S. Singh, T. Rathnayake, S. Vig, B. E. Granger, R. P. Muller, F. Bonazzi, H. Gupta, S. Vats, F. Johansson, F. Pedregosa, M. J. Curry, A. R. Terrel, v. Roučka, A. Saboo, I. Fernando, S. Kulal, R. Cimrman, and A. Scopatz, *PeerJ Computer Science*, 2017, 3, e103.
- 213. E. H. Barriga, K. Franze, G. Charras, and R. Mayor, *Nature*, 2018, **554**, 523–527.
- 214. F. Burla, Y. Mulla, B. E. Vos, A. Aufderhorst-Roberts, and G. H. Koenderink, *Nat. Rev. Phys.*, 2019, **1**, 249–263.
- 215. G. L. Jackson, J. M. Dennis, N. D. Dolinski, M. van der Naald, H. Kim, C. Eom, S. J. Rowan, and H. M. Jaeger, *Macromolecules*, 2022, **55**, 6453–6461.
- 216. M. P. Murrell and M. L. Gardel, *Proc. Natl. Acad. Sci.*, 2012, **109**, 20820–20825.
- 217. J. Alvarado, M. Sheinman, A. Sharma, F. C. Mackintosh, and G. H. Koenderink, *Nat. Phys.*, 2013, 9, 591–597.
- C. Alkemade, H. Wierenga, V. A. Volkov, M. Preciado López, A. Akhmanova, P. R. ten Wolde, M. Dogterom, and G. H. Koenderink, *Proc. Natl. Acad. Sci.*, 2022, 119, 1–12.
- 219. Y. Mulla, M. J. Avellaneda, A. Roland, L. Baldauf, W. Jung, T. Kim, S. J. Tans, and G. H. Koenderink, *Nat. Mater.*, 2022, **21**, 1019–1023.
- 220. H. N. Verwei, G. Lee, G. Leech, I. I. Petitjean, G. H. Koenderink, R. M. Robertson-Anderson, and R. J. McGorty, *J. Vis. Exp.*, 2022, 1–27.
- 221. R. G. Winkler, J. Elgeti, and G. Gompper, J. Phys. Soc. Japan, 2017, 86, 101014.
- 222. S. Joo, X. Durang, O.-c. Lee, and J.-H. Jeon, Soft Matter, 2020, 16, 9188–9201.
- A. Militaru, M. Innerbichler, M. Frimmer, F. Tebbenjohanns, L. Novotny, and C. Dellago, *Nat. Commun.*, 2021, 12, 2446.
- 224. J. Zhang, T. Huang, G. Xu, and Y. Chen, Commun. Theor. Phys., 2022, 74, 075601.
- 225. Y. Kim, S. Joo, W. K. Kim, and J.-H. Jeon, *Macromolecules*, 2022, **55**, 7136–7147.
- 226. R. Khalaf, A. Viamonte, E. Ducrot, R. Mérindol, and S. Ravaine, Nanoscale, 2023, 15, 573-577.
- I. Chakraborty, D. J. G. Pearce, R. W. Verweij, S. C. Matysik, L. Giomi, and D. J. Kraft, ACS Nano, 2022, 16, 2471–2480.
- 228. J. R. Howse, R. A. L. Jones, A. J. Ryan, T. Gough, R. Vafabakhsh, and R. Golestanian, *Phys. Rev. Lett.*, 2007, **99**, 048102.
- H. Seyforth, M. Gomez, W. B. Rogers, J. L. Ross, and W. W. Ahmed, *Phys. Rev. Res.*, 2022, 4, 023043.
- 230. A. Vijaykumar, P. R. ten Wolde, and P. G. Bolhuis, *Mol. Phys.*, 2018, **116**, 3042–3054.

- 231. G. Cowan. Oxford University Press, USA, 1998.
- 232. H. Flyvbjerg and H. G. Petersen, J. Chem. Phys., 1989, 91, 461-466.
- 233. J. K. G. Dhont, G. W. Park, and W. J. Briels, Soft Matter, 2021, 17, 5613-5632.
- 234. A. Vijaykumar, P. G. Bolhuis, and P. R. ten Wolde, Faraday Discuss., 2016, 195, 421-441.
- 235. H. Kramers, *Physica*, 1940, 7, 284–304.
- 236. P. Hänggi, P. Talkner, and M. Borkovec, Rev. Mod. Phys., 1990, 62, 251–341.
- 237. A. Geiseler, P. Hänggi, and G. Schmid, Eur. Phys. J. B, 2016, 89, 175.
- 238. L. Natali, L. Caprini, and F. Cecconi, Soft Matter, 2020, 16, 2594–2604.
- 239. J. Paturej, A. Milchev, V. G. Rostiashvili, and T. A. Vilgis, J. Chem. Phys., 2011, 134, 224901.
- 240. A. Zaccone, I. Terentjev, L. Di Michele, and E. M. Terentjev, J. Chem. Phys., 2015, 142, 114905.
- 241. C. F. Lee, J. Phys. Condens. Matter, 2015, 27, 275101.
- 242. C. F. Lee, J. Phys. Condens. Matter, 2018, 30, 315102.
- 243. M. Razbin, P. Benetatos, and A. A. Moosavi-Movahedi, Soft Matter, 2019, 15, 2469-2478.
- A. Ghosh, D. I. Dimitrov, V. G. Rostiashvili, A. Milchev, and T. A. Vilgis, *J. Chem. Phys.*, 2010, 132, 204902.
- 245. A. Mondal and G. Morrison, *J. Chem. Phys.*, 2022, **157**, 104903.
- 246. A. M. Lorenzo, E. M. De La Cruz, and E. F. Koslover, Soft Matter, 2020, 16, 2017–2024.
- 247. S. Henkes, C. Brito, and O. Dauchot, Soft Matter, 2012, 8, 6092.
- 248. N. Michaud-Agrawal, E. J. Denning, T. B. Woolf, and O. Beckstein, *Journal of Computational Chemistry*, 2011, **32**, 2319–2327.
- 249. Richard J. Gowers, Max Linke, Jonathan Barnoud, Tyler J. E. Reddy, Manuel N. Melo, Sean L. Seyler, Jan Domański, David L. Dotson, Sébastien Buchoux, Ian M. Kenney, and Oliver Beckstein. In: *Proceedings of the 15th Python in Science Conference*. Ed. by Sebastian Benthall and Scott Rostrup. 2016, 98 –105.
- 250. P. Baconnier, D. Shohat, C. H. López, C. Coulais, V. Démery, G. Düring, and O. Dauchot, *Nat. Phys.*, 2022, **18**, 1234–1239.
- 251. T. Vicsek and A. Zafeiris, *Phys. Rep.*, 2012, **517**, 71–140.
- 252. J. Palacci, S. Sacanna, A. P. Steinberg, D. J. Pine, and P. M. Chaikin, Science, 2013, 339, 936–939.
- 253. I. Buttinoni, J. Bialké, F. Kümmel, H. Löwen, C. Bechinger, and T. Speck, *Phys. Rev. Lett.*, 2013, **110**, 238301.
- 254. A. Bricard, J.-B. Caussin, N. Desreumaux, O. Dauchot, and D. Bartolo, *Nature*, 2013, **503**, 95–98.
- 255. Y. Fily and M. C. Marchetti, *Phys. Rev. Lett.*, 2012, **108**, 235702.
- 256. G. S. Redner, M. F. Hagan, and A. Baskaran, *Phys. Rev. Lett.*, 2013, **110**, 055701.
- T. Vicsek, A. Czirók, E. Ben-Jacob, I. Cohen, and O. Shochet, *Phys. Rev. Lett.*, 1995, 75, 1226–1229.
- 258. J. Stenhammar, R. Wittkowski, D. Marenduzzo, and M. E. Cates, *Phys. Rev. Lett.*, 2015, 114, 018301.
- 259. A. Wysocki, R. G. Winkler, and G. Gompper, New J. Phys., 2016, 18, 123030.
- 260. R. Wittkowski, J. Stenhammar, and M. E. Cates, New J. Phys., 2017, 19, 105003.
- 261. J. Stürmer, M. Seyrich, and H. Stark, *J. Chem. Phys.*, 2019, **150**.
- 262. F. Peruani, A. Deutsch, and M. Bär, *Phys. Rev. E*, 2006, **74**, 030904.
- 263. M. E. Cates and J. Tailleur, Annu. Rev. Condens. Matter Phys., 2015, 6, 219-244.
- 264. J. O'Byrne, A. Solon, J. Tailleur, and Y. Zhao, Out-of-equilibrium Soft Matter, 2023, 107–150.
- J. Rouwhorst, P. Schall, C. Ness, T. Blijdenstein, and A. Zaccone, *Phys. Rev. E*, 2020, 102, 022602.

- 266. E. Lattuada, D. Caprara, R. Piazza, and F. Sciortino, Sci. Adv., 2021, 7, 1–7.
- 267. H. J. Jonas, P. Schall, and P. G. Bolhuis, J. Chem. Phys., 2022, 157, 094903.
- 268. S. Dikshit and S. Mishra, Eur. Phys. J. E, 2022, 45, 21.
- 269. B. Hrishikesh and E. Mani, Soft Matter, 2023, 19, 225-232.
- 270. R. Soto and R. Golestanian, Phys. Rev. Lett., 2014, 112, 068301.
- 271. R. Soto and R. Golestanian, Phys. Rev. E Stat. Nonlinear, Soft Matter Phys., 2015, 91, 1-9.
- 272. L. Angelani, C. Maggi, M. L. Bernardini, A. Rizzo, and R. Di Leonardo, *Phys. Rev. Lett.*, 2011, **107**, 138302.
- 273. M. Von Smoluchowski, Z. Phys. Chem., 1917, 92, 129.